E.T.S. de Ingenieros Industriales
y de Telecomunicación

# Integration of a photodiode for THz generation in the framework of TERALINKS Project

Máster Universitario en
Ingeniería de Telecomunicación

Trabajo Fin de Máster

Carlos Biurrun Quel
Dirigido por: Carlos del Río Bocio
Pamplona, 27 de junio de 2018

upna Universidad Pública de Navarra
Nafarroako Unibertsitate Publikoa

## Abstract

The constant growth in the demand for data rates in wireless networks leads to a continuous increase in the amount of resources allocated per user. This is translated to a continuous demand for more bandwidth. Terahertz range has been gaining attention dramatically for its potential applications, among which high data rate communications can be found. However, one of the limiting drawbacks of this frequencies is the difficulty of generating power from efficient THz sources. One of the most recurrent approaches is photomixing, in which two optical signals are mixed in a photodiode to generate terahertzes. However, this techniques carry a series of issues that must be solved, such as efficient coupling of the terahertz energy and efficient illumination. For this reason, a novel concept for integrating a THz-generating photomixer, based on an ellipsoidal reflector, is presented in this work. Although a fully operational device has not been achieved, all the main issues are addressed, design guidelines are provided and future lines of work are drawn. This has been developed in the framework of the TERALINKS project.

## Index Terms

Terahertz, photomixing, packaging, ellipse, reflector.

## Resumen

El crecimiento en la demanda de mayores velocidades en redes inalámbricas lleva a incrementar los recursos asignados al usuario, lo que se traduce en necesidad de mayores anchos de banda. La banda de Terahercios resulta muy interesante por sus potenciales aplicaciones, entre las cuales se encuentran las comunicaciones de gran tasa binaria. Sin embargo, una de las limitaciones fundamentales de esta banda es la dificultad para generar potencia eficientemente. Una de las técnicas mas recurrentes es el photomixing, por la cual dos frecuencias ópticas se baten en un fotodiodo para generar terahercios. Sin embargo, estas técnicas acarrean una serie de problemas, tales como el acoplo eficiente de la radiación generada y la iluminación del diodo. Por ello, en este trabajo se presenta un concepto novedoso para la integración de photomixers, basado en un reflector elipsoidal. Aunque no se ha conseguido un dispositivo operativo, los principales problemas son tratados, una serie de reglas de diseño son propuestas y las futuras líneas de trabajo son detalladas. Ello ha sido desarrollado en el marco del Proyecto TERALINKS.

## Palabras clave

Terahercios, photomixing, packaging, elipse, reflector.

## Acknowledgement

This Master Thesis entails the end of an academic stage in which I have grown as a person at the same time I have adquired the enabling skills for being a competitive telecommunication engineer. It would not be fair to list every single person who I am grateful for it, because I would probably miss a few of them. However, I would like to mention some specific people, which I will refer to in Spanish.

En primer lugar, quisiera agradecer a mi director, Carlos del Río, por su atención y plena disponibilidad ante las multiples consultas que le he realizado, así como la oportunidad para adentrarme en el mundo académico y de investigación a la vez que continuaba con mis estudios de Máster.

También me gustaría agradecerle su ayuda a Jorge Teniente, que siempre ha estado dispuesto a solventar las consultas que le planteaba y con quien realicé previamente varias becas de colaboración.

Aprovecho también para agradecerles a mis compañeros de sala: Alicia, Alexia, José, Unai, Iñigo e Irati por su ayuda así como por el compañerismo del grupo.

Finalmente, dedicárselo a mi familia, en especial a mis padres, quienes han hecho posible que estudiara lo que quisiera y que me han apoyado durante todo este tiempo; a los compañeros de clase en el Máster, por el buen ambiente que hemos tenido estos dos años (así como los años de Grado, con algunos); a la cuadrilla y amigos, porque también viene bien desconectar de vez en cuando; y a Mar, por su capacidad de animarme y haberse convertido en un punto de apoyo fundamental.

This work has been supported by Spanish Ministry of Economy, Industry and Competitiveness, PCIN-2016-073 in the framework of European CHIST-ERA project Call 2015, TERALINKS.

# Index

## List of Abbreviations

| | |
|---|---|
| AiP | Antenna in Package |
| BWO | Backward Wave Oscillator |
| CW | Continuous Wave |
| Gbps | Gigabits per second ($10^9$ bits per second) |
| GRIN | Graded Index |
| EDFA | Erbium-Doped Fibre Amplifier |
| FEL | Free-Electron Laser |
| FFF | Fused Filament Fabrication |
| HBT | Heterostructure Bipolar Junction |
| HBV | Heterostructure Barrier Varactor |
| HEMT | High Electron Mobility Transistor |
| HPBW | Half-Power Beam Width (-3dB) |
| IMPATT | IMPact ionization Avalanche Transit Time diode |
| LTG-GaAs | Low-Temperature Grown Gallium Arsenide |
| MMIC | Monolithic Microwave Integrated Circuit |
| PC | Photoconductive/photoconductor |
| RD-SOS | Radiation-Damaged Silicon On Sapphire |
| SLA | Stereolithography (Apparatus) |
| SWS | Slow-Wave Structure |
| TDS | Time-Domain Spectroscopy |
| TED | Transferred Electron Devices (Gunn diode) |
| TIR | Total Internal Reflection |
| TUNNETT | TUNNEl injection Transit Time negative resistance diode. |
| TWT(A) | Travelling Wave Tube (Amplifier) |
| UTC-PD | Uni-Travelling-Carrier Photodiode |
| UWB | Ultra-Wide Band |
| ZBD | Zero-Biased Detector |

## List of Tables

## List of Figures

# 1. Introduction.

## 1.1 Motivation.

The constant growth in the demand for data rates in wireless networks leads to a continuous increase in the amount of resources allocated per user. This is translated to a continuous demand for more bandwidth. However, the radio spectrum is significantly busy at traditional radio frequencies, while upper parts of the spectrum are scarcely inhabited and offer higher fractional bandwidths.

Millimetre and submillimetre waves are increasingly gaining interest due to their potential applications, among which high data rate communications can be found. These millimetre (30-300 GHz) and submillimetre (300GHz - 3THz) waves are included in the lower part of the traditionally called "**Terahertz gap**", which ranges from 3mm (100 GHz) to 30 μm (10 THz). This terminology was coined due to the immaturity of the technology for generating and detecting waves at these frequencies, in comparison to other mature technologies, such as the ones used at microwave frequencies or infrared optical communications. Nowadays, however, this gap is shrinking due to the recent advances; not only in communications applications, but also and essentially boosted by research in radiometry and spectrometry. In fact, the growth of publications involving "terahertz" has been exponential for the last few decades, as stated in [1] and depicted in Fig. 1 in this work, with up-to-date data retrieved from Scopus.

This Master Thesis has been developed in the framework of the TERALINKS project [2], which is dedicated to the demonstration of a real-time THz communication system in the 200-300 GHz frequency band, in two different scenarios: one outdoor and another indoor. This communication system is thought to operate as a backhaul link, aiming to achieve at least 40 Gbps real-time. As for this Master Thesis, it aims to contribute to the goal of shrinking the aforementioned gap by investigating a new technique for integration and packaging of THz sources that are based of the optoelectronic technique of photomixing.

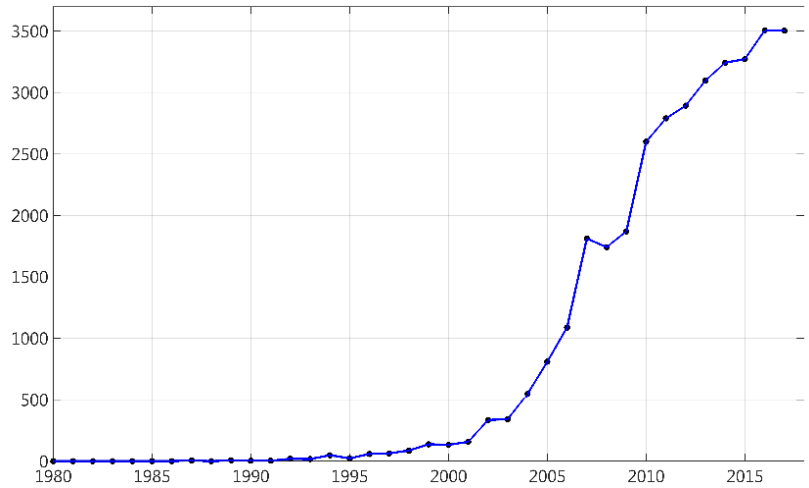

Fig. 1: Terahertz-related publications per year from 1980 to 2017

## 1.2 Objectives.

As part of the TERALINKS project [2], which is dedicated to the demonstration of a real-time THz communication system in the 200-300 GHz frequency band, this Master Thesis will focus on developing a new technique for integrating and packaging a photodiode to be used in a photomixing process for THz generation.

Due to the plethora of challenges present at the THz band, such as atmospheric absorption (Fig. 2), propagation losses and manufacturing tolerances, maximizing the efficiency at power generation seems crucial. For this reason, a new concept of integration block for a terahertz-generating photodiode will be presented in this work. Its most significant feature is the use of an ellipsoidal reflective surface in order to maximize the output power by focalizing all the generated THz power in the same point (one focus of the ellipse), being able to collect the radiated energy and output it into a waveguide (or a transmission antenna). Some of the challenges to be faced in this work include the integration and adaptation of a photomixer (to be designed and delivered by a colleague team in France), the design and analysis of an ellipsoidal reflective surface and the incorporation of different elements to enhance its performance. The optical input will also be studied, in order to integrate the fibre connectors properly into the final device. Due to the lack of specific information about the photodiode, a series of assumptions will be introduced and explained throughout this document. Therefore, this work aims to study different possibilities for designing new structures based on this novel concept, at the same time it presents the design of a specific component. Comments regarding its fabrication will also be made.

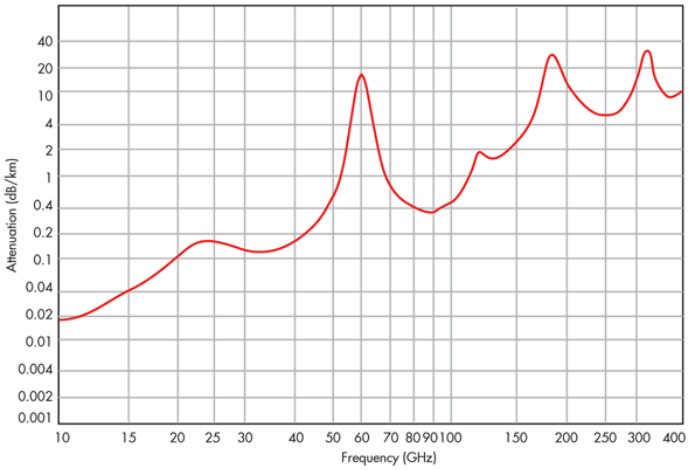

Fig. 2: Atmospheric and molecular attenuation per kilometre [3].

After this introduction, a brief summary of each chapter of the current document is presented next:

*Chapter 2* introduces the context of the TERALINKS project, with its partners, main challenges and goals. *Chapter 3* presents a review of the state of the art concerning the TERALINKS Project and Terahertz in general: THz generation techniques and existing approaches to communication systems in this band. *Chapter 4* provides a brief review of the traditional techniques for packaging and integration of photomixers. *Chapter 5* introduces the geometrical concept of the ellipse and its theory. In addition, it demonstrates the feasibility of this geometric element for its implementation in the packaging of THz sources. *Chapter 6* expands this concept and will detail each of the different steps taken into account in the design of the final device. In *Chapter 7*, some simulation results of the final device will be presented and discussed. *Chapter 8* comments the possible approaches for the fabrication of the component and the results obtained by 3D printing. *Chapter 9* presents the conclusions of this work and draws the future lines of work. *Chapter 10* provides an overview of all the literature consulted in this work, properly referred.

In addition, three appendixes have been included in this work. The first two provide some simulation results, illustrating the relations between the dimensions of some specific parts in the design. They were believed to provide a significantly illustrative view of the best combinations and they effectively summarize the results of large parametric analysis and thus it was decided to include them. The third appendix presents the results of the measuring campaign in both near- and far-field scenarios of a 3D printed and metallized horn designed at 240 GHz. Since this horn was measured during the development of this Thesis and is used in the final system, it was believed to be interesting to include it.

## 2. Context of the TERALINKS Project.

The ever-increasing demand for high data rate and low latency has led to a continuous increase of the carrier frequency and bandwidth allocation. While increasing this carrier frequency allows the allocation of broader bandwidth, it also suffers from higher loss due to propagation and weather conditions. Furthermore, the network is expected to become highly densified [4], with the number of connected devices expected to grow exponentially. For this reason, the user-resources must be allocated on an efficient manner. In order to face both challenges: propagation loss and resource allocation, the optimal solution seems to be *cell splitting*. This is, reducing the coverage area of the base stations (BS), thus increasing the number of BS in the service area. By these means, the number (**n**) of users served by each BS is reduced. This implies that the reutilization of resources is higher and that less interference is generated. Therefore a higher throughput per user (**R**) can be obtained, as stated in [4] and denoted by Shannon' s law, adapted to cell communications, for an error-free situation:

$$R < C = m\left(\frac{B}{n}\right)\log_2\left(1+\frac{S}{I+N}\right) \qquad \text{Eq. 1}$$

Where **B** denotes the base station signal allocated bandwidth [Hz], **m** denotes the number of spatial streams between a base station and a user device, **S** is the power of the desired signal [W] and (**I + N**) are the sum of interference and noise power [W], respectively, measured at the receiver. However, such a large growth in the number of BS requires an infrastructure capable of forwarding hundreds of Gigabit backhaul traffic with a guaranteed quality of service [5]. Observing Shannon's formula, obviating the cell-related parameters, it can be agreed that the capacity of a link can be enlarged by allocating more bandwidth and/or increasing the signal-to-noise ratio (S/N). In fact, there is a trade-off between these two magnitudes. A higher bandwidth implies a shorter transmission time and thus, a higher data rate. However, it also incurs in a higher level of noise in the system. On the other hand, there is a lowest threshold for S/N, below which error rates increase rapidly. This threshold varies depending on the modulation scheme employed.

In this context, some frequency bands, such as IEEE standard designations V-band (40-75 GHz) and W-band (75-110 GHz) – which have traditionally been used for satellite, radar and scientific research – are recently been proposed to develop **backhaul systems**. The allocated frequencies only include, however, part of these bands, being available only the following portions: 57 – 66 GHz, 71 – 76 GHz, 81 – 86 GHz. These portions of spectrum are not suitable for the purpose of the TERALINKS project, where an initial goal of 40 Gbps has been set.

In this project, 240 GHz has been selected as the target carrier frequency due to the good comprise between, first, atmospheric and propagation losses and second, current technology and technological challenges [6]. One of these challenges is the generation of power, in order to achieve an adequate S/N. Higher S/N allows the utilization of higher spectrum-efficient modulation schemes and thus higher capacities. In order to generate enough THz power, the combination of photonic-based sources and travelling wave tubes (TWT) has been chosen.

## 2.1 Partners.

The **TERALINKS** (***TERA****hertz high power* ***LINKS*** *using photonic devices, tube amplifiers and Smart antennas*) Project aims to demonstrate a real-time THz communication system within the 200-300 GHz frequency range in an operational environment. For this purpose, three key enabling technologies are considered: **photonics-based THz sources**, **Traveling Wave Tubes** (TWTs) for high THz power generation and **Smart Antennas**. It is a European project[1] driven by a handful of partners, mainly European universities, which have been lately involved in the THz field of research.

- University Lille (IEMN).
- University of Nice (EpOC).
- Queen Mary University of London (QMUL).
- Lancaster University (LU).
- **Universidad Pública de Navarra** (UPNA).


Fig. 3: TERALINKS Project logo

As well as two industrial partners:

- ST-Microelectronics.
- THALES.

[1] CHIST-ERA is a program for European Coordinated Research on Long-term Information and Communication Technologies. Every year, a transnational call for research proposals is launched. TERALINKS corresponds to the Call from 2015.

## 2.2 Goals

Essentially, the project aims to achieve a real-time communication link of at least 40 Gbps (fixing 100 Gbps as the ultimate target), at a centre frequency of 240 GHz. In addition, two different scenarios are considered in this project:

- **Outdoor** point-to-point link for future cellular network backhaul (1 kilometre).
- **Indoor** high speed networks (up to 10 to 20 metres).

These transmission scenarios have different power link budget conditions, as in (a) high directivity antennas and high radiation efficiency are required in order to compensate the attenuation due to propagation loss, gas absorption and critical weather conditions such as rain or fog; while in (b) high directive antennas are substituted by beam-steerable advanced designs, propagation losses are not as critical as in a) due to the reduced distances and weather conditions are no longer critical. On the other hand, line of sight (LoS) could be compromised due to obstacles such as furniture or even people. In both scenarios, the targeted bandwidth of operation is 240 ± 20 GHz; namely, 40 GHz must be available for the link operation. In order to achieve the initial goal capacity, i.e. 40 Gbps, simple modulations, such as ASK, and direct detection could be used. The technology to achieve this has already been demonstrated [7], [8] by using Schottky-based receiving systems and photomixing techniques.

Higher or similar bitrates to the proposed target have already been achieved in the recent years employing different techniques, such as multiple transmission channels in parallel (8 channels of 25 GHz achieving together 160 Gbps, as reported in [9]), or higher carrier frequencies [8] (46 Gbps at 400 GHz). Although these implementations successfully reported very interesting data rates, the achieved working distances were roughly less than a few metres, thus they are not comparable to the main goal of this project for the outdoor scenario (although they are not far from the indoor scenario).

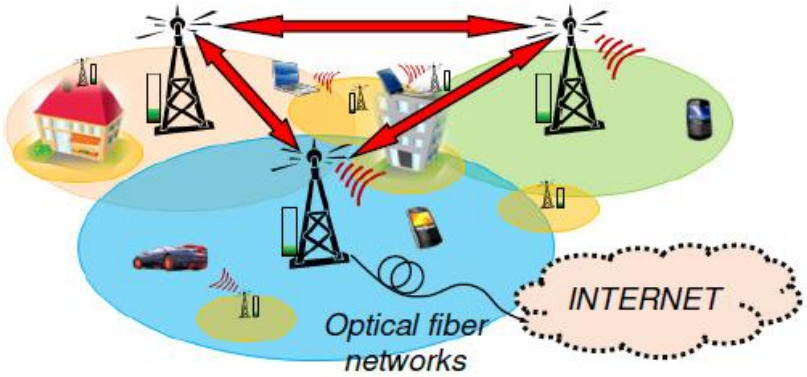


Fig. 4: Outdoor scenario scheme

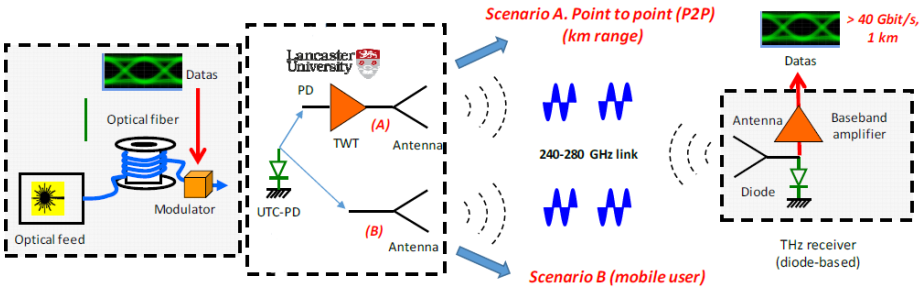


Fig. 5: Wireless link architecture for both scenarios considered in TERALINKS

Nevertheless, the technologies employed in these contributions successfully achieved similar or even higher data rates and it could establish an interesting starting point. In terms of the link budget, higher available output power and more directive antennas could improve the reachable distance. On the other hand, other type of mechanisms, such as forward error correction, could be implemented in order to decrease the BER of the system and therefore, obtain higher data rates. These error correction mechanisms are out of scope from this Master Thesis and will not be mentioned in the following sections. Nevertheless, they should be taken into consideration in the final implementation of the communication link.

Focusing on the outdoor scenario (Fig. 4), where a distance over one kilometre is required, one remarkable, real-time implementation driven in 2012 by NTT in Japan must be highlighted, in which a 120-GHz-band wireless link achieved a 10 Gbps transmission over a distance of 1 km in heavy rain condition with 99.999% availability and above 5km in conditions of fine weather [10]. Hence, the goal considered by the TERALINKS project for the outdoor scenario stands out as an ambitious target, entailing a four-time increase in link capacity regarding to the state of the art design by NTT.

Table 1: Main specifications of the wireless link to be developed in TERALINKS

| | |
|---|---|
| **Frequency** | 220 – 260 GHz |
| **THz source power** | Up to 1mW |
| **TWT power amplifier** | Gain > 30 dB<br>Power: 3-4 W |
| **Receiver** | Zero Bias Schottky Detector<br>responsivity 1kV/W |
| **Rx bandwidth** | 40 GHz, including baseband amplifier |
| **Modulation** | ASK (real-time)<br>40 Gbps |

As for the receiver, TERALINKS project has chosen to include a Zero Bias Detector (ZBD) based on Schottky diodes. This device is commercially available, due to the current capability of these devices to detect up to 50 Gbps. Thus, no attention will be paid to this device and efforts will be concentrated on the THz emitter. The main specifications of the communication system are presented in Table 1.

In the next Chapter, a review of the main technologies for THz power generation and communications will be presented and special interest will be paid in some of the aforementioned key enabling technologies: photomixing techniques and travelling wave tubes.

# 3. Terahertz technologies for communication systems.

In the last few decades, the **terahertz gap** has been reduced significantly, pushed initially by research in radio astronomy and spectroscopy, boosted by sensing and imaging techniques. Other newer applications related to imaging include Ultra-Wide Band (UWB) high resolution radars [11] and biomedical imaging to replace X-rays [12]. Nowadays, high speed communication systems based on terahertz are on the horizon and diverse studies have already been successfully performed. This denomination of "gap" was coined due to the underdevelopment of the technologies for generating THz with respect to electronic techniques, operating in frequencies below this gap; and photonic techniques, operating right above this band. Up to date, a plethora of techniques for THz generation have been developed and this gap is gradually being filled by new research. Different classifications of these techniques can be found in the literature. These diReffer among each other in singular details but all in all, three main categories can be differentiated: electronic sources, photonic sources and a subtype of this photonic sources, the optoelectronic sources. **Electronic sources** comprehend mainly vacuum tubes, solid state oscillator devices and frequency multipliers. Recent efforts have also been made in research of plasmonic sources. On the other hand, photonic **sources** include gas lasers and semiconductor lasers, among others. Finally, a third hybrid group should be highlighted: **optoelectronic sources**. In fact, this last group will be analysed in detail, due to the enormous development that has experienced in the recent decade and due to the fact that an optoelectronic technique will be chosen for THz generation in the TERALINKS project.

Some of the most relevant techniques of each group will be presented in order to comment on their advantages and drawbacks. Additionally, some examples of the state of the art in these techniques will be given. A brief review will also be made about recent approaches in developing operational, real time, THz communication systems.

Since TERALINKS project does not focus on the detection technologies, rather chooses a commercial Zero-Bias Schottky Detector [13], no attention will be paid to this particular component, since it has been considered out of the scope of this Master Thesis. Nevertheless, a characterisation of this diodes can be found in [14], as well as in the referred web page.

## 3.1 Electronic sources

### 3.1.1 Vacuum Tubes and Electron-beam Devices

A vacuum tube, also called electron tube, is a device capable of controlling the electric current between two electrodes in a container that can be evacuated (vacuum) or gas-filled. Among its applications, they are used in generating high power at radio frequencies. Regarding the terahertz region, different examples can be found, such as the Free-Electron Laser (FEL), the Backward-Wave Oscillator (BWO) or the Travelling Wave Tube (TWT).

**Free-Electron Lasers** are based on the fact that an electron, travelling through a stationary electric or magnetic field, radiates, being its wavelength dependant on the speed of the electron [15]. In FELs, a beam of electrons inputs an undulator – an array of N pairs of magnets with alternating poles – and is accelerated by this alternating field distribution due to the Lorentz Force, making the beam travel across the undulator with a sinusoidal trajectory, on a plane normal to the magnetic fields. The cavity is enclosed by a pair of mirrors, thus creating standing waves in the inside. The result of the interference between the waves generated by the electrons on each period of the undulator gives a constructive, coherent radiation at a frequency controlled by the speed of the electrons and the magnetic fields of the cavity [16]. FELs provide possibly the highest levels of output power. However, these systems require expensive and massive-sized facilities and enormous amounts of power consumption. One example is found in [17] and an approximated view of the size of these facilities is shown in Fig. 6.

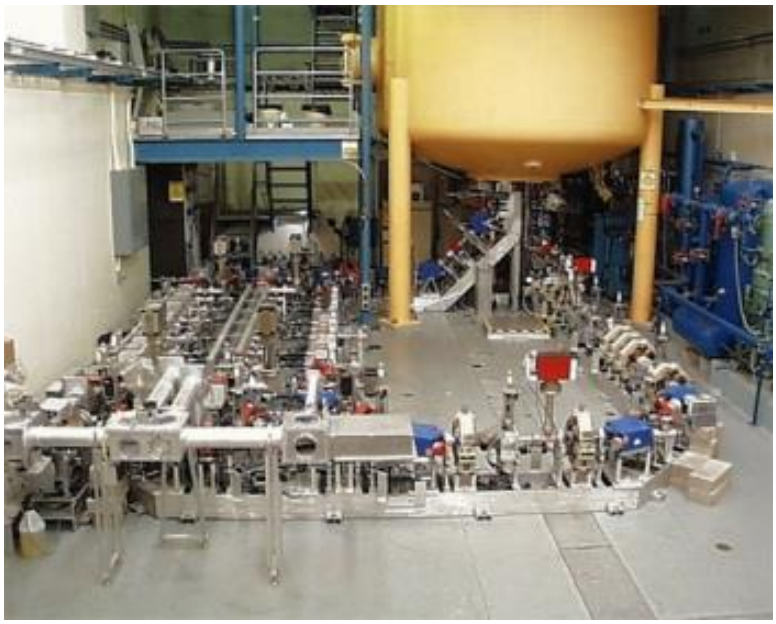

Fig. 6: UCSB Free-Electron Laser facility [18].

**Backward Wave Oscillators** could be considered as table-top, small brothers of FELs [19]. An electron beam is generated by an electron gun (such as a Gunn diode) and interacts with a slow-wave structure (SWS) instead of an undulator. The density of electrons in the beam is modulated, grouping electrons (microbunching) by the repulsion or attraction in areas with low or high bias. This modulation corresponds to the relative amplitude of the input RF signal. This is translated in an amplified version of the signal. The output signal travels opposite to the electron beam, hence the name "backward wave". Nevertheless, the output frequency is controlled by the speed of the electrons and thus it can be changed by modifying the bias voltage [20]. Operation can take place also in the absence of an input signal. Therefore, BWO are not only THz amplifying devices [21], but also THz sources [22]. Some remarkable, recent works proved a peak power of 110mW at 260 GHz [23]. Other studies provide interesting simulation results, obtaining several Watts of output power at 340 GHz or 650 GHz. A conclusion that can be extracted from reviewing the related literature is that the design and manufacture of the SWS unit cells are driving tasks in the design of this devices.

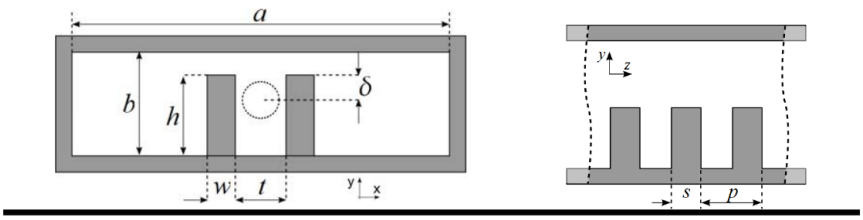


| Param. | *a* | *b* | *p* | *s* | *h* | *w* | *t* |
|---|---|---|---|---|---|---|---|
| μm | 530 | 380 | 360 | 80 | 210 | 80 | 150 |

Fig. 7: Example of SWS cell unit, with dimensions, extracted from [24].

The principle of work for the **Travelling Wave Tubes** is fundamentally the same as that of the BWO. An electron beam is injected in a tube in presence of a RF signal to be amplified. The tube typically includes a slow-wave structure (or a helix wire, but this type of structures do not support very high power). With this kind of structures (SWS), the electromagnetic waves are slowed down, so that their phase velocity is similar to the electrons' speed, which is controlled by the voltage bias. With much more comparable speeds, it is possible for the electrons to interact with the signal, being modulated by it. TWTs are commonly used as amplifiers rather than THz sources, although some studies have dealt with this [25]. As has just been presented, both BWO and TWT are significantly similar, with the difference of the direction of the output signal and a higher tuning capability for the BWOs. In TWTs, phase velocity and group velocity have the same direction, while in BWO the group velocity has an opposite direction. For this reason,

it could be thought that they could share the same SWS. That is the case in [24], where a multiple beam BWO is presented, based on the Double Corrugated Waveguide TWT in [26]. In these works, an output power of 45W and 3W, respectively, were obtained over a 30 GHz bandwidth at 220 GHz. In fact, these works were driven by one of the colleagues participating in the TERALINKS project, and a similar device is expected to be designed for power amplification, to be placed right after the device that will be presented in this Master Thesis.

### 3.1.2 Solid State Oscillators

There are several types of solid state devices that can be used as THz sources, such as Gunn diodes (also known as Transferred Electron Devices, TED), Resonant Tunnelling Diodes (RTD), Transit Time diodes (such as IMPATT or TUNNETT) or transistors. These devices are characteristic for their **negative resistance or negative conductance** at some parts of their current/voltage curves, being suitable for working as **oscillators**. A review of these devices can be found in [27]. The main goals in the development of these devices are the up-scaling in frequency and obtaining higher output powers. However, as a rule of thumb, scaling in frequency implies a higher number of drawbacks in the designs due to miniaturization (which carry thermal and electrical constrains) and manufacturing tolerances. In fact, while solid state electronics are expected to enable low-cost and integrated THz power generation, the output powers obtained to date are still low, since they suffer from several fundamental issues including reactive parasites, high resistive losses or high-frequency roll-off [28], yet some recent results are promising. Some examples have reached the order of milliwatts, as in [29], were almost 0.2mW were obtained with an RTD. In [30], a 3 Gbps transmission with a BER of $3 \cdot 10^{-5}$ was achieved as well with an RTD oscillating at 542 GHz and an output power of 0.21mW. Recently, a 22 Gbps error-free transmission was achieved with a broadband RTD at 490 GHz with an output power of 0.06mW.

As for solid state amplifier devices, heterojunction bipolar transistors (HBT) have been proved to provide more than 20 dB small-signal gain over a bandwidth of 40 GHz around 290 GHz, with a peak output power of 10mW [31]. Other technologies include High Electron Mobility Transistors (HEMT) – transistors made of several layers of different semiconductors and thus different bandgaps, where the discontinuities provide high mobility to the electrons – and metamorphic HEMTs (which are HEMTs grown on non-lattice-matched substrates). These technologies are explained and a detailed review of their state of the art is presented in [32].

### 3.1.3 Frequency Multipliers

When operating at very high frequencies is required, such as THz, solid state oscillators start to not being able to provide power and other solid state alternatives must be implemented. This is the case of frequency multipliers. These devices take advantage of non-linear effects to generate harmonics from an input signal. These multipliers are essentially based on non-symmetrical devices such as Schottky diodes or symmetrical components such as HBVs (Heterostructure Barrier Varactor) [19].

Schottky diodes made from GaAs are the most common device for building multipliers due to its fabrication process simplicity, low DC power consumption and low parasitic. However, they are generally used only for multiplication factors of 2 or 3, due to low conversion efficiency and chains of multipliers are often required to reach THz frequencies. On the other hand, configurations including HBV allow a more efficient realisation of higher multiplication factor, such as frequency quintuplers [33]. This is feasible due to the symmetry of the device, which allows to cancel the generation of even harmonics. These devices provide a handling of higher output powers in comparison to Schottky diodes, since they include several junctions in series, stacked during epitaxial growth, although they require a much more complex engineering process [19].

The current status and state of the art of frequency multipliers is analysed in depth by [34] and [35]. Some interesting results regarding HBV include the realisation of a frequency septupler (x7) at 240 GHz [36], although power under the milliwatt level was achieved. Other studies achieved up to 60mW in a frequency quintupler (175 GHz) [33] and 240 mW in triplers around 110 GHz with a conversion efficiency of 20% [37]. It should be highlighted that these designs are all narrowband. As for Schottky-based multipliers, state-of-the-art designs offer bandwidths of around 15-20% and efficiencies around 30%. Furthermore, frequencies up to 3 THz have been achieved [38]. Some examples include 42.5% efficiency at 190 GHz with 90 mW output power doubler [39] or a 160 GHz quadrupler with 70 mW output power and 29% efficiency [40].

## 3.2 Photonic Sources

### 3.2.1 Semiconductor Lasers

Quantum cascade lasers (QCL) are compact, narrow line-width, semiconductor THz sources. Their body is composed of hundreds of layers containing quantum wells and barriers, which together determine the wavelength of operation. In these devices, electrons undergo quantum jumps between conduction subbands formed within a superlattice of quantum wells structure [19]. These layers are very thin and its energy transitions correspond to the THz region. They can be designed to radiate over a wide range of frequencies/wavelengths, outperforming diode lasers in terms of power handling capability. However, in contrast to solid state electronics, operation in lower frequencies is challenge-increasing. They usually require cryogenic temperatures to operate properly, although some recent studies suggest the feasibility of obtaining room-temperature QCLs [41], [42]. The output power levels obtained result very attractive, but they suffer from limited bandwidth and low tunability, and require frequency stabilization. Some examples of achievable powers are collected in [43], with up to 1W @ 3.4 THz at a temperature of 118K, and [44], with 3W at 65 THz (4.6 microns) at room temperature.

Another table-top technique is the p-Ge laser. It consists of a germanium crystal doped with acceptors such us beryllium, zinc or gallium, among others. The crystal is placed in between crossed electric and magnetic fields and the holes are accelerated, resulting in population inversion that leads to stimulated emission [45]. It is often used in spectrometry and requires cryogenic working temperatures, reason why a cold plate is placed [46].

### 3.2.2 Gas Lasers

Gas lasers are other candidate sources of coherent power at the upper end of this frequency range. They use polar molecules as the laser medium, obtaining THz radiation from spectral resonances of molecular rotations together with a specific cavity. The gas cell is pumped with an infrared laser, such as CO2 laser. One fundamental limitation is that operating frequencies are limited to those of molecule-specific resonances [19].

## 3.3 Optoelectronic Sources

Up to this point, different photonic and electronic techniques for THz generation have been presented. As it has be shown, each technique presents its own advantages and drawbacks in comparison to each other. While one driving limitation of optical terahertz sources lies in the low photon energy at this frequencies, in the order of meV (and the lack of materials which such a small bandgap), solid-state devices based on semiconductors, such as amplifiers, oscillators and frequency multipliers, suffer from low conversion efficiencies and stability problems. Other drawbacks of high power, photonic sources are either the need of very low operation temperatures or the need of a whole room in order to host the equipment, as in the case of FEL. Nonlinear THz generation employing non-linear crystals has also been presented, reporting low power efficiency. Similarly to the idea of frequency up-conversion by frequency multipliers, THz generation could be achieved by down-conversion techniques from optical sources. These are usually referred to as **optoelectronic** techniques and two main methods are generally differentiated: **continuous wave** (CW), narrow-band THz generation by photomixing of two photocarriers with a wavelength difference corresponding to the frequency of interest (THz) and broad-band generation by **pulsed operation**. This is, generating short pulses, in the order of femtoseconds, with an optical laser and the use of some photoconductive film. Both solutions require a small photoconductor connected to a pair of electrodes for bias feeding. This photoconductive material is irradiated by the optical beams (or pulses) in order to generate currents in the terahertz band that will be coupled to an RF antenna or circuit working at the frequency of interest. Pulsed operation is known as Time Domain generation (TD) while CW is known as Frequency Domain generation (FD).

### 3.3.1 Pulsed Emission

Terahertz pulses can been generated by irradiating a photoconductive (PC) antenna, quantum structures or a semiconductor surface with femtosecond optical pulses [47]. The use of photoconductive antennas has been historically the most recursive. A standard pulse generation scheme using a PC antenna is shown in Fig. 8. A short optical pulse, in the order of femtoseconds, irradiates a photoconductive material placed onto a semiconductor substrate with a printed THz antenna that is biased with a DC voltage. This optical pulses must have an energy greater than the bandgap of the semiconductor, in order to be absorbed. This absorption generates electron-hole pairs that are generated in the conduction and valence bands, respectively. The bias voltage generates an electric field that accelerates the carriers, which have a specific carrier lifetime until they are relegated back to the valence band. Therefore, a THz photocurrent is induced

in the structure, and the emitted THz field is proportional to the first derivative of this photocurrent [19].

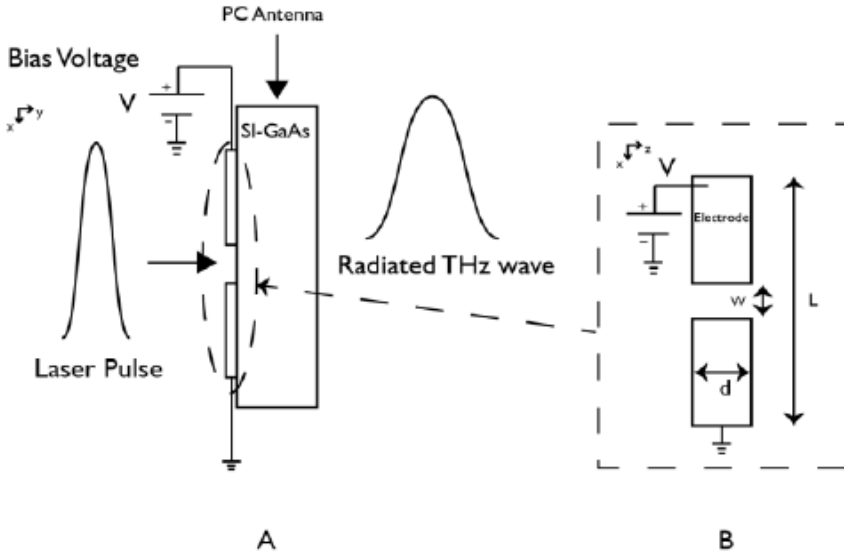


Fig. 8: Scheme of THz pulsed radiation by means of photoconductive antenna [48].

When calculating the frequency spectrum of the emitted signal, one could expect a broadband response. This is according to the Fourier theorem, which states that the spectral width is inversely proportional to the temporal width. In fact, as explained in [47], the spectrum of the photocurrent is ideally proportional to the spectrum of the optical pulse. Thus, it can be agreed that the optical pulse duration must be much shorter than the period of the maximum THz frequency whose generation is desired.

$$E_{THz}(t) \propto \frac{dI_{ph}(t)}{dt} \qquad \text{Eq. 2}$$

$$E_{THz}(\omega) \propto FT\left[\frac{dI_{ph}(t)}{dt}\right] = i \cdot \omega \cdot I_{ph}(\omega) \qquad \text{Eq. 3}$$

Nevertheless, when a photon is absorbed, it generates an electron-hole pair that is at rest and must be accelerated by the bias electric field. This will subsequently take an amount of time that will make the THz pulse temporally broader than the incident optical pulse. As for the photoconductive materials, the most commonly used are RD-SOS (Radiation-Damaged Silicon on Sapphire) and more recently LTG-GaAs (Low-Temperature grown), due to their short carrier life time (under picoseconds), their relatively high carrier mobility and high breakdown voltage.

In addition to photoconductive antennas, the generation of THz pulses can be achieved by other means such as semiconductor quantum structures, optical rectification in non-linear media, excitation of optical phonons and

other techniques, presented in [47]. Pulsed emission techniques are often used in time-domain spectroscopy and thus they won't be analysed any further in the current work because they are not considered in the frame of the TERALINKs project.

Moreover, two major drawbacks concern TD generation: limited frequency resolution and limited available power per frequency, since the generated pulse may have a significant power, but this power must be divided among all the frequency components.

### 3.3.2 Continuous-wave Generation

When referring to continuous-wave THz generation by optoelectronic means, the idea that must come to our mind is photomixing. Photomixing is a technique consisting of exciting a semiconductor or photoconductive material with a pair of lasers, whose optical frequencies $(\nu_1, \nu_2)$ differ in frequency by the desired THz frequency to be generated. The following mathematical explanation is extracted from Chapter 2.2 in [19].

$$\nu_{1,2} = \bar{\nu} \pm f_{THz}/2 \qquad \text{Eq. 4}$$

Each of the irradiating lasers can be expressed as an electric field strength $\overrightarrow{E_1} \sim \sqrt{P_1}$ and $\overrightarrow{E_1} \sim \sqrt{P_1}$ . These lasers are heterodyned - in fact, photomixing has also been referred to as "optical heterodyning" for many years - in the photomixer, resulting in a total optical field strength of:

$$\begin{aligned} \vec{E}(t) &= \vec{E}_1(t) + \vec{E}_2(t) \\ &= \vec{E}_1 \cdot e^{i(\bar{\omega}+\frac{\omega_{THz}}{2})t} + \vec{E}_2 \cdot e^{i\left(\bar{\omega}-\frac{\omega_{THz}}{2}\right)t - i\varphi} \end{aligned} \qquad \text{Eq. 5}$$

Where $\omega$ represents the angular frequencies and $\varphi$ is the relative phase between both waves. The optical intensity is proportional to the square of this optical field strength and shows the heterodyning process and the generation of an individual THz component:

$$\begin{aligned} I_L(t) \propto \left|\vec{E}(t)\right|^2 = E_1^2 + E_2^2 + \\ 2 \cdot \left|\vec{E}_1 \circ \vec{E}_2\right| \cdot (\cos(\omega_{THz} t + \varphi) + \cos(2\bar{\omega} t - \varphi)\,) \end{aligned} \qquad \text{Eq. 6}$$

The high frequency component, sum of the frequencies of both lasers can be neglected because it varies on a time basis much shorter than the carriers' lifetime and thus its effect on the modulation is not significant. For instance, if the central wavelength of the lasers would be 1500 nm (which corresponds roughly to 200 THz), twice this frequency would have a wave period of 2.5 fs. Photoconductive materials often employed in this techniques have carrier

lifetimes of picoseconds or several hundreds of femtoseconds and thus the signal with such a small period can be neglected. In the end, the photoconductor/photodiode acts as a square law detector, filtering out the high frequency.

Eq. 6 can be expressed in terms of optical power. Developing the dot product of the incident laser beats, the angle between the polarizations of the lasers, $\beta$, appears. The optical power is maximized for the case where both lasers have identical power and polarization. In addition, it can be observed that there are no phase matching problems.

$$P_L(t) = P_1 + P_2 + 2 \cdot \sqrt{P_1 P_2} \cdot \cos(\beta) \cdot \cos(\omega_{THz} t + \varphi) \qquad \text{Eq. 7}$$

This optical power modulates the photoconductance of the semiconductor, generating a photocurrent. In this process there will be losses due to the non-ideality of the process. The photocurrent generated in an ideal semiconductor is presented in Eq. 8, were h is the constant of Planck and e the charge of the electron:

$$I_{Ph}^{id}(t) = \frac{eP_L}{h\bar{\nu}} \qquad \text{Eq. 8}$$

Sakai [47] proposes an equivalent circuit of a photomixer connected to an antenna. It is shown in Fig. 9. From this circuit, one can extract the dynamic current equation and, as solved in Eq. 9, the output THz radiated power:

$$P_{THz}(\omega) = \frac{I_{Ph}^2 \cdot R_A}{2[1 + (\omega_{THz}\tau)^2][1 + (\omega_{THz} R_A C)^2]} \qquad \text{Eq. 9}$$

From this expression, it can be agreed that output power decreases with higher frequencies. On the other hand, it increases in proportion to the square of the photocurrent induced and thus, in proportion to the incident optical power.

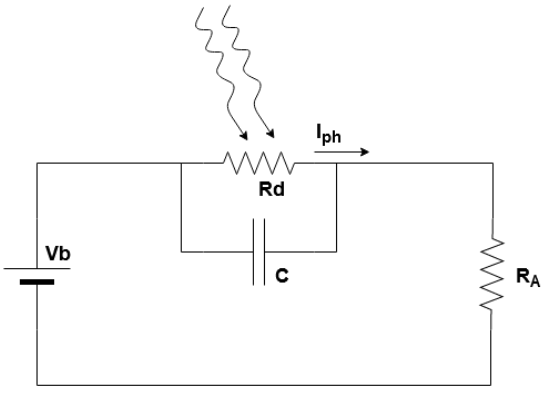


Fig. 9: Equivalent circuit of CW photomixing device.

Compared to TD techniques (pulsed operation), photomixing offers a series of advantages. The most evident is that it generates a single frequency, concentrating all its energy on that single mode, and thus offering a higher SNR. Moreover, this technique offers the highest range of tunability in THz generation. This is due to the fact that it uses two laser beams that can be tuned by several to tens of nanometres. For example, the frequency of interest for the TERALINKS project, 240 GHz, corresponds to a wavelength difference of 1.8 nm at 1,550 nm. On the other hand, when using two independent laser sources and combining them, uncorrelated noise can impact negatively, producing poor frequency stability and large phase noise. Nevertheless, different techniques have been proposed to overcome this issues. These include the use of an external modulator MZM (Mach-Zender) together with a RF signal half of the frequency of interest. At a specific biasing point, the non-linear transfer function of the MZM generates an optical dual sideband signal with suppressed carrier. These sidebands are separated by a frequency that is twice the frequency of the RF signal. Therefore, it is possible to generate two optical modes with coherent phases. This approach is presented in [49].

Another solution is to achieve phase locking of two individual lasers by a double arm OPLL (optical phase-locked loop) as the one shown in Fig. 10, where "Laser Filter" stands for an OPLL circuit with narrow bandwidth. This was presented in [50], and it allows to reduce phase noise as well as increase stability. For this, an optical reference is extracted from an optical comb generator (OCG)[2], locking each of the lasers to a pair of wavelengths of the OCG.

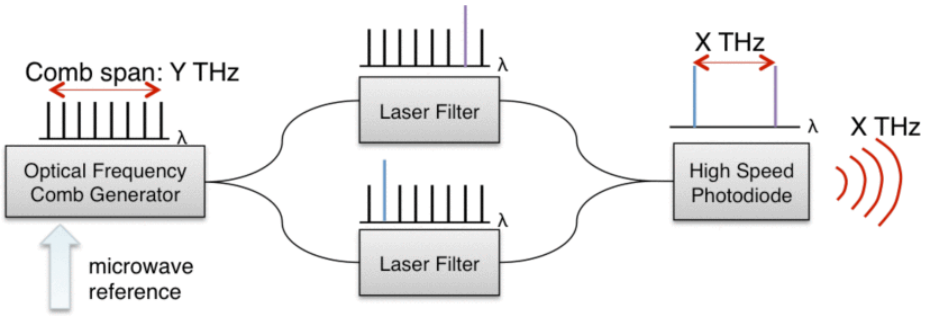


Fig. 10: Scheme of the photonic oscillator based on the dual optical filter [50].

[2] An Optical Comb Generator is a source of multiple optical wavelengths separated equidistantly from each other. Ideally, all of them are phase-locked to each other.

### 3.3.3 Types of Photomixers

There are essentially two differentiated types of photomixers: p-i-n diode based mixers and photoconductive mixers, both made from semiconductors. A brief explanation of both will be provided in this section. Special attention will be paid in p-i-n diodes and the different methods to overcome its drawbacks, among which UTC-PD are included. The book [19], provides a detailed insight on this semiconductor devices and it is referred for further study of this matter.

#### 3.3.3.1. Photoconductive Mixers

A photoconductive mixer consists of a highly resistive semiconductor, covered with metallic contacts working as electrodes. This semiconductor receives photons with an energy higher than its band gap and generates electron-hole pairs. Since there is no built-in field, applying an external DC bias is required to create an electric field capable of separating the carriers and thus generate a photocurrent.

The materials used for this devices require a low carrier lifetime, so that they are recombined on their way to the electrode, improving the transit time roll-off. The higher the DC bias voltage, the stronger the electric field generated and thus the faster the carriers move across the device. Thus, the field breakdown of this materials must be high, in order to support high bias voltages, which can range from a few volts to 100 V [19].

Photoconductors have been developed for both 800 nm and 1550 nm (first and third windows in optical communications). Gallium arsenide, GaAs, is one of the work horses for photoconductive devices. It has a very high dark resistance, so that there are practically no thermally generated carriers. However, due to its large band gap, 1.42eV, it can only be used with wavelengths shorter than 870nm (namely, it is only used at 800nm). Nevertheless, GaAs is the basis of a plethora of materials, such as Low Temperature Grown GaAs, which features a carrier lifetime lower than a few hundreds of femtoseconds and a breakdown field twice higher as GaAs. Other materials include InAlAs[51], ErAs:GaAs [52] and InGaAs[53], for operation in both 800 nm and 1550 nm.

#### 3.3.3.2. p-i-n diodes

A p-i-n diode consists of a p-doped semiconductor, followed by an undoped semiconductor part (intrinsic), also called the absorption layer, and an n-doped semiconductor. The bandgaps of the doped regions are increased by adding other materials, such as aluminium, exceeding the photon energy, so that the absorption can only take place in the intrinsic layer. An electric field is formed in the intrinsic region, of length $d_i$, due to the p- and n-concentrations surrounding it, with a field strength of $E_i = E_G/d_i$, being $E_G$ the bandgap of the intrinsic semiconductor. Each absorbed photon generates an electron-hole pair that contributes to the photocurrent. However, there are some mechanisms that limit its efficiency.

First of all, some of the laser power will be reflected by the semiconductor surface, with a reflection coefficient R. Nevertheless, this can be minimised by applying an anti-reflection coating.

Secondly, the device has a finite absorption length and an absorption coefficient $\alpha$. This limits the total photocurrent that can be generated by the device and thus, the output power. This reduction is summarized in the external THz quantum efficiency, Eq. 10, where the square dependency comes from the same relation between THz power and photocurrent, shown in Eq. 9 in the previous section.

$$\eta_{ext} = (1 - R)^2 \cdot [1 - \exp(-\alpha d_i)]^2 \qquad \text{Eq. 10}$$

Furthermore, every electronic device has a capacitance, which becomes problematic at higher frequencies. This capacitance is parallel to the antenna's radiation resistance and at high frequencies can be problematic. This capacitance corresponds to that of a plate capacitor with a spacing of $d_i$ (the length of the intrinsic region) between plates. The capacitance shorts the antenna, reducing the power delivered. This is called the **RC roll-off**.

$$\eta_{RC} = \frac{1}{1 + (2\pi R_A C_{pin} f_{THz})} \;\; ; \;\; C_{pin} = \varepsilon \frac{A}{d_i} \qquad \text{Eq. 11}$$

Finally, there is another roll-off, caused by the transport of carriers inside the diode. Carriers generated at different times cause currents that interfere with each other. This is called the **transit-time roll-off** and the envelope of its roll-off function can be estimated by Eq. 12, where $\tau_{tr}$ is the transport time of the carriers and $v_{sat}$, the electrons saturation velocity.

$$\eta_{tr} \approx \frac{1}{1 + (2\tau_{tr} f_{THz})^2} \;\; ; \;\; \tau_{tr} = \frac{d_i}{v_{sat}} \qquad \text{Eq. 12}$$

One way to overcome this transit-time roll-off could be reducing the transport length, $d_i$, however, this would increase the capacitance and thus the RC roll off presented in Eq. 11. Reducing the cross-section of the device, the capacitance would be reduced. However, this would increase the optical power density and the maximum photocurrent would be limited due to thermal and electrical constraints. Therefore, THz power would be significantly reduced, given the square-proportional relation with photocurrent. Another option for easing this roll-off could be increasing the speed of the carriers over the velocity of saturation, what is called "velocity overshoot". This would decrease the transport time of the carriers without affecting the RC roll-off. Unfortunately, whereas this is possible for the case of electrons under high fields, holes are significantly slower. Nevertheless, there are techniques that compensate this by generating holes very close to the p-contact, in order to keep the transport length minimised and thus preventing them from affecting the roll-off. This is the case of **Uni-Travelling-Carrier photodiodes** (UTC-PD). In these devices, a doped semiconductor layer with a bandgap lower than the energy of the photon (absorption layer) followed by a layer of intrinsic semiconductor with a band gap higher than this energy are placed next to the p-contact. With this layers, electron-hole pairs are generated in the vicinity of the p-contact, allowing holes to drift almost immediately and thus making the electrons the only carriers that are transported. The diffusion block layer stops electrons from travelling to the p-contact, being accelerated towards the n-contact through an n-type collection layer.

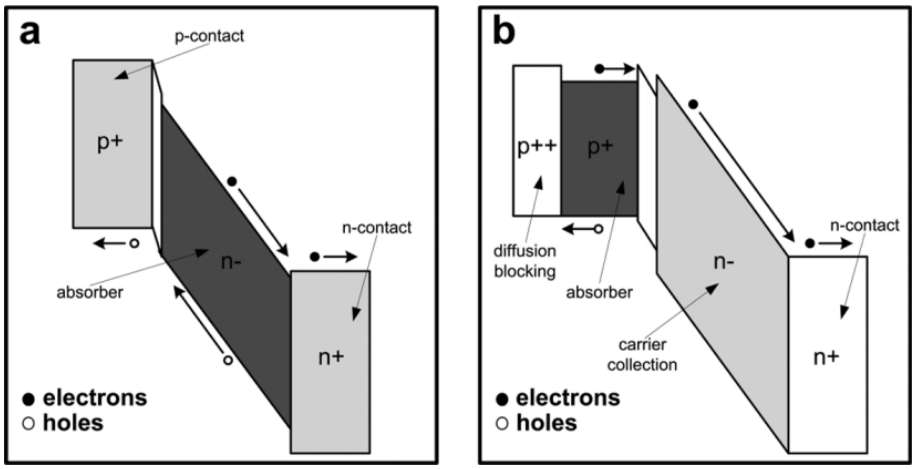


Fig. 11: Schematic band diagrams of (a) p-i-n photodiode and (b) uni-traveling carrier photodiode [54].

The original design of the UTC-PD was presented in 2005 by NTT, working at 1.04 THz and featuring an output power of 2.6 μW with a broadband antenna and 10.9 μW with a resonant antenna [55]. From there,

a plethora of designs have been proposed, modifying the layer structure and doping strategies, as well as including different antenna designs, in order to optimise bandwidth an responsivity, such as in [56], [57]. This is the type of device that will be employed in the TERALINKS project and whose integration will be studied in this work. Its design, however, will be carried out by the team at IEMN, in Lille. This team has a broad experience in the design of UTC-PD. Some examples can be found in [58]–[60].

Most of the diodes are backside illuminated, this is, through the substrate. Others use a refracting facet or waveguide illumination. These ways of illuminating are inconvenient due to measurement and integration issues and a front-side illumination shall be preferable in order to overcome this problems. This is achieved in [59], where a semi-transparent metallic contact (with subwavelength periodic apertures) is placed on top of the device, allowing direct irradiation while offering a low contact resistance. This contact, together with a resonant cavity, demonstrates record values of efficiency and provides up to 0.75W at 300 GHz. Furthermore, it has been recently used to demonstrate a 100 Gbps transmission for future IEEE standard 802.15.3d [61].

### 3.4 THz Communication Systems

The potential of THz communications for ultra-high bit rates is pushing the research of the field of terahertz communication systems. However, due to atmospheric gas absorption and inclement weather, as well as lack of high available, output power sources, the realisation of long range communications remains difficult. To date, only a few examples using terahertz ($0.1 - 10$ THz) in long-range communications have been reported. Currently, the longest real-time wireless communication demonstrated achieved a 5 Gbps rate over 21km wireless link with ha BER of $10^{-12}$ [62]. Here, a 16-QAM modulation scheme was used at a frequency of 140 GHz. A Ku-band mixer and terahertz harmonic mixer together with two local oscillator were employed for IF to RF conversion. MMIC power amplifier is cascaded together with a TWT in order to amplify the power from -24dBm to 26.3 dBm. A scheme of the system is shown in Fig. 12.

As briefly commented in Chapter 2, one of the most remarkable works with regards to TERALINKs project was presented by NTT in 2010 [10], where a 120-GHz-band wireless link was demonstrated with a 10 Gbps bit rate over a distance of 1 km in heavy rain condition with 99.999% availability and above 5km in conditions of fine weather. Three years later, a 10 Gbps non-real time communication was achieved over a 1.5 km link using 16-QAM modulation in 140 GHz band. However, the fact that communication was not real time makes the work of Hirata [10] more remarkable.

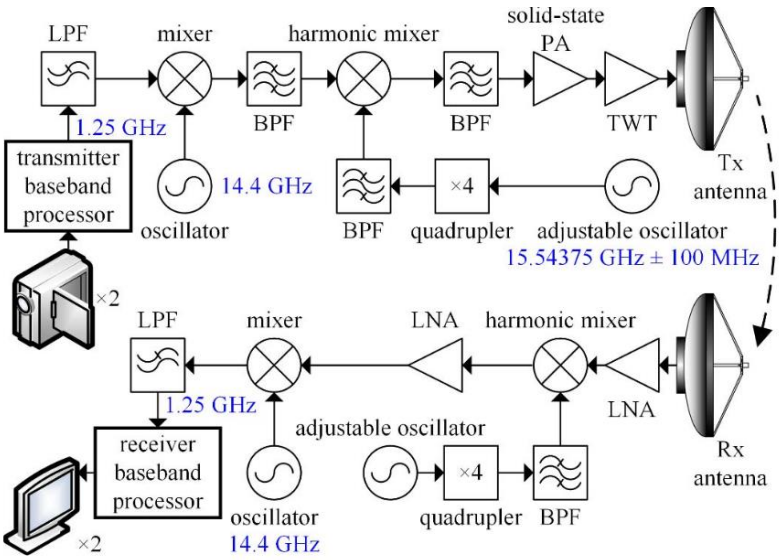


Fig. 12: Schematic of 140-GHz band communication system presented in [62].

In that work, *Hirata et al* developed two technologies for the generation of wireless signals in 120 GHz band: **UTC-PD** and **InP HEMT MMIC**. In one of the approaches (Fig. 13), a single-mode laser was modulated at a frequency of 62.5 GHz with an optical intensity modulator and fed into a planar lightwave circuit containing an arrayed waveguide grating (AWG) with a channel spacing of 60 GHz. Two output channels with an interval of 120 GHz were chosen and later amplified with an erbium-doped fibre amplifier (EDFA). The optical signal was then modulated by data signal and once again amplified by a second EDFA. Next, the modulated optical signal was irradiated into an UTC-PD in order to O/E-convert the signal. Finally, the signal was amplified up to 10 dBm by an InP HEMT MMIC amplifier and transmitted from a high-gain, Cassegrain antenna.

In the second approach (Fig. 14), the optical data signals are O/E converted previously to the modulation of a CW 125 GHz signal obtained by frequency multiplication (x8) from a 15.625-GHz tone. Finally, two power amplifiers, previous to the antenna, increased the output power up to 16 dBm. As for the receiver, it was based on a MMIC chipset [63] in both cases.

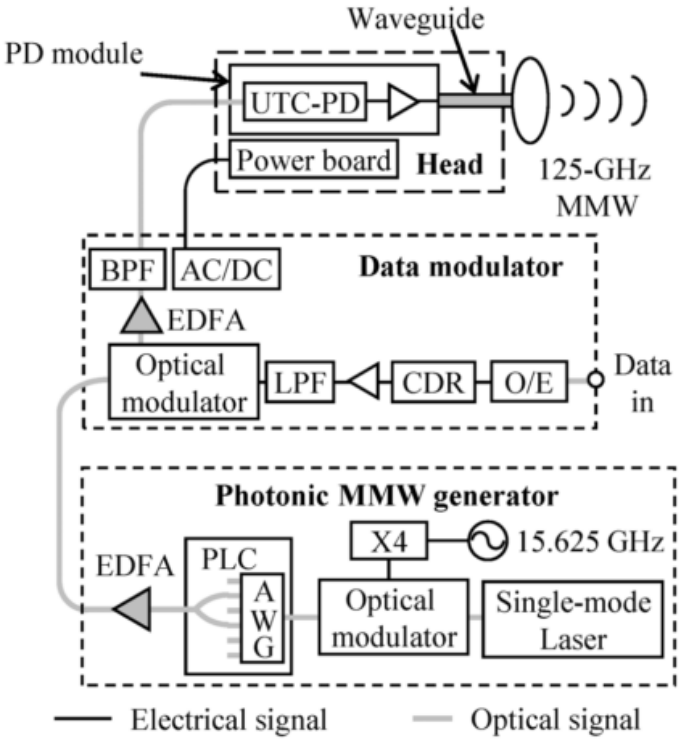


Fig. 13: Schematic of 120-GHz band transmitter using a UTC-PD [10]

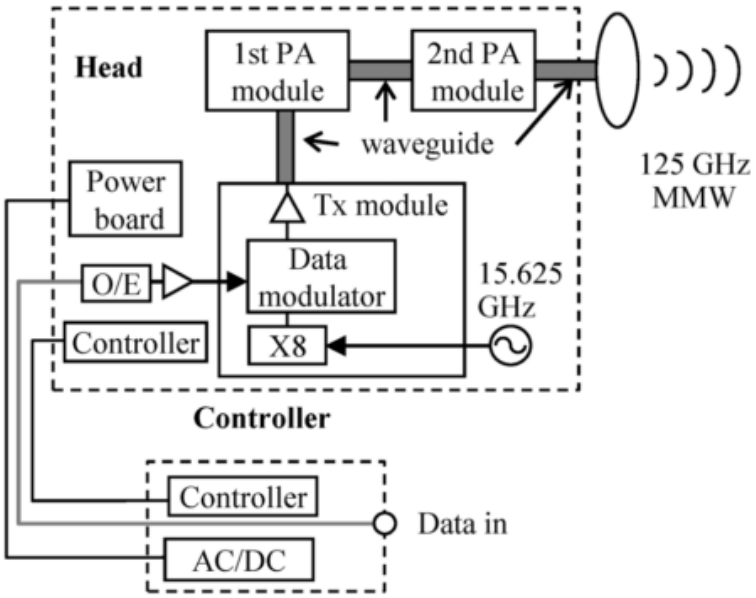


Fig. 14: Schematic of 120-GHz band transmitter using HEMT MMICs [10]

The work of *Hirata* compared both solutions, highlighting the main advantages of each approach. Regarding the **optoelectronic solution**, the head of the transmitter (the module which effectively adequate the signal before transmitting it) is smaller, since it only includes the O/E conversion and

electrical amplification. In addition, one could change the modulation scheme in the controller without having to change the head. The controller block is, however, significantly heavier than the **HEMT MMIC solution**, as the first approach includes all the equipment involved in signal generation and modulation, while the last one includes these functionalities in the head of the transmitter, instead of the controller. Nevertheless, the most important advantage of the optoelectronic technology is that the radio **signal generator could be shared** by several radio transmitters, being able to allow even multi-band wireless systems by using wavelength division multiplexing (WDM) techniques. This results in a fundamental advantage in order to reduce the overall cost per wireless link. On the other hand, the electronic solution stands out for its small and simple structure, low cost and consumption. However, it does not offer the possibility to change the modulation scheme and/or operation frequency, reason why it does not seem suitable for the next generation of mobile wireless communications. Nevertheless, the authors claim that this technology could be suitable for live TV relay and temporary wireless links, such as large-scale events or disaster recovery.

## 3.5 Conclusions

As aforementioned, three key enabling technologies are considered within the TERALINKS Project: photonic-based THz sources, Traveling Wave Tubes (TWTs) and Smart Antennas. In this chapter, a brief review of the available techniques for terahertz generation have been presented. The basic concepts behind the uni-travelling-carrier photodiodes and travelling wave tubes were explained and their state of the art presented. The explanation and design of antennas will be left for the complementary work that accompanies this Master Thesis.

After presenting the different techniques for THz generation and the different approaches up to date to developing communication links at these frequencies, it seems more feasible to adopt a solution similar to the optoelectronic approach in [10]. UTC-PD photonic solution provides broadband, significant output power. Moreover, this solution takes advantage of the 1550nm optic solutions, commercially available and widely deployed. The optical signals to be mixed could be transported to the head transmitter from long distances without significant losses. This would allow reducing the overall cost per link in a mature scenario with several stations deployed across a territory, being the signals broadcasted from a head centre, where all the optical equipment could be hosted, and transported by fibre cables.

# 4. THz Packaging Techniques

Photonic techniques for THz generation enable the integration of wired optic and wireless communication networks, regardless of the modulation scheme or data rates. In order to obtain THz, a photoconductive antenna is typically used to transform the electric currents generated by the photomixer into electromagnetic waves. One of the main materials for monolithic integration of the photonic components in integrated circuits is Indium Phosphide , since it has a direct band gap and thus generates light efficiently [64]. However, it has a high dielectric constant (around 12.4) and this deteriorates the radiation efficiency of the antenna, as well as its directivity, because waves tend more to propagate along the substrate the higher the dielectric constant is.

Traditionally, a solution to this issue consists on a quasi-optical approach, employing Silicon or other dielectric material lenses in order to collimate the radiation of the photoconductive antenna. This lenses can be designed with gradient index in order to optimise the collimation of the beam [65]. These lenses are typically made of the so-called *float-zone single crystal silicon*, which is one of the most transparent dielectric materials at the THz region [66]. It offers a quasi-constant index of refraction across this band and thus incurs in small dispersion, which make it useful for broadband, TDS applications. The performance of these lenses can be increased by applying antireflection coatings or designing antireflection structures, such as in [67], where an antireflection structure silicon lens that increases the amplitude of a time-domain pulse up to 10%, increasing some the spectral amplitude of some frequencies up to 50%.

Another trend is to couple this radiation to the corresponding WR waveguide, so that the energy will rearrange as the fundamental mode of the waveguide. Both approaches are schematically illustrated in Fig. 15. Some examples of each can be found in [68] and [69], respectively. The first introduces a hyper-hemispherical Silicon lens and presents an equivalent circuit model of the photomixer together with the lens. The second article presents a transition from coplanar to a WR12 rectangular waveguide with an insertion loss of 3 dB. Another example of waveguide coupling is found in [70], where coupling to a WR-10 standard waveguide is achieved. The output power is measured within the whole band, obtaining a peak power at 100 GHz of about -10 dBm.

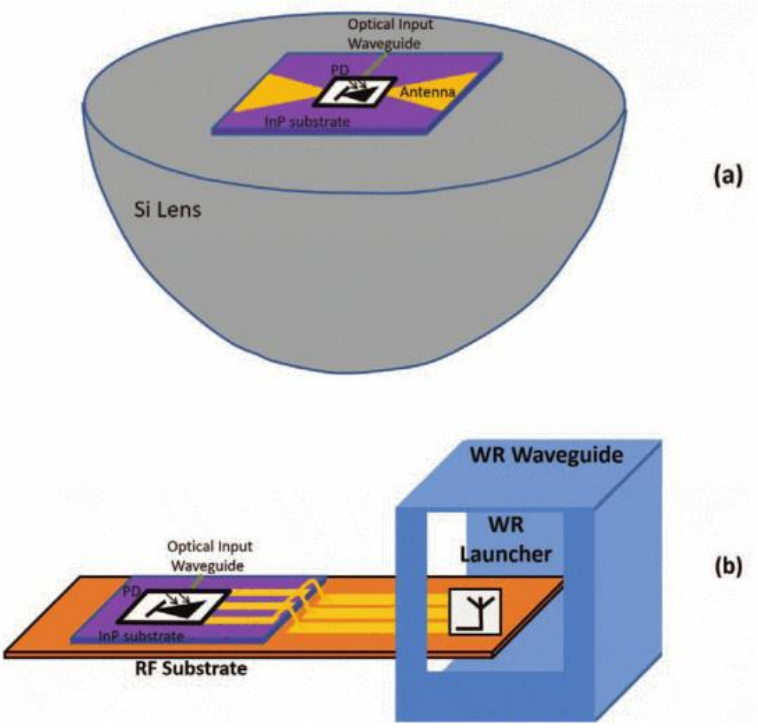


Fig. 15: Schematic representation of a) silicon/dielectric lenses for collimation and b) coupling the radiated energy into a waveguide [64].

As it has been seen, integration and packaging of these components is a challenging task. Two main techniques have been traditionally adopted for this purpose: the use of silicon lens and coupling the radiation to a waveguide. The next chapters will focus on the proposal and design of a new integration technique based on an ellipsoidal reflector.

## 5. Fundamental theory of the ellipse

An ellipse can be defined geometrically as a locus of points (namely, set of points) such that for any point P of the set, the sum of the distances |F1P|,|F2P| to two fixed points F1, F2 (the foci) is constant and equal to the major axis. The midpoint of the line segment joining the foci is called the centre of the ellipse, C. The line through the foci is called the major axis, 2*a, and the line perpendicular to it through the centre is called the minor axis, 2*b, being 'a' and 'b' the lengths of the major and minor semi-axis, respectively. The distance from the centre to each of the foci is called the focal distance, fd. The ellipse is defined by the following equation and an example can be found in Fig. 16:

$$\frac{x^2}{a^2}+\frac{y^2}{b^2}=1 \qquad \text{Eq. 13}$$

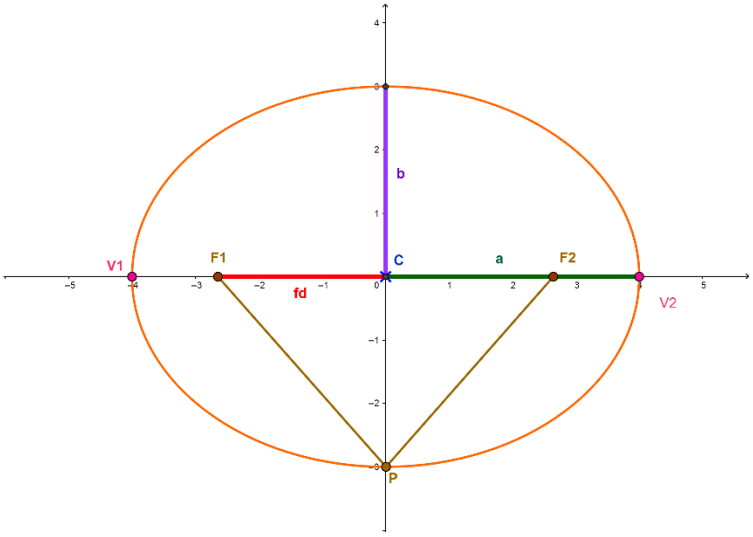


Fig. 16: Elements of an ellipse.

Additionally, the focal distance can be easily determined by Pythagoras theorem. Given that the distance from a point P to both foci equals 2*a, which is the length of the mayor axis, if P corresponds to a point located on a vertex of the minor axis, an isosceles triangle $\widehat{F1PF2}$ is formed. Given that the distance $\overline{PF1}$ equals $\overline{PF2}$, a rectangular triangle $\widehat{PCF2}$ can be extracted where 'a 'is the hypotenuse of the triangle. The geometric representation is given in Fig. 17. Finally, value of the focal distance can be computed:

$$fd = \sqrt{a^2 - b^2} \qquad \text{Eq. 14}$$

The eccentricity parameter, e, defined as the ratio between the focal distance and the major semi-axis, $e = fd/a$, unequivocally identifies the type of conic section and could be thought of as how much a conic section deviates from being circular. In the particular case of an ellipse, this parameter ranges from $0 < e < 1$ ($e$=0 corresponds to a circle and $e$=1 corresponds to a parabola, while $e$>1 would correspond to a hyperbola).

When applying a revolution symmetry to an ellipse, an ellipsoid is obtained. Considering a change of the coordinate axis and assuming that the major axis is oriented along the z axis (in Fig. 7 the mayor axis would correspond to the X axis), the resulting ellipsoid is described by:

$$\frac{z^2}{a^2} + \frac{x^2 + y^2}{b^2} = 1 \qquad \text{Eq. 15}$$

One interesting consequence of the total travel length being the same along any path taken between the two foci bouncing on the surface is that, if a light source is placed at one focus of an ellipsoidal reflector – this is, as previously mentioned, sweeping an elliptic curve along its major axis in order to obtain a revolution surface – **all rays** coming out from the source will be reflected by the mirror and **focalized into the second focus**. This is a fundamental property of the ellipse which could be used in order to collect in one focus, F2, all the energy radiated by any source (punctual, horn, dipole…) located at the other focus, F1, and radiating towards the reflector surface.

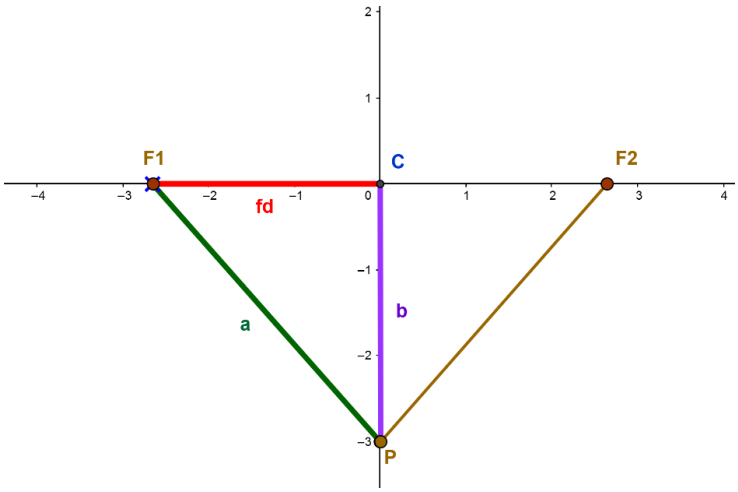


Fig. 17: Pythagoras theorem

Authors in [71] benefit from this property in order to design on-chip crossings and 90 ° turns in photonic integrated circuits. For this purpose, a metal-free reflector is designed, in which the angle of incidence and the difference in the refractive index between the waveguide and the reflector enables total internal reflection (TIR) at the reflector' s surface without the

need of metal coating. In this work, the authors achieve to design and manufacture turning devices with reduced optical loss and crossing devices with reduced loss and crosstalk. However, it should be highlighted that the input and output points for the 90° turning device do not correspond to the location of the geometrical focal points of the ellipse. They are located at the beam waist locations (M), which are determined by physical optics and located at a distance d from the focal point F, as shown in Fig. 18.

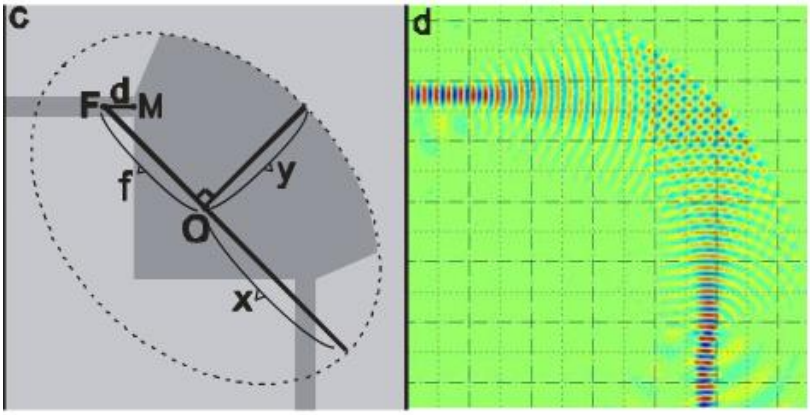


Fig. 18: Elliptical Reflector Turn geometry and EM simulation [71]

In order to check the phenomenon described by the authors, a full-wave simulation was set up in ANSYS Electronics Desktop 18 High Frequency Structure Simulator (HFSS). Here, an ellipsoidal cavity was simulated. The simulated structure is presented in Fig. 19. It consists of an ellipsoidal reflector contained in a radiation box for calculating the radiated fields and provide an air/quartz boundary. A small lumped port was placed at one of the focus of the ellipse in order to emulate a punctual source, such as an UTC-PD, and a flat, rectangular dipole was placed in order to provide an omnidirectional radiation pattern. The structure was simulated in the range from 200 to 300 GHz. The XZ plane was set as an E-Symmetry plane in order to alleviate the computational requirements of the simulation.

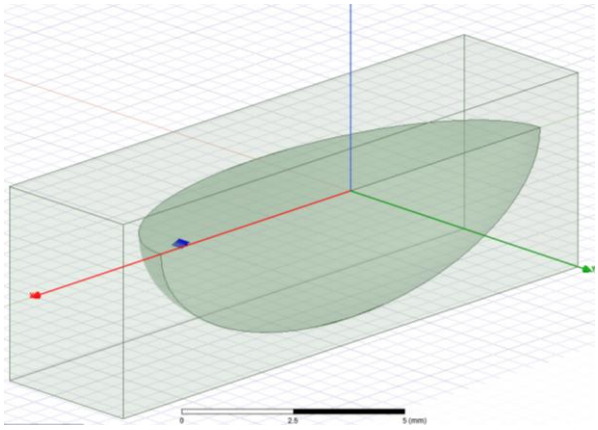

Fig. 19: Simulated ellipsoidal reflector contained in a radiation box.

The cavity was filled up with quartz glass, with dielectric constant $\varepsilon_r = 3.78$ and thus refractive index $n = \sqrt{\epsilon_r \mu_r} = \sqrt{3.78 \cdot 1} = 1.94$. Following the TIR principle, the critical angle within the boundary between quartz and air can be calculated:

$$\theta_c = \arcsin\left(\frac{n_2}{n_1}\right), n_2 \cong 1\ (air)$$
$$\theta_c = 30.95º \qquad \text{Eq. 16}$$

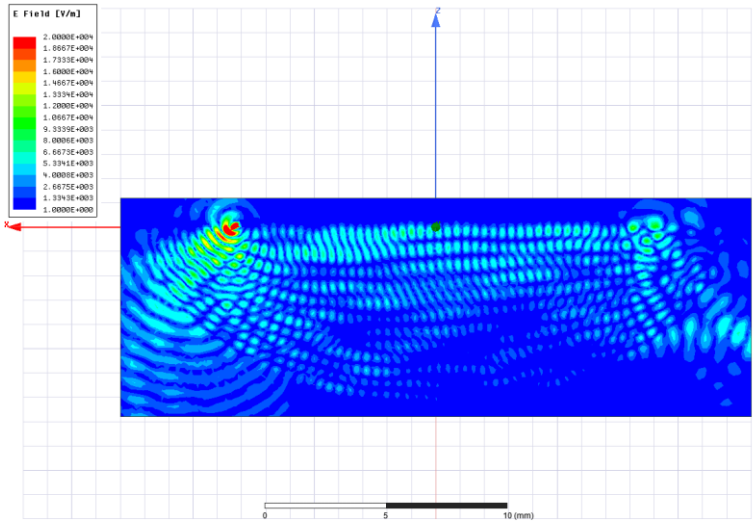


Fig. 20: Simulated electric field propagating through the quartz-filled ellipsoidal cavity

The propagated fields are shown in Fig. 20. It can be observed how the energy propagates across the cavity and part of it is gathered in the second focus. There is, however, a substantial leak of these fields in the nearest part of the reflector, due to an insufficient incidence angle. This effect could be improved by employing a dielectric with a higher refractive index. This would reduce the critical angle and therefore increase the amount of field focalized in the second focus. Nevertheless, it should be taken into account that the use of dielectric would imply a great amount of losses. Moreover, characterization of dielectric materials at these frequencies must be done beforehand and no data regarding this characterization was available before the development of this study. Therefore, this solution was discarded.

Another solution is employing a metallic surface in order to achieve the reflection. In this case, there is no essential condition for achieving TIR. A full-wave simulation of an ellipsoidal cavity in HFSS. The simulated structure is similar to the one presented in Fig. 19, defining the internal part of the reflector as vacuum, instead of quartz. The structure was simulated in the range from 200 to 300 GHz. The XZ plane was set as an E-Symmetry plane in order to alleviate the computational requirements of the simulation. The propagated fields are shown in Fig. 21. It can be observed that the energy

propagates across the cavity and is majorly gathered in the second focus. It should be taken into account that, since an omnidirectional source has been placed, part of the energy is radiated upwards, not being reflected to the second focus by the ellipsoidal mirror. For this reason, the amount of energy collected at the second focus is lower than the radiated energy. In order to improve this performance, some structure must be designed in order to prevent this energy leak.

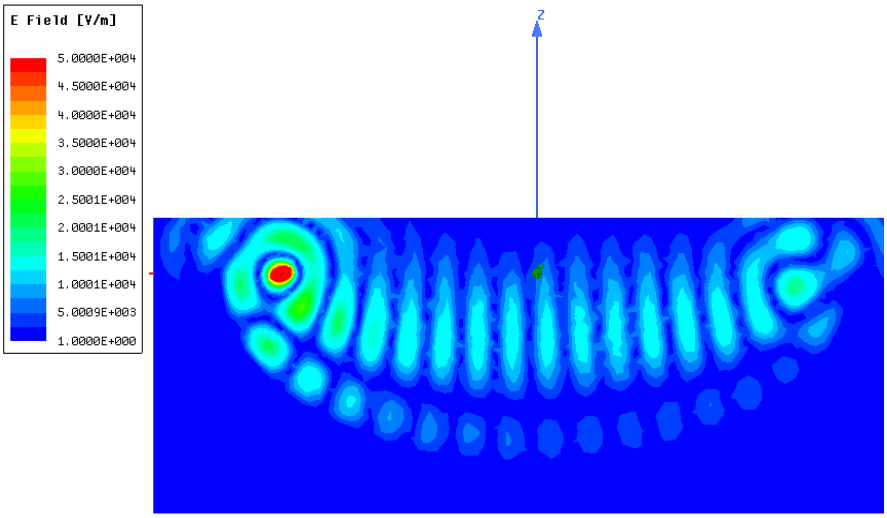


Fig. 21: Simulated electric field propagating through the ellipsoidal cavity.

Following this proof of concept, this Master Thesis will focus on the design of an integration block with an elliptical reflector. This structure is proposed for integrating and adapting a photodiode for efficiently generating power in the frequency band from 220 to 260 GHz, in order to fulfil the requirements of power generation for the TERALINKS project.

# 6. Design

In the previous Chapter, the basic properties of the ellipse have been presented and a conceptual demonstration has been proven through a simulation with HFSS. However, there are several aspects that should be taken into consideration for the design of an actual component. These include how to illuminate the photomixer, how to support the photomixer inside the ellipsoidal cavity, how to maximize the power directed to the ellipsoidal reflector or how to collect and output the generated power. In this Chapter, each of this aspects will be dealt with and the different stages of design will be explained. First, the dimensions of the elliptical reflector will be discussed. Then, each of the focus and the components to be placed at both of them will be analysed. Finally, an assembly of every part will be presented and conclusions will be drawn.

## 6.1 Ellipsoidal reflective cavity

As has been demonstrated in the previous Chapter, it could be feasible to employ an elliptical reflector to collect at its second focus a significant amount of the energy radiated from the first focus. In principle, the dimensions of this reflector should not be a restricting factor if the waves were perfectly spherical. This means, if far-field condition would be achieved. However, this condition might not be achieved if the dimensions are too small. On the other hand, current packaging alternatives for THz sources are not essentially bulky and thus the proposed, novel technique should not be significantly bulky. For this reason, a trade-off must be solved with regard to these dimensions. These are, essentially, the length of the mayor axis and the eccentricity of the ellipse. These two parameters govern the geometry of the ellipse and are the ones that must be determined in order to assure the propagation of spherical waves. Moreover, the ellipsoidal reflector does not recover the phase front properly and incurs in a phase error [72] and the consequent distortion. It is believed that a shaping of the surface could be introduced in order to compensate this distortion. However, due to time-constraints this could not be performed.

It would have been desirable to develop a study concerning this trade-off in order to offer an optimised solution. However, due to time constraints this was not possible, and a semi-mayor axis of 20 mm and a ratio between the mayor and minor axis of 0.5 (thus, a minor axis of 10 mm) were chosen. Fig. 21, in the previous chapter, presents the magnitude of the electric field propagating across an ellipsoidal cavity with the aforementioned dimensions and shows how the energy actually propagates and gathers around the second focus. For this reason, it is believed that the generation of quasi-spherical waves was achieved. A study concerning the optimal dimensions of the

ellipsoid, as well as a possible shaping of the surface, are left as some of the future lines of work of this Master Thesis.

## 6.2 Focus 1: Bridge and photogeneration

As stated before, a metallic bridge was chosen in order to satisfy the need of successfully integrating and supporting the photomixer. It consists of a several-mm-thick layer of metal that supports a 150 μm-thick substrate of quartz. A horn-shaped via was designed to be etched in the layer of metal. This horn was meant to increase the amount of power to be delivered downwards, since the bridge is meant to be placed on top of the reflective surface. Therefore, maximizing the power in this direction will be one of the fundamental design goals. On the substrate, an antenna will be designed in order to couple and radiate the THz signal generated by the photomixer, following the idea of a photoconductive antenna. This antenna will also be used to provide DC bias for the UTC-PD photomixer. With this configuration, simulation results provided a significant amount of power being radiated downwards, into the ellipsoidal cavity. Different approaches, which will be presented in the current section, have been studied in order to maximize the directivity in this direction.

### 6.2.1 UTC-PD Photomixer

The design of the UTC-PD photomixer was not concerned in this work, since it will be delivered by the team from IEMN in Lille, France. The **lack of information** regarding this device has fundamentally conditioned this work, since it is the key component of the proposed system and therefore some assumptions have been made in order to have some dimension parameters as a starting point for the design. This way, it has been assumed that the delivered photomixer will be integrated in a small block that shall be connected to the DC bias of our system. It was modelled as silicon block with dimensions 50μm x 100μm x 50μm, although some other materials are traditionally used in the literature. This block aims to model a possible absorption of loss of power due to the presence of a substrate on top of the antenna. In order to model the actual source of power, a lumped port was used. As it has been reported in the literature, photoconductive mixers usually have several kΩ of input impedance. As for UTC-PD, a wide range of impedances are usually given, ranging from a few Ohms, such as the (18 - j57) Ω presented in [73], to several kΩ as well. In this case, the maxima of power is achieved by complex-conjugate matching. However, due to the unavailability of this parameter, it was decided to design a standard model and thus an input **port impedance of 50Ω** was assumed. Moreover, it is unknown whether the photomixer block will include some kind of impedance

matching network. This model would contribute to draw a series of conclusions which could be applied in a more specific, future model with more information regarding the photomixer.

### 6.2.2 Design of the photoconductive antenna

The design of the photoconductive antenna was studied in the first place. When selecting the **type of antenna**, a plethora of alternatives arise. One could chose a broadband antenna, such as a bow-tie or log-periodic antenna, or a resonant antenna, such as a dipole. The main advantage of the last type is that it provides a higher output power than the broadband, due to the resonant condition. On the other hand, their bandwidth is reduced in comparison with broadband designs. Nevertheless, requiring a 40 GHz bandwidth at centre frequency of 240 GHz implies only a 16.6% fractional bandwidth. Traditionally, the literature refers to a "broadband antenna" when the ratio between the highest and lowest frequencies is higher than an octave. This is $f_h/f_l=2$. In this case:

$$\frac{f_h}{f_l} = \frac{260}{220} = 1.18$$

Given this result, the bandwidth required for our antenna could be considered relatively narrow and it was believed to be achievable with a resonant antenna. Moreover, it was desired to maximize the output THz power. Therefore, a resonant design was chosen at first instance. Nevertheless, as will be discussed later in this section, some considerations will be made with regards to this resonant condition, since there will be a **trade-off** to be solved between the resonance and the bandwidth of operation. Different antennas have been simulated and conclusions will be drawn at the end of this section. Before presenting these models, some general assumptions and considerations are presented next.

As for the substrate, a transparent material must be chosen, since optical radiation is to propagate through it. Moreover, material with a relatively low permittivity shall be chosen, in order to minimise loss. For this reason, quartz was selected. It is a transparent material and its dielectric constant is around 3.78 (although dielectric characterization at sub-THz frequencies still needs further study). The **thickness of the substrate** was determined by dealing with a compromise between availability/feasibility of a layer with that thickness and the fact that a higher thickness of substrate would incur in higher loss, while incurring in more energy propagating through it (which would be beneficial, since radiation in that direction is aimed). For this reason, a thickness of 150 μm was chosen. It is important to note that including a substrate changes the effective wavelength of propagation. Since the dielectric constant is higher on the substrate, the effective wavelength is

reduced. This implies that, for example, a half-wave dipole designed for resonance at one specific frequency would be effectively bigger when adding the substrate and thus its resonance would be shifted to smaller frequencies. The designed antennas hereby presented have been designed taken this into consideration.

On the other hand, the thickness of the metallic paths and patches was also determined. When determining these parameters, fabrication limitations as well as skin-depth effect had to be taken into account. The **skin-depth** effect is a phenomenon that consists of the current density being higher in the surface of a conductor material where an alternate current (AC) is travelling. This makes the effective AC resistance higher than the one for DC operation as well as frequency dependant. It is defined as the depth in which the current density has decreased in a 1/e factor. Considering copper as the conductive material, the value of this parameter is 0.133µm at the frequency of work. It is often recommended to use a metal thickness at least 10 times bigger than the value of skin-depth. For this reason, 1.5µm was chosen. Once this considerations have been highlighted, the different designs of the photoconductive antenna are presented next.

#### 6.2.2.1. Resonant dipole

The design of the dipole antenna consists of 2 thin patches or stripes, fed at one of their ends by the lumped port that models the photodiode. Both stripes are equal and their dimensions have been optimised to achieve a resonant operation at 240 GHz. As a first approach, a thin dipole was designed through an optimization process. This process resulted in a dipole formed by 2 metal stripes of dimensions 170µm x 30µm, represented in Fig. 22 and whose S11 parameter is shown in Fig. 23. The green box represents the photodiode integrated block. The dipole has been designed together with the quartz substrate, in order to take into account its effects on the overall performance. As for adaptation, it can be observed that the band of interest maintains a return loss below 11.8 dB. Moreover, a very good impedance match is achieved at centre frequency (Fig. 24).

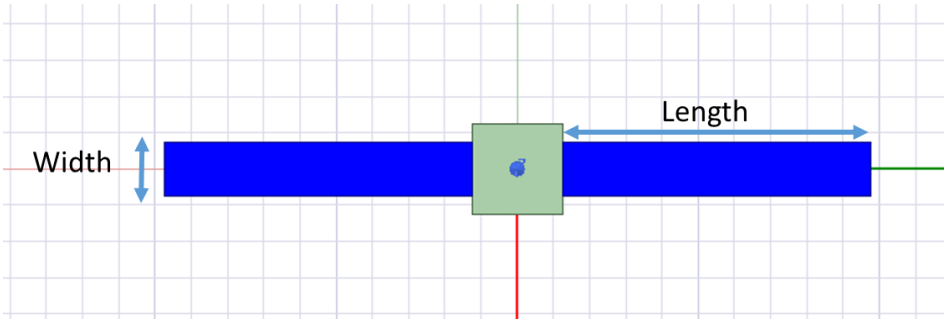


Fig. 22. Layout of the microstrip "thin" dipole for THz generation.

The effect of the substrate is constatable when comparing the radiation patterns of the dipole with and without substrate (Fig. 27). In the case of a dipole without substrate, an omnidirectional pattern is obtained. However, when adding the substrate, this omnidirectional feature vanishes and greater side lobes appear. As a consequence, as shown in Fig. 25, the maximum directivity is given pararell to the substrate, at $\theta$=90°, with a 2.9 dBi directivity at boresight.

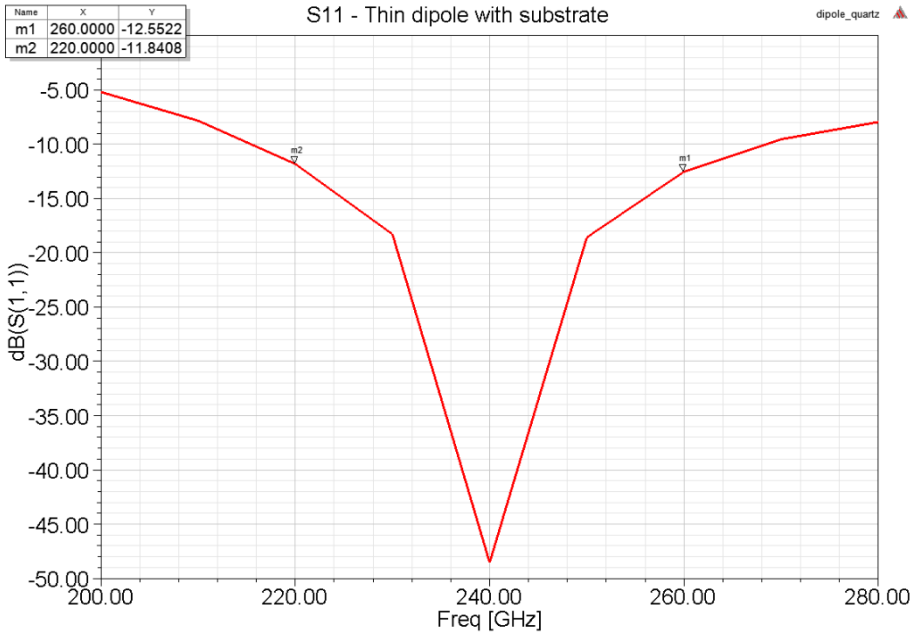


Fig. 23. Adaptation (S11) of the microstrip "thin" dipole for THz generation with Zo=50Ω.

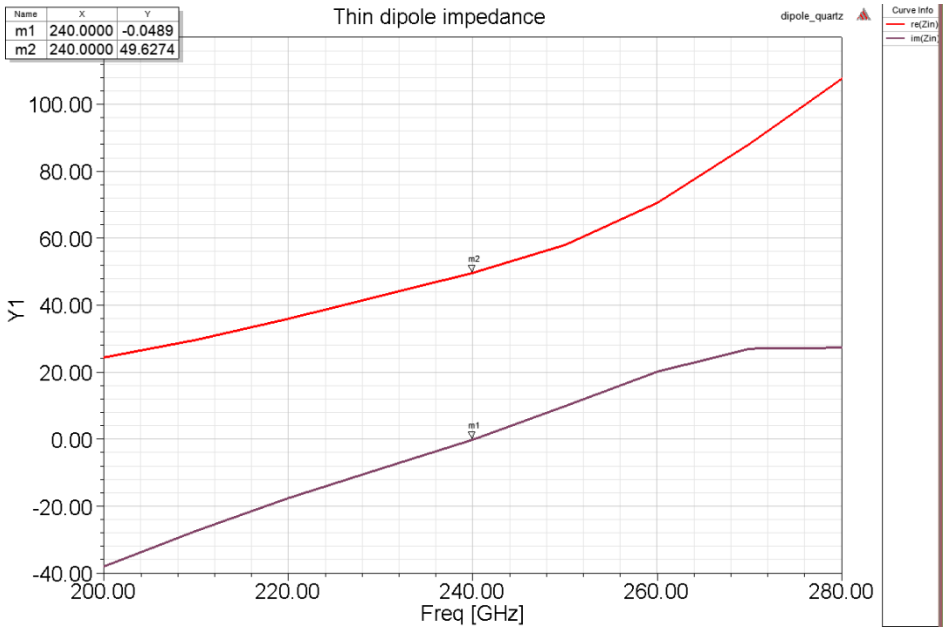


Fig. 24: Adaptation (Zin) of the microstrip "thin" dipole for THz generation with Zo=50Ω.

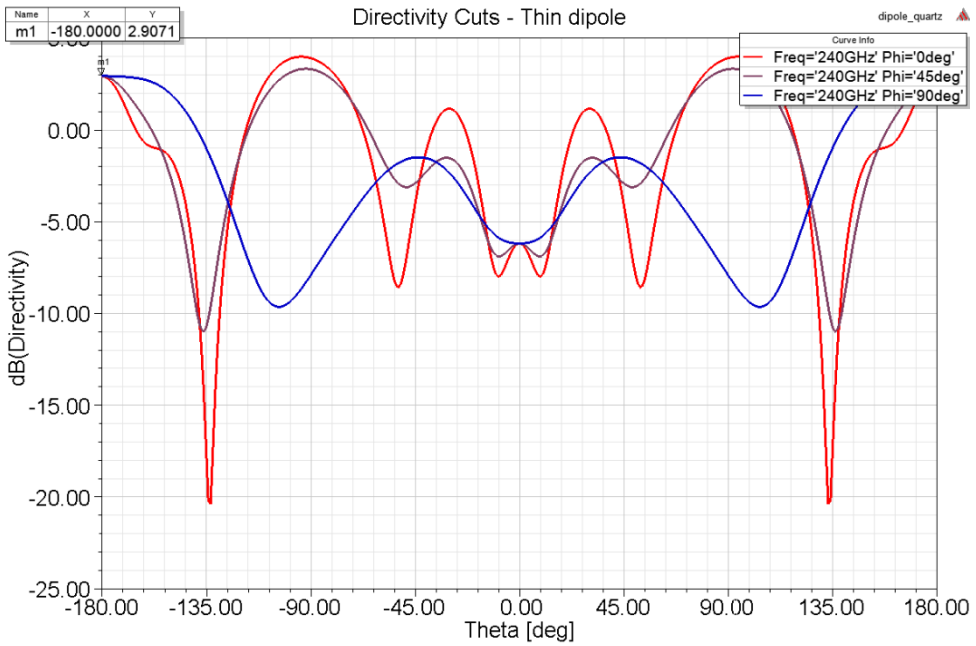


Fig. 25. Directivity of the microstrip "thin" dipole for THz generation at 240 GHz.

However, this directivity is not constant and a difference of 3.5 dB is found between the lowest and highest frequencies of the band of interest (220 and 260 GHz, respectively). This is not desirable for a broadband application such as the one aimed by TERALINKS and this difference should be minimised.

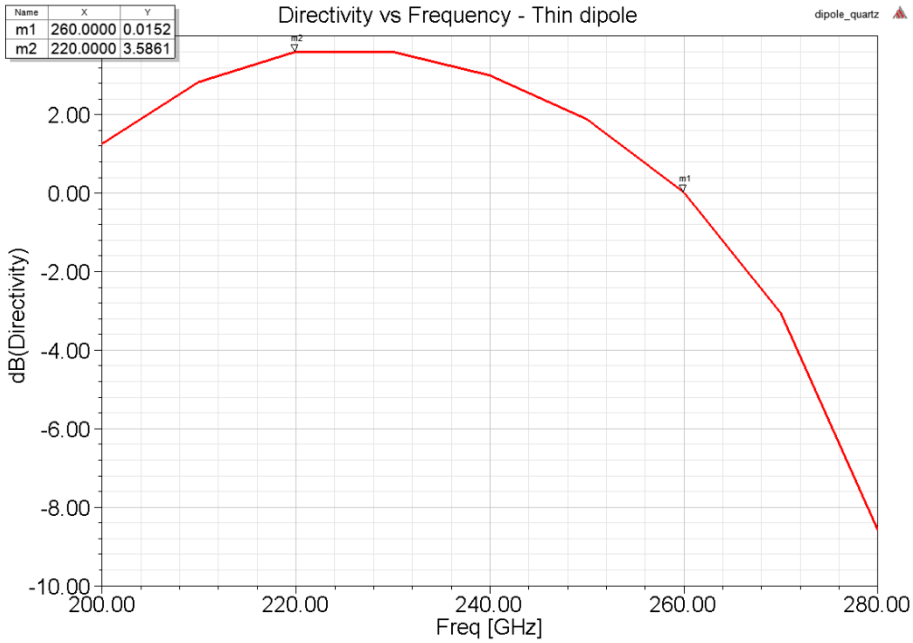


Fig. 26. Directivity at boresight of the thin rectangular dipole.

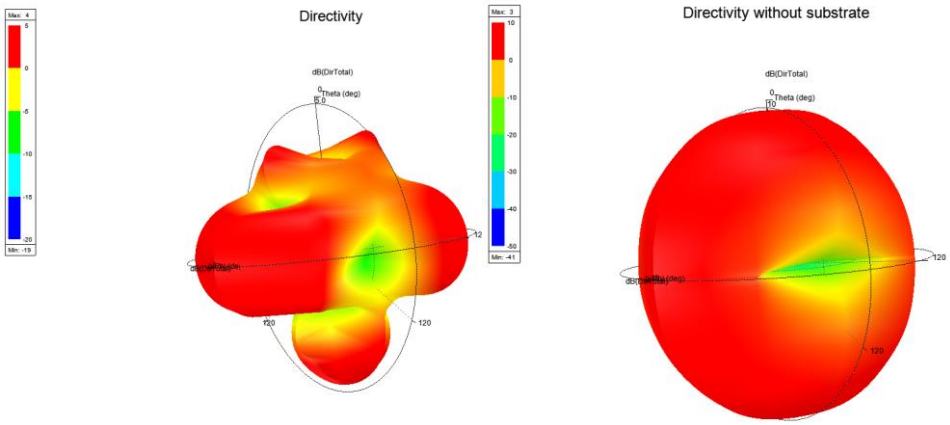


Fig. 27. Comparison of radiation patterns a) with and b) without substrate of the microstrip dipole at 240 GHz.

#### 6.2.2.2. Broadband dipole

In order to study the trade-off between bandwidth and resonance, a wider approach of the dipole was explored. It is generally known that maintaining the same length of a dipole, it can be made more broadband by widen it. However, increasing its width also reduces the frequency of resonance. All in all, after a second, more restricted optimization analysis (the total length was restricted to values more similar to the corresponding to a half-wave dipole), the final dimensions of each patch of the dipole were 350µm x 250µm. Some inserts have been included in order to optimise the feeding point in the patches, assuming that the impedance match is achieved at 50Ω. The dipole has been designed together with the quartz substrate, in order to take into account its effects on the overall performance.

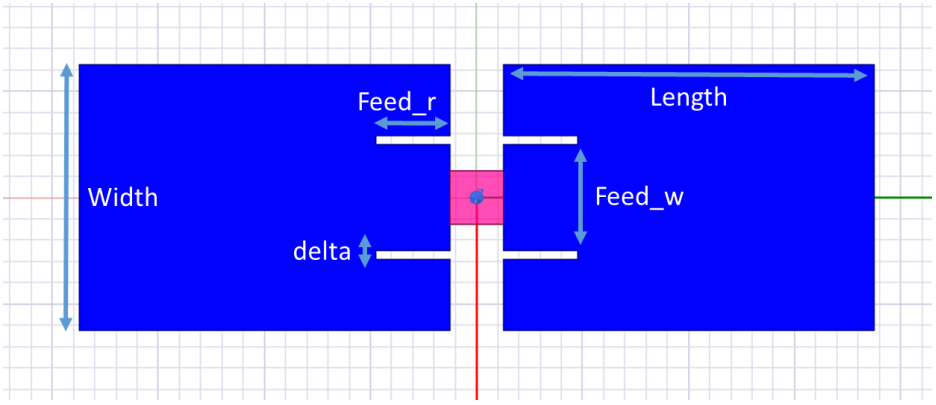


Fig. 28. Layout of the microstrip "wide" dipole for THz generation.

The total length is 750µm (taking into account the 50µm of the lumped port), which is near half of the wavelength at 240 GHz in free space. The boundary between the air and the quartz substrate modifies the effective wavelength of the system and thus the resulting antenna could be approximated to a half-wave dipole. The geometry of the dipole can be observed in Fig. 28. It provides a directivity of almost 5dBi in the direction of interest, as can be seen in Fig. 29. It can also be observed that there is a strong propagation of waves across the substrate. This will be taken into consideration for the next stages of design and alternatives will be proposed in order to reduce the propagation of surface waves. Fig. 30 represents the directivity at boresight for the whole band. It can be seen that the difference between the lowest and highest frequencies of interest is less than 1.5 dB. Finally, Fig. 31 represents the adaptation of the antenna in terms of S11. Here, it can be observed that the return loss is at least 17dB in the band of interest, corresponding to a VSWR of 1.32:1.

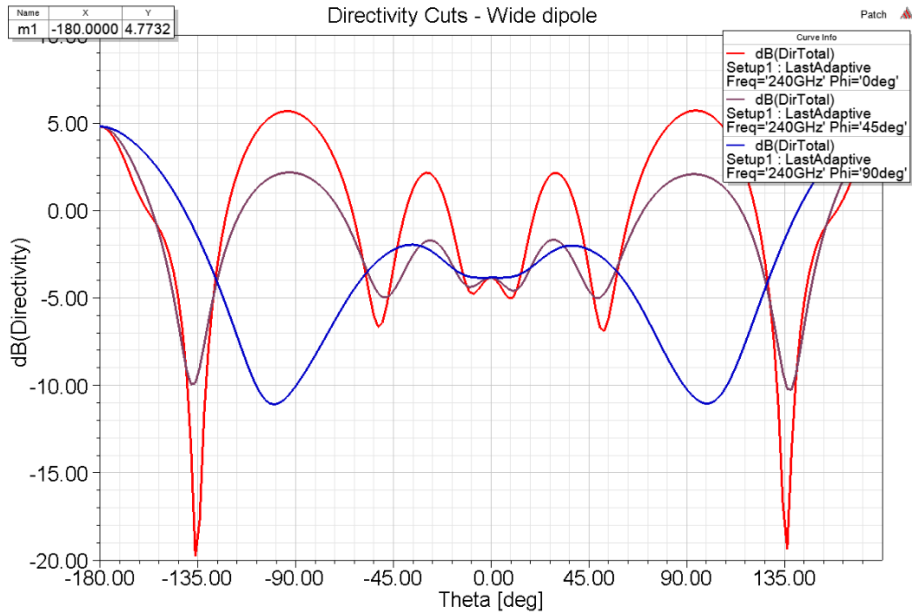


Fig. 29. Directivity of the microstrip "wide" dipole for THz generation at 240 GHz.

In comparison to the thin dipole, it can be observed that the resonance at 240 GHz is not as strong. However, the bandwidth of operation is broader and the adaptation is more uniform over the whole band. In addition, significant, although not complete, impedance match has been achieved (Fig. 32), due to the inclusion of some insets at the feeding point, as shown in Fig. 28. This inserts are placed at 50 µm of the longitudinal axis of the dipole (feed_w/2), have a width of 16 µm (delta) and a length of 70 µm (feed_r).

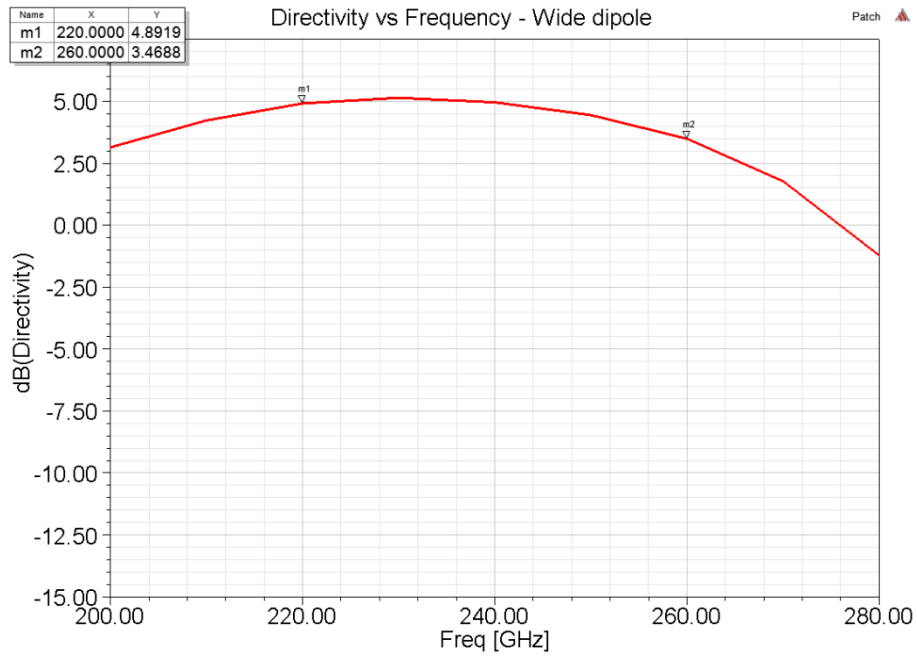


Fig. 30. Directivity at boresight of the wide rectangular dipole.

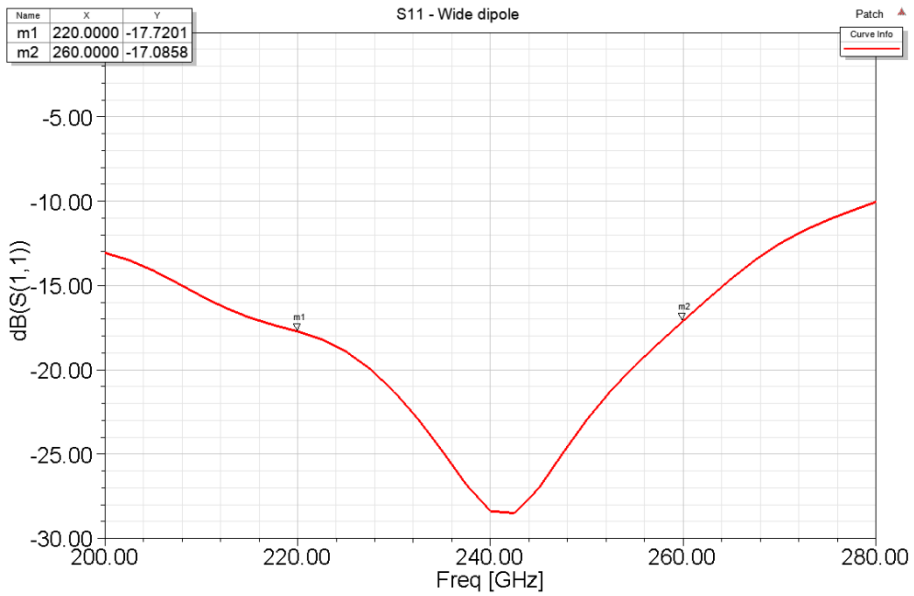


Fig. 31. Adaptation (S11) of the microstrip "wide" dipole for THz generation with Zo=50Ω.

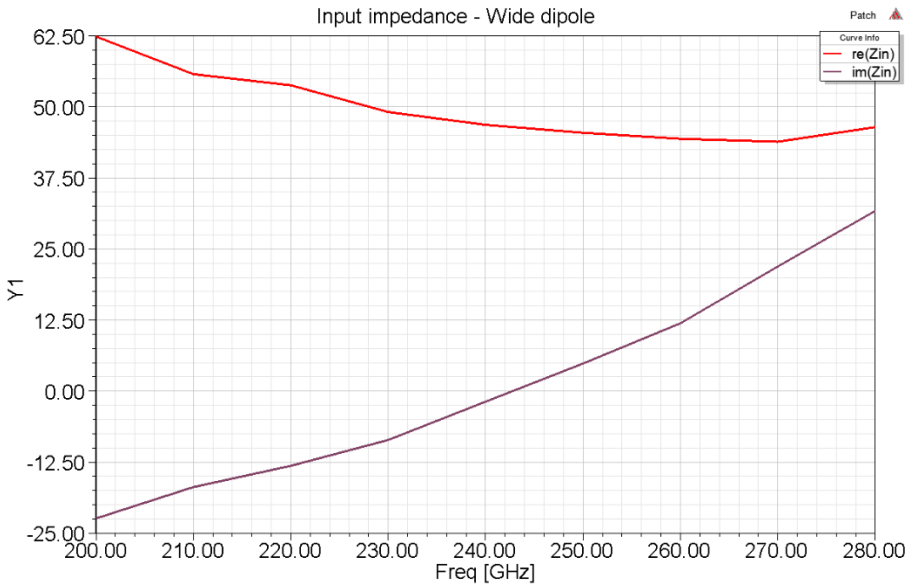


Fig. 32. Adaptation (Zin) of the microstrip "wide" dipole for THz generation with Zo=50Ω.

#### 6.2.2.3. Bow-tie antenna

Bow-tie antennas are well-known as UWB antennas [74]–[76] and thus could be suitable for our application. A bow-tie antenna was designed and simulated with HFSS to be matched at 240 GHz. It consists of two isosceles-triangle-shaped patches. It has been designed to achieve impedance matching of an input port with 50Ω impedance. To the design it, 3 dimensions have to be taken into consideration: the base and height of the triangles (alternatively, the base and the common angle of the isosceles triangle) and the offset from the centre, at which the triangles are truncated (resulting in a trapezoidal-shaped patch).

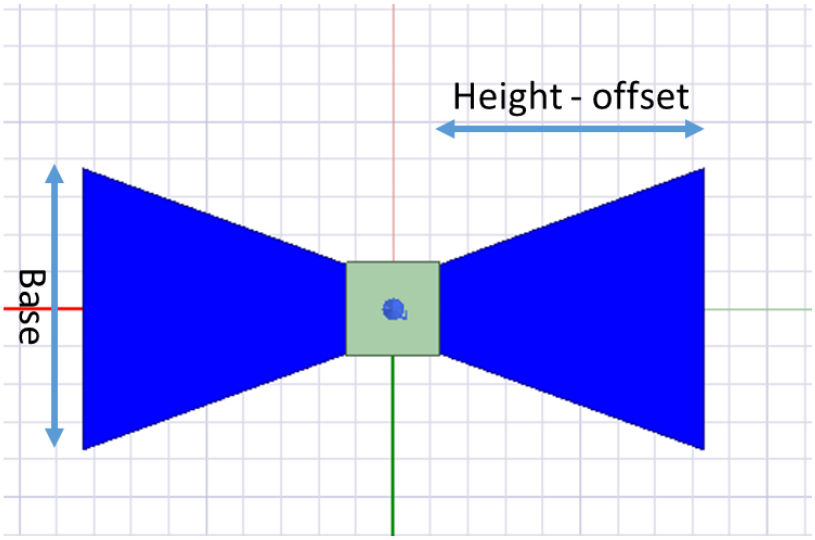


Fig. 33. Layout of the bow-tie antenna.

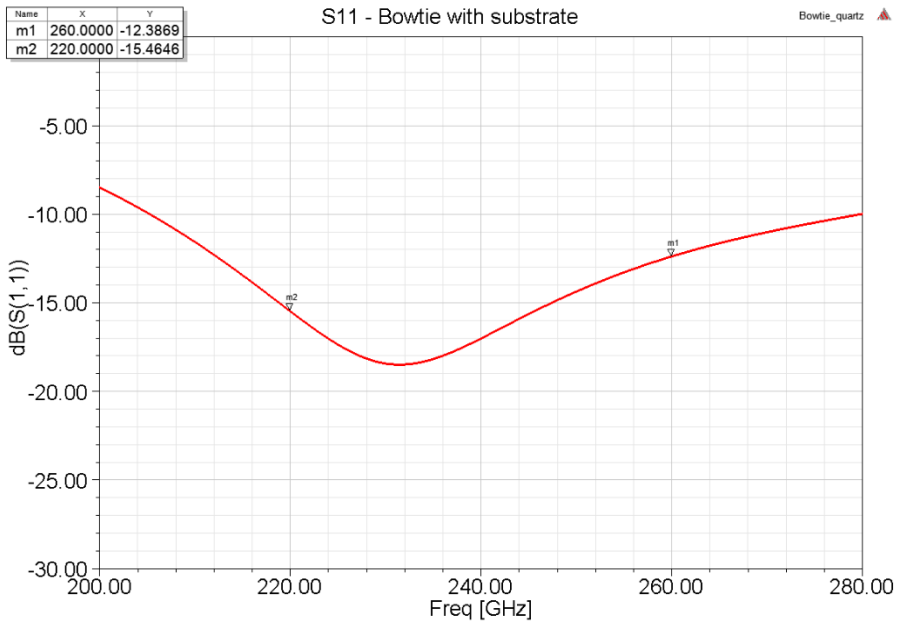


Fig. 34. S11 of the bow-tie antenna.

As it can be seen in the corresponding graphs, the adaptation is not as good as in the broadband rectangular dipole (Fig. 34). The directivity at boresight is scarcely 3 dBi (Fig. 35) and a difference of directivity of 2.5 dB is found between the limits of the band (Fig. 36).

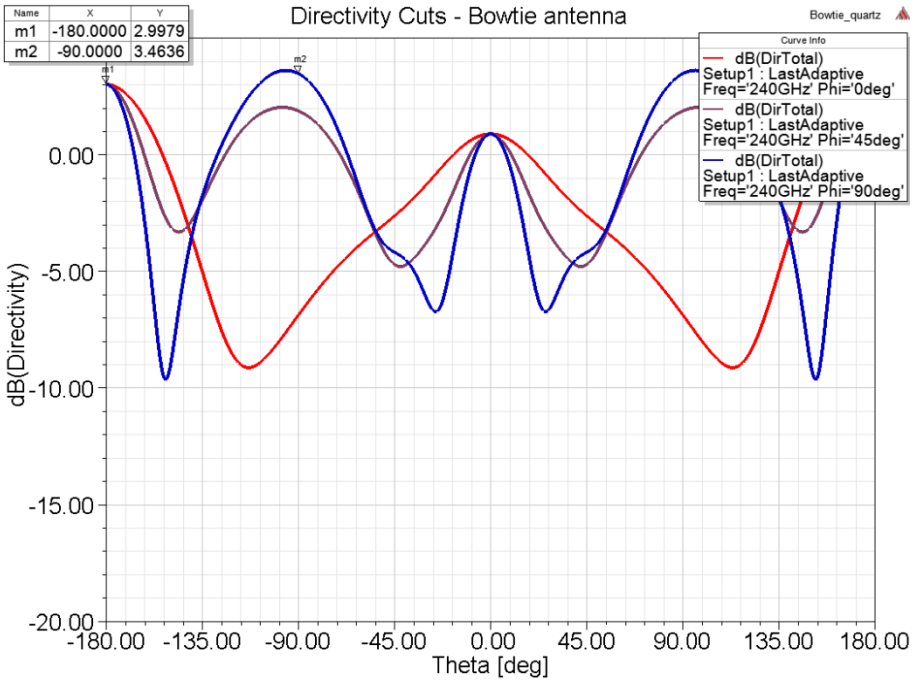


Fig. 35. Directivity of the bow-tie antenna for THz generation at 240 GHz.

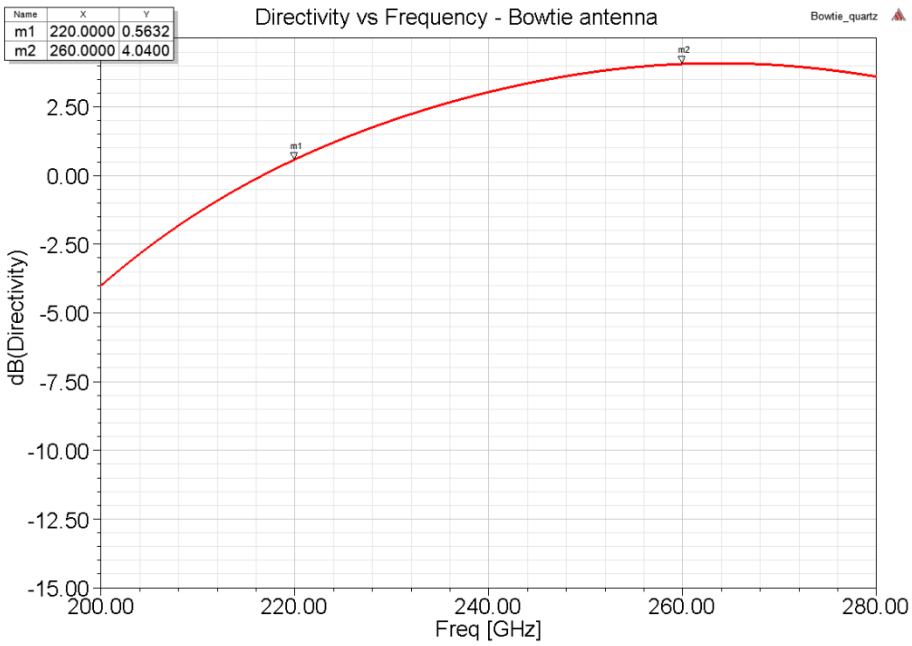


Fig. 36. Directivity at boresight of the bow-tie antenna.

#### 6.2.2.4. Diamond dipole antenna

After some literature research, diamond dipoles were found to be an interesting antenna which combine an UWB response with a matched input impedance [77]. A diamond dipole was designed and simulated with HFSS to be matched at 240 GHz. It consists of two isosceles-triangle-shaped patches, as in a bow-tie antenna, but inverted with respect to it. The two dimensions to control their design are the height and the base of the triangles. Fig. 38 shows the adaptation of the diamond dipole for an input port impedance of 50Ω in terms of S11. As for the radiation pattern, shown in Fig. 39, it can be observed how the energy tends to propagate across the substrate. A maximum directivity of 3.5 dBi is found at boresight (180°). Finally, it can be observed in Fig. 40 that this directivity is not constant in the band of interest, with a difference of 3 dB between the lowest and the highest frequencies.

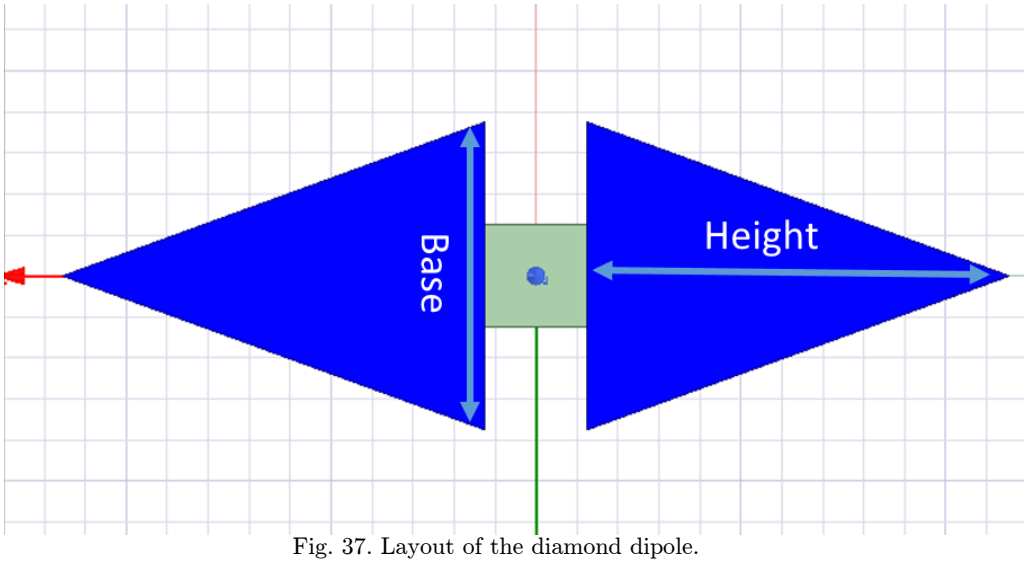


Fig. 37. Layout of the diamond dipole.

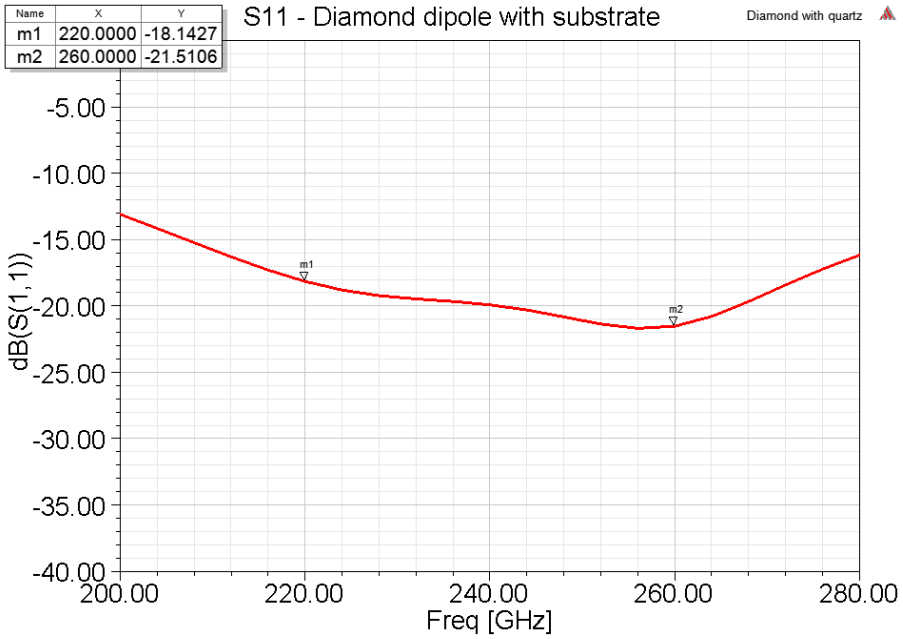


Fig. 38. S11 of the diamond dipole.

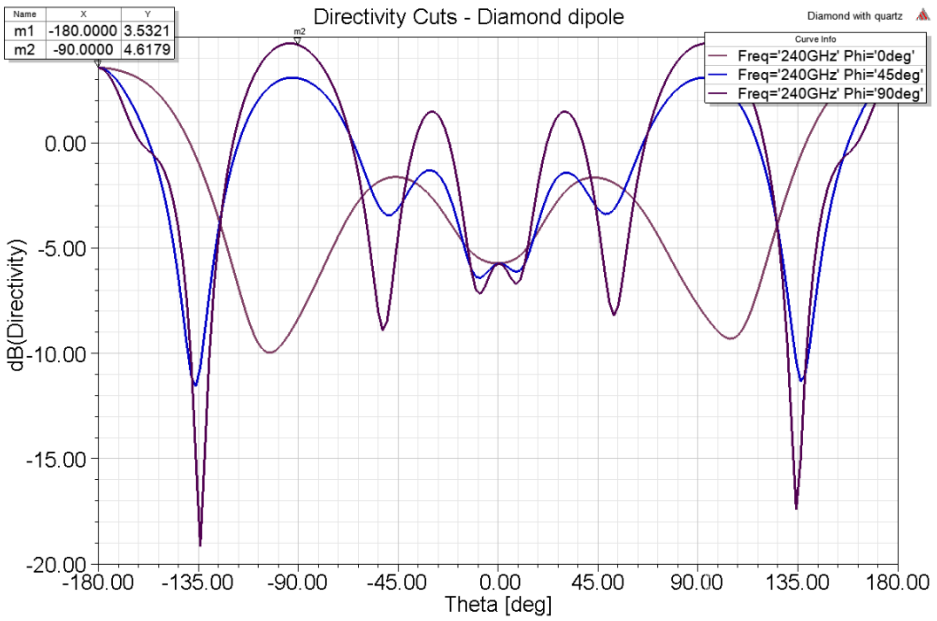


Fig. 39. Directivity of the diamond dipole for THz generation at 240 GHz.

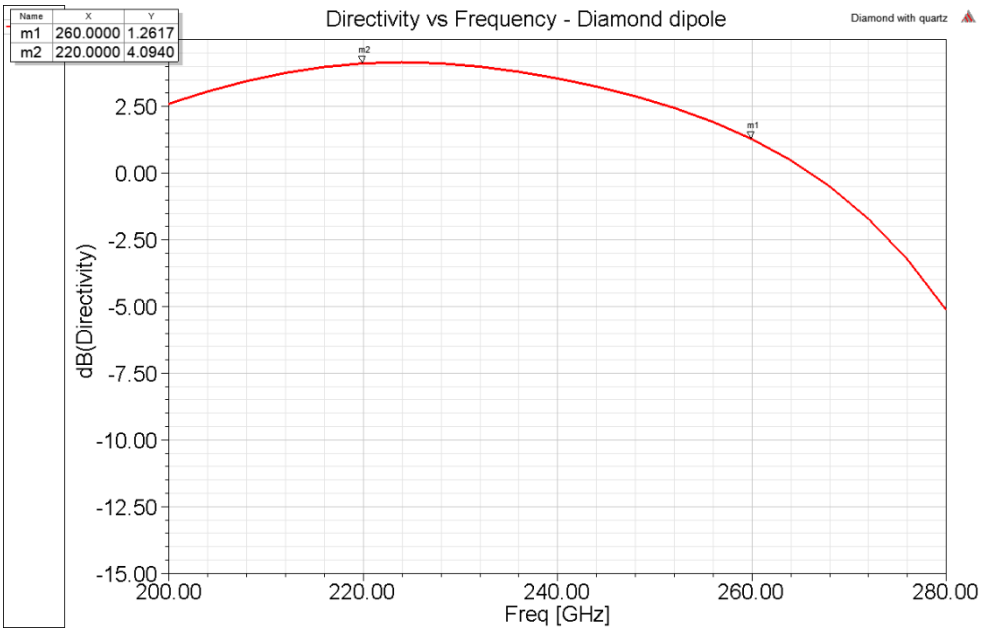


Fig. 40. Directivity at boresight of the diamond dipole.

Up to this point, different antenna designs have been presented. These designs feature either a resonant behaviour (thin dipole), a broadband behaviour (bow-tie) or a mixture of both (diamond dipole and wide dipole). A summary of all the designs presented is found in Table 2. It includes basic data regarding all the designs. As for the dimensions shown, they are referred to a single patch. In addition, it shall be remarked that height/length refer to the X axis and correspond to the height of the triangles in the case of the bow-tie (without truncation) and diamond antennas, while length correspond

to the rectangular dipoles. Similar reasoning applies to the parameter base/width.

Considering the four designs presented, the wide rectangular dipole has been chosen, as it offers the highest directivity in the direction of interest and shows a good degree of adaptation. The study of the combination of the other designs with the metallic bridge is left as a future line of work. For the rest of this work, an S11 of at least -10 dB will be required in order to consider that the system is adapted.

Table 2: Dimensions of the proposed antennas

| | Thin dipole | Wide dipole | Bow-tie | Diamond |
|---|---|---|---|---|
| Height / Length (mm) | 0.17 | 0.35 | 0.206 | 0.27 |
| Base / Width (mm) | 0.03 | 0.25 | 0.15 | 0.25 |
| S11 @ 240 GHz (dB) | -47 | -17 | -12 | -18 |
| BW -10dB S11 (GHz) | 50 | 80 | 70 | 80 |
| Dmax (dB) | 2.9 | 4.78 | 3 | 3.53 |
| ΔDmax within band (dB) | 3.5 | 1.4 | 2.4 | 2.8 |

### 6.2.3 Bridge dimensions and horn-shaped via

Once the antenna has been chosen, the dimensions of the bridge and the horn-shaped via are taken into consideration, aiming to improve the directivity in the direction of interest - downwards from the point of view of the antenna - this is, through the substrate of quartz. For this purpose, the creation of a horn-shaped via in the metallic bridge is proposed. This horn will allow, on the one hand, to **increase the directivity** in the direction of interest as well as **allow a direct illumination** of the photomixer by the optical signal. This last will be discussed further in the next section.

The proposed horn is a simple conical horn to be etched in the middle of the bridge, right below the photomixer, which will be placed in the centre of the input of horn (separated by the substrate of quartz). It has 3 main parameters to be discussed: the length of the horn and its input and output radius. Different parametric analysis have been performed and their results are shown in Appendix 1 – *Parametric analysis of the dimensions of the bridge*. After comparing the results, a length of 6mm, input radius of 0.5mm and output radius of 2.5mm were chosen. This combination offers the highest directivity in the direction of interest while maintaining a relatively low backward directivity. Fig. 41 illustrates the final design of the bridge. However, this design was observed to deteriorate the adaptation of the system. As shown in Fig. 42, the S11 parameter has been shifted and a resonance is found at higher frequencies, while it is maintained under -9dB across the band of interest.

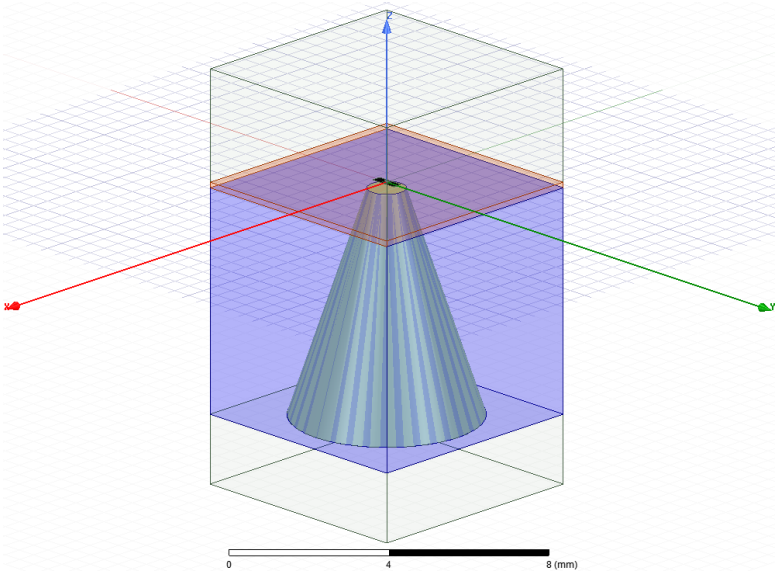

Fig. 41. Overview of the bridge structure

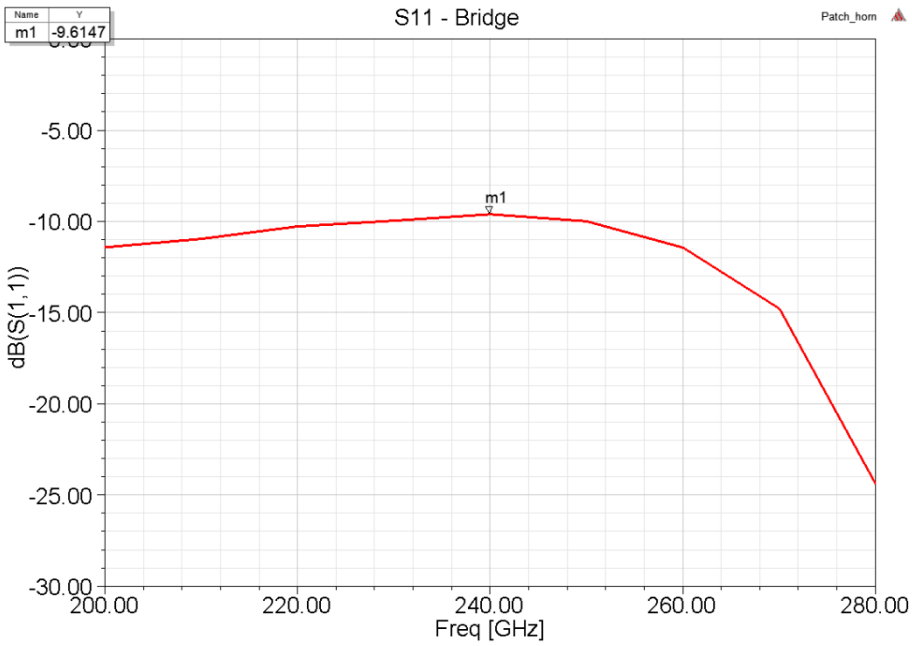


Fig. 42. Adaptation (S11) of the bridge structure with Zo=50Ω

It must be taken into account that adding the bridge structure to the analysis is more or less similar to placing a ground plane in the bottom face of the substrate for the area surrounding the photodiode and antenna. The remarkable fact is that this bridge is placed at 150 microns, in the near field of the antenna, and its exact effect cannot be determined analytically. This can, first of all, increase the propagation across the substrate. On the other hand, due to the horn-shaped via, propagation is increased in the boresight. In this case, the simulation results show a deterioration in the adaptation. Efforts have been made in order to improve it. From all the parametric analysis exposed in Appendix 1, none of the values provided a significant improvement of the S11 parameter. It is important to solve this mismatch, since it is translated into loss of radiated power. This can be seen in Fig. 43, where the directivity at boresight is compared with the realised gain (the gain of the system taking into account the mismatch loss). As highlighted by the markers in the graph, this mismatch can incur in up to 0.5 dB losses.

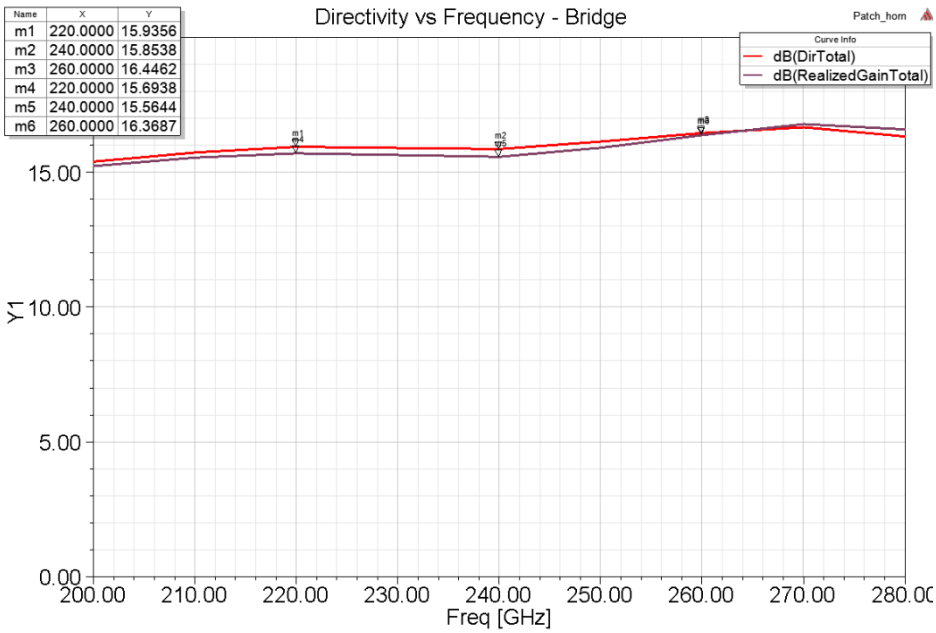


Fig. 43. Comparison between Directivity and Realized Gain for the bridge structure.

For this purpose, two alternatives were taken into consideration. On the one hand, modifying the insets in the patches could allow to fix a better feeding point of the patches and thus improve the impedance matching. On the other hand, all the dimensions of the patches shall be modified. After an optimisation process, it was observed that modifying only the insets slightly improved the adaptation of the system and the S11 coefficient was set below -10 dB. However, a second optimization process including the dimensions of the dipole delivered a remarkably better solution.

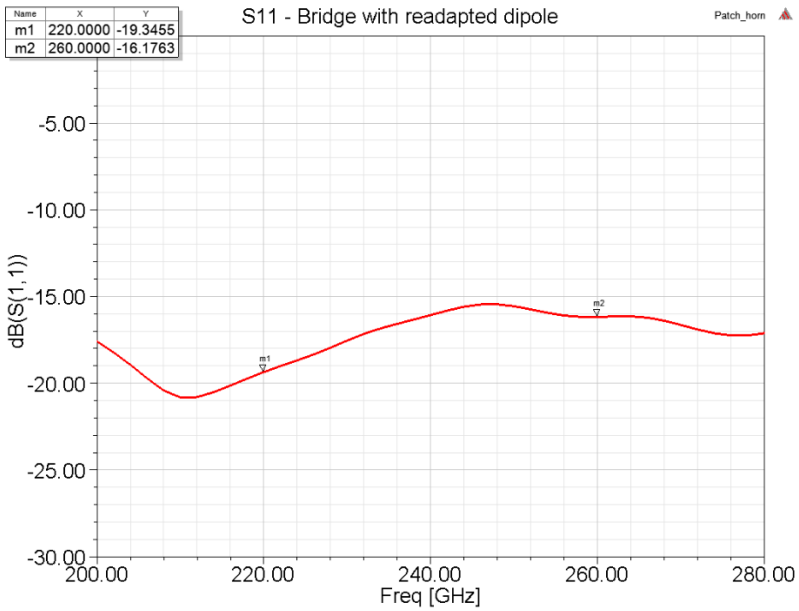


Fig. 44. Adaptation (S11) of the bridge structure with Zo=50Ω after modifying the dipole

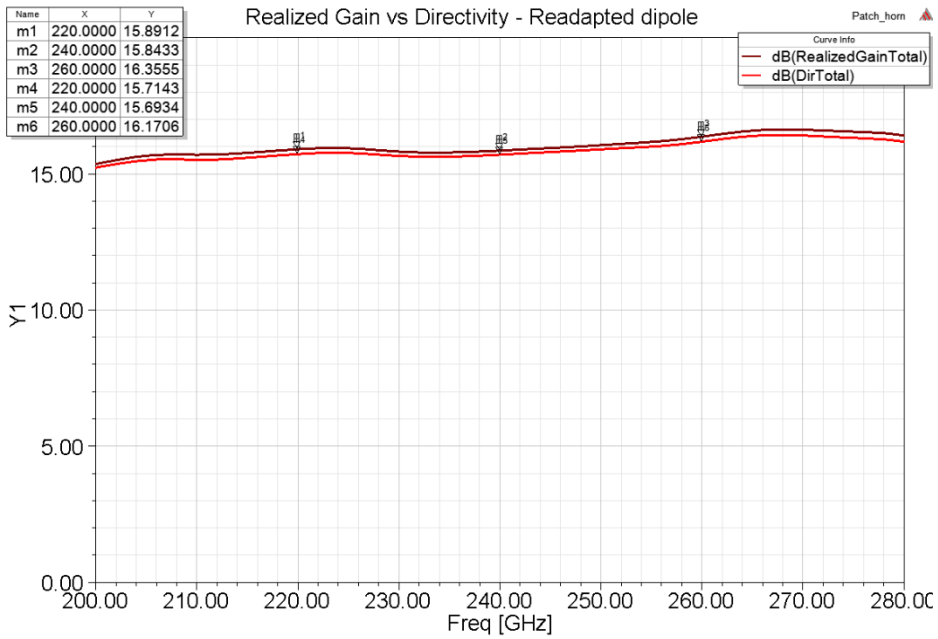


Fig. 45. Comparison between Directivity and Realized Gain for the bridge structure after readapting the dipole.

As seen in Fig. 44, the S11 coefficient was lowered up to -15 dB in the whole band and at some points even -20 dB. As a result, the matching of the antenna together with the bridge is enhanced and the calculated realized gain is higher than the directivity, as presented in Fig. 45. The new dimensions of the dipole are given in the table below.

Table 3: Comparison between the dimensions of the original and modified dipole

| Dimension | Original | Modified |
|---|---|---|
| Length (mm) | 0.35 | 0.38 |
| Width (mm) | 0.25 | 0.27 |
| Feed_r (mm) | 0.07 | 0.02 |
| Feed_w (mm) | 0.1 | 0.09 |
| Delta (mm) | 0.02 | 0.03 |

At this point, the design of the bridge and the horn have been presented. It has been demonstrated that the directivity in the direction of interest has been improved, while the back-radiation has been decreased slightly. In addition to this, it is believed that extra elements could improve the performance of the system. These elements are: director elements and corrugations/rings. The first ones aim to increase the directivity of the system by achieving an effective coupling with the dipole. These elements might remind the reader of the director elements of a Yagi-Uda antenna. The second

type of extra elements are corrugations, to be etched in the upper part of the bridge, within its boundary with the bridge; and rings, to be printed in the upper face of the substrate, within the boundary between air and quartz.

The purpose is to design these corrugations and rings as a periodic structure, creating a stop-band for the waves to propagate across the substrate. With this technique, it is expected to prevent this leakage across the substrate from taking place and instead, redirecting this power in the direction of interest. This leakage can be observed in Fig. 46, were the 3 main cuts of the radiation pattern of the structure are represented. It is observed that the value of this radiation pattern in the direction pararell to the substrate ($\theta$=90°) is between -2dB and -8dB, being the maximum value located at plane $\phi$=45°.


Fig. 46. Cuts of the radiation pattern of the bridge structure at 240 GHz

Nevertheless, these additional elements will have a bandwidth of operation as well and might compromise the broad-band performance of the system. Therefore, it will be studied whether or not including them results beneficial overall.

### 6.2.4 Director elements

In order to increase the directivity in the direction of interest, the inclusion of some director elements is proposed. Following the philosophy of the Yagi-Uda antennas, one could add passive elements to a dipole antenna in order to increase its directivity. Traditionally, two types of passive elements have been used: reflectors and directors. Reflectors are elements slightly larger than the driven element (dipole) that are placed at its rear, in the opposite direction to the one of desired radiation. Placed at a specific distance, it reflects the back-radiation and makes it interfere constructively with the forward radiation. As for directors, these are elements slightly smaller than the driven element that couple its radiation by induced currents, allowing the waves to "travel" forward. Some designs have been implemented in microstrip technology, where the different elements are printed on the dielectric substrate. One recent example is a 10dB Yagi antenna with 2 rows of directors, designed for next generation communications at 60GHz [78]. In the traditional microstrip designs, the passive elements are positioned together with the driven element in the XY plane. However, in the current design there is a fundamental limitation, given by the fact that the desired direction of radiation is downwards, through the substrate. In straight relation to this, it is not feasible to include several director elements, given the horn-shaped via right under the substrate. For this reason, a pair of director elements have been designed to be printed on the bottom face of the substrate. These elements could adopt several shapes: circular, rectangular, rings, etc. The selected shape was a rectangular ring, hollow in the middle, in order not to block the incident optical signal coming through the horn. Different parametric analysis were performed in order to obtain the optimal dimensions of these elements. Results of these analysis are presented in detail in Appendix 2 – *Parametric analysis of the dimensions of the director elements*.

These analysis show that the best coupling is achieved when the director elements are placed with the same offset than the patches of the dipole with respect to the centre, this is 25μm. Several combinations can be observed that improve the directivity in the direction of interest. The most remarkable results are compared in Table 4, where the obtained directivities are shown together with the return loss (RL) at central frequency and a 10dB RL bandwidth. A row with the value of the realized gain has been included to provide a more graphical view of the trade-off between increase in directivity and mismatch. The homogeneity of this realized gain within the band has been included as well.

Table 4: Comparison of different directors' geometries and performances.

| | 1 | 2 | 3 | 4 | 5 | 6 | 7 | 8 | 9 |
|---|---|---|---|---|---|---|---|---|---|
| Length *(μm)* | 152 | 114 | 114 | 190 | 152 | 114 | 114 | 152 | 190 |
| Width *(μm)* | 135 | 162 | 189 | 108 | 162 | 216 | 243 | 162 | 81 |
| Frame width *(μm)* | 10 | 10 | 10 | 20 | 20 | 20 | 30 | 30 | 30 |
| Dmax (dB) @ 240 GHz | 16.7 | 16.5 | 16.6 | 16.7 | 16.65 | 16.8 | 16.7 | 16.7 | 16.6 |
| Dback (dB) | 1.8 | 2.3 | 1.9 | 1.5 | 1.3 | 1.7 | 1.4 | 1.5 | 2.35 |
| RL (dB) @ 240 GHz | 10.3 | 11 | 9.5 | 10 | 9.4 | 8.7 | 7.9 | 10.1 | 11.4 |
| BW 10dB RL (GHz) | 80 | 80 | 15 | 80 | 30 | 25 | 0 | 80 | 80 |
| Realized Gain (dB) | 16.5 | 16.45 | 16.3 | 16.4 | 16.3 | 16.4 | 16.2 | 16.5 | 16.55 |
| ΔRG within band (dB) | 0.4 | 0.6 | 0.34 | 0.6 | 0.6 | 0.4 | 1.2 | 0.5 | 0.54 |

After considering all the alternatives, the directors with dimensions 190x81 (μm) have been chosen because they offer the highest value of realized gain (RG). There are other combinations that offer a higher directivity showed lower return losses and thus the realized gain of these combinations are inferior. Nevertheless, the differences between them are of tenths of decibel and manufacturing tolerances would probably turn these differences neglectable. However, since this work is based on simulation results, the solution with the best performance has been chosen.

The radiation pattern is plotted in Fig. 47. In this figure, it can be compared to the original radiation pattern, without director elements, shown previously in Fig. 46. It can be observed how the radiation is increased in practically 1 dB in the direction of interest, while the back radiation is lowered from 4 to around 1dB. This implies a reduction with a factor of 2 in the back radiation. Moreover, it can be observed that its maximum has been shifted from $14^\circ$ to $52^\circ$ and remains around 2.3 dB, a similar value to the one existing without directors. The propagation across the substrate is still denoted, ranging from 0 to -8 dB. As for the matching of the system, it is

shown in Fig. 48. Finally, the layout of the bridge including the director elements is presented in Fig. 49.

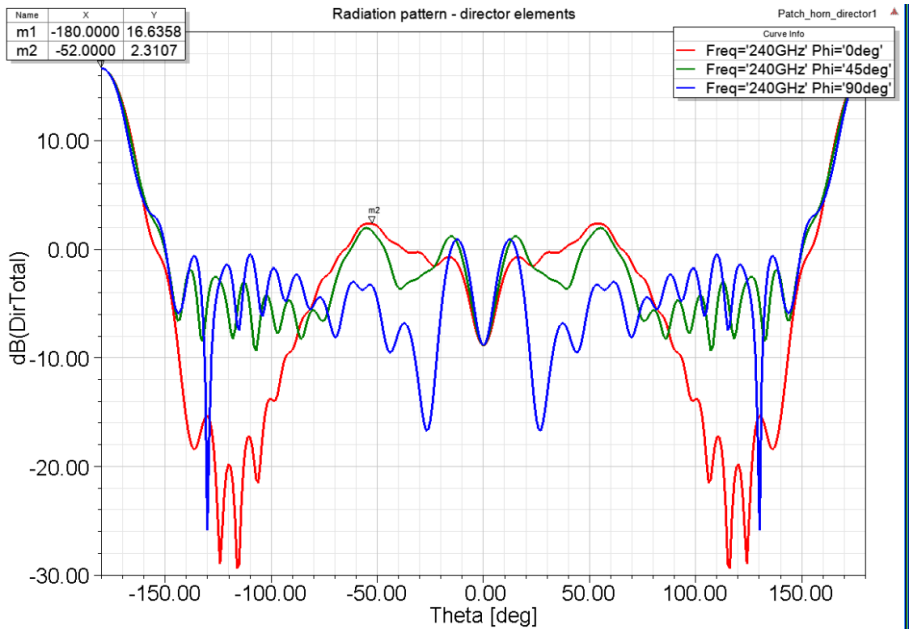


Fig. 47. Cuts of the radiation pattern of the bridge structure with directors at 240 GHz

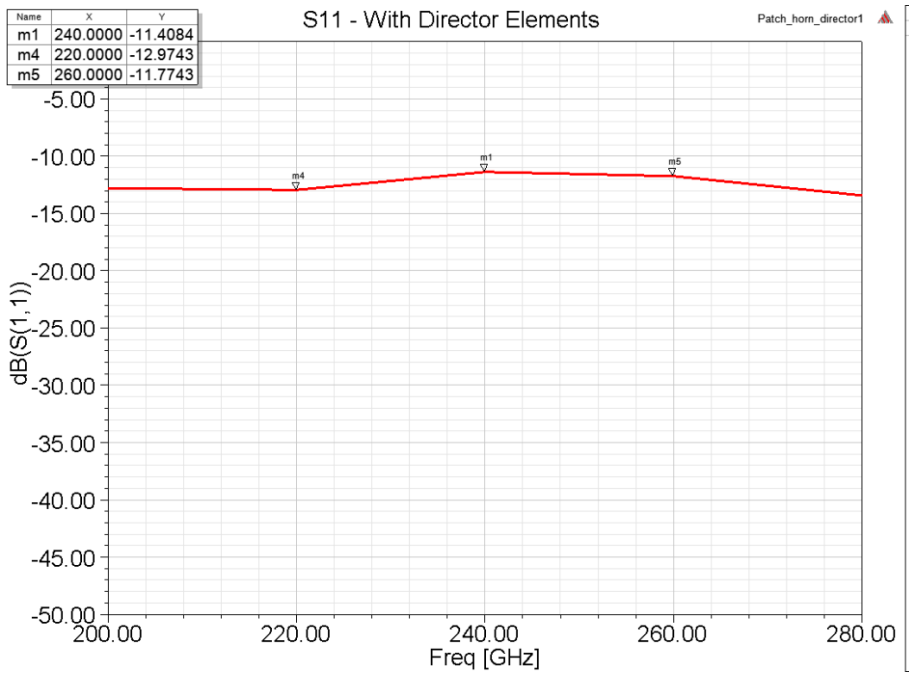


Fig. 48. Adaptation (S11) of the bridge structure with directors and Zo=50Ω

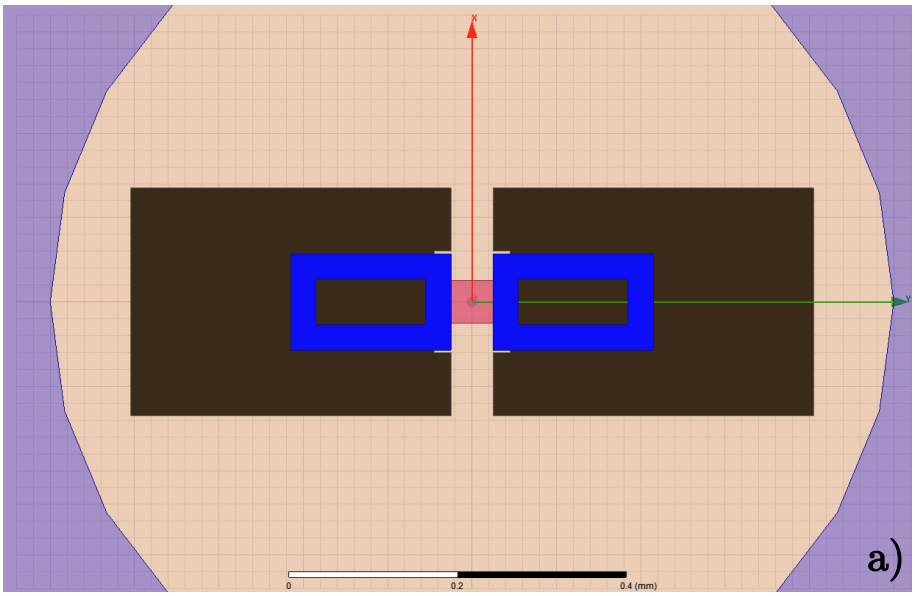


Fig. 49. Zoom into the rectangular dipole with the director elements a), and layout of the bridge including dipole, substrate, directors, horn and radiation box.

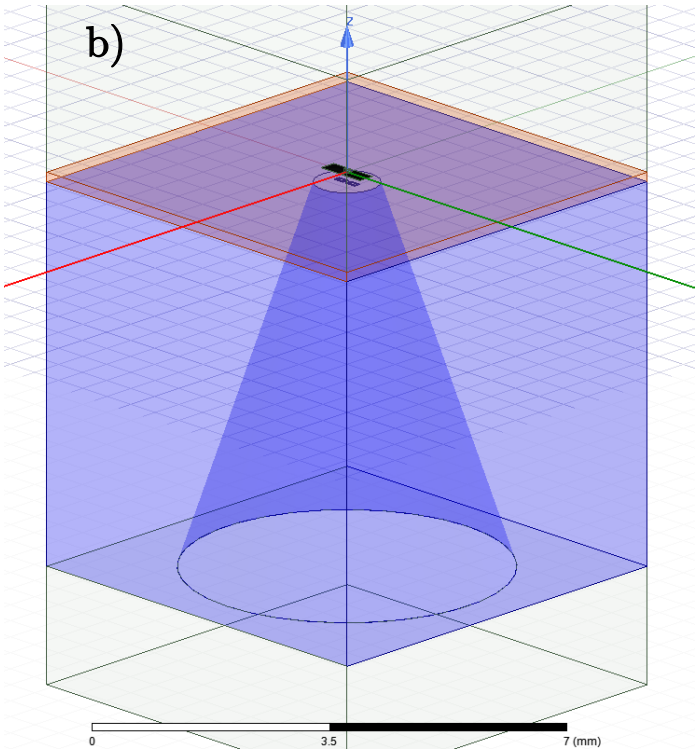

### 6.2.5 Corrugations and rings

As stated in section 6.2.3, a combination of corrugations and rings could be designed in order to prevent substrate modes to propagate. Some parametric analysis have been performed but any straightforward relationship has been found. It is believed that a more exhaustive analysis could be able to draw some conclusions in this regard. However, special attention shall be paid to the frequency response of these elements, since they usually offer a narrow-band response. Nevertheless, it could be explored whether combinations of rings and corrugations with different pitches could offer a broader-band operation. Moreover, the use of rings might interfere with the metallic paths for DC bias and the effect of splitting this rings might be interesting to be studied.

Due to limited time availability and computational costs, this analysis could not be performed and is left as one of the lines of future work.

### 6.2.6 Conclusions

All in all, the proposed bridge structure provides a handful of functionalities. First of all, the bridge supports the substrate on which the photomixer is placed, thus allowing the THz generation. Secondly, it allows to directly illuminate the photomixer through the horn-shaped via etched in the middle of the bridge. And finally, it enhances the radiation of THz in the direction of interest. Different trade-offs were dealt with within the design of the structure: such as the thickness of the substrate and the dimensions of the different elements, such as the dipole, the bridge or the directors. The different analysis taken into consideration could be broaden to different geometries, such as the shape director elements or higher sampled ranges of values for the parametric sweeps. Nevertheless, the final results are satisfying and sufficient for the next stages of design.

### 6.3 Focus 2: Energy collection

Provided that the ellipsoidal reflector redirects and gathers the energy in its second focus, some type of structure must be included in order to collect and output the energy. **Horn antennas** are believed to successfully achieve this purpose. As in a reflector configuration where a horn feeds a reflective dish, a horn antenna could be placed in the focus of the ellipsoidal reflector. In principle, it is suggested that the phase centre of this horn shall be placed at the very precise location of the focus, since the phase centre is the origin of the spherical waves emitted by the horn. However, it shall be argued whether the proposed ellipsoidal configuration allows the formation or spherical waves or not, since far-field condition might not be achieved. Therefore, a spatial offset between the phase centre and the focus of the ellipse might be considered.

A theoretical study of this wave formation was considered to be out of the scope of this Master Thesis and further efforts shall be made regarding this topic. As for what this work is concerned, the position of the antenna will be estimated via simulation.

In principle, in could be believed that any horn antenna specifically designed for the 240 GHz band could be suitable for this purpose. Nevertheless, highly directive horns shall not be suitable, since the main lobe might be too narrow. Since the waves arriving to the second focus might come from a wide range of angles, a relatively wide main lobe is desired. A 240 GHz horn antenna had been recently designed and was measured at UPNA Labs during the course of this project and was considered to be suitable for this purpose. The 3D model of the horn is shown in Fig. 50. Its phase centre at the central frequency is located at approximately 1.6 mm from the aperture into the horn.

The antenna includes a 2-step circular to WR4.3 rectangular waveguide transition and was designed to have around 12 dBi gain at boresight. Appendix 3 – Far-Field and Near-Field measuring , details the measuring process and compares the simulation results with the measured ones. The directivity of this horn is relatively low and has around 52 degree HPBW (Half-power beam width), as shown in Fig. 51.

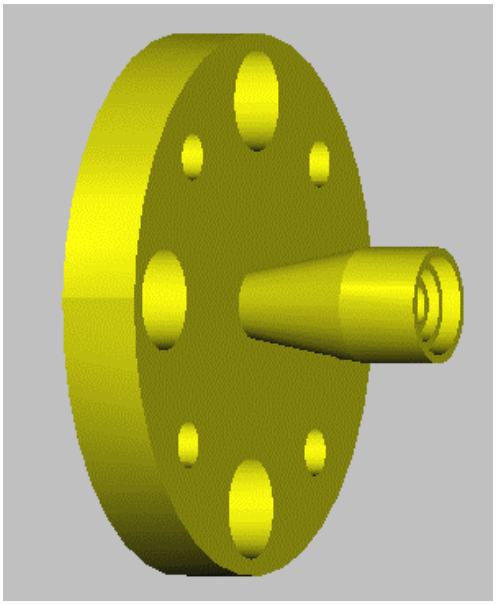

Fig. 50. 3D Model of the choke horn antenna.

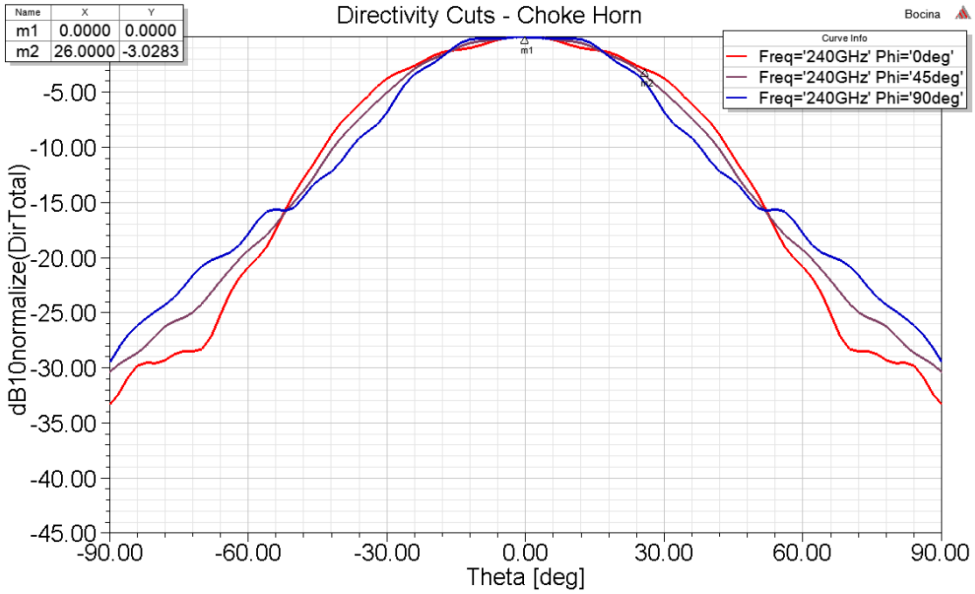


Fig. 51. Simulated radiation pattern and HPBW of the choke antenna.

## 6.4 Optical illumination

The fibre collimators selected for this purpose include a GRIN (Graded Index) lens for beam collimation, available at [79]. They provide a beam diameter of 0.5mm with a beam divergence of 0.25°. The maximal optical power in continuous wave operation supported by the device is 300 mW and the collimator bandwidth is ±30 nm around the central wavelength, 1550nm. This linewidth corresponds to a 3.74 THz frequency bandwidth at 1550nm, as it can be calculated using Eq. 17. Therefore, the collimator supports the

transmission of 2 optical signals separated 240 GHz and is suitable for the aim of this work.

$$\Delta\upsilon = \frac{c}{\lambda^2} \cdot \Delta\lambda \qquad \text{Eq. 17}$$

The geometry of the connector is shown in Fig. 52. They are usually employed in pairs, with a working distance of 15±5 mm. This working distance has been defined by the company in terms of power transmission percentage and insertion losses measured between both elements of the pair. The output optical beam is considered Gaussian. At a distance of 15mm, the minimum insertion loss of 0.3 dB is achieved. For this reason, a distance of 15mm would initially be fixed between the connectors (half distance between each connector and the photomixer) since maximum, incident, optical power should be achieved. These collimators have been characterised by the manufacturer and the typical values of insertion loss and transmission coefficient, extracted from [79], are shown in Table 5. One of the connectors will be placed with some inclination angle with respect to the vertical axis while the second element of the pair is placed specular to the vertical axis in order to try to collect any possible reflection of the optical beam after irradiating the photomixer. However, at it will be explained further in this section, the optimal distance could not be achieved due to geometrical limitations.

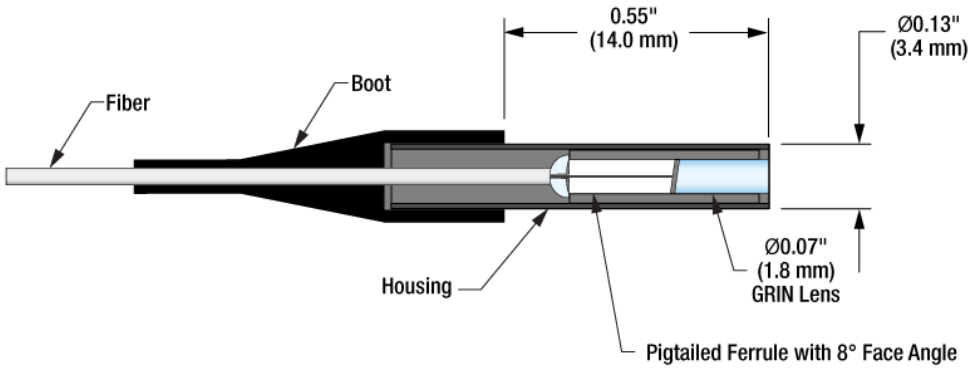


Fig. 52. Geometry of the selected GRIN Collimator [79]

Given the geometry of the collimators, it was possible to determine their position in the final device. As a first consideration, it could be stated that maximizing the angle of inclination of the collimators with respect to the vertical axis is aimed. This is due to the fact that the maximum of radiation from the photomixer remains in this axis, thanks to the horn etched in the metallic bridge. Therefore, it should be avoided to place the connectors near this axis, since a hole must be made in the surface of the reflector in order to

irradiate the photomixer. On the other hand, there is a fundamental limitation in the angle of inclination given by the horn in the bridge.

Table 5: Characterization of the selected collimators

| Working Distance (mm) | Insertion Loss (dB) | Transmission (%) |
|---|---|---|
| 1 | -0,6 | 87,10 |
| 5 | -0,52 | 88,72 |
| 10 | -0,47 | 89,74 |
| 15 | -0,3 | 93,33 |
| 20 | -0,33 | 92,68 |
| 25 | -0,39 | 91,41 |
| 30 | -0,57 | 87,70 |
| 35 | -0,51 | 88,92 |
| 40 | -0,66 | 85,90 |
| 45 | -0,82 | 82,79 |
| 50 | -0,98 | 79,80 |
| 75 | -1,92 | 64,27 |
| 95 | -2,32 | 58,61 |
| 125 | -4,08 | 39,08 |
| 140 | -5,1 | 30,90 |
| 153 | -5,4 | 28,84 |

As shown earlier in this Chapter, the horn that has been designed to be etched in the metallic bridge consists of a conical aperture with a length of 6mm, an input radius of 0.5mm and an output radius of 2.5mm. Since direct irradiation of the photomixer is required (relying on multiple paths is not trustworthy and could incur in additional loss of power), the optical beam cannot exceed the flare angle of the horn (is this case, the beam would travel quasi-parallel to the walls of the horn). Additionally, a 150 μm-thick layer of quartz is placed in order to support the photoconductive antenna and it should be taken into account in the calculation, in order to precisely focus the optical beam. This maximum angle can be easily calculated by means of trigonometry, as shown in the following formula and illustrated in Fig. 53:

$$\tan(\alpha) = \frac{y}{z} = \left(\frac{r_{out} - r_{in}}{l_{horn} + h_{quartz}}\right) = \frac{2}{6.15} \qquad \text{Eq. 18}$$

$$\alpha \cong 18°$$

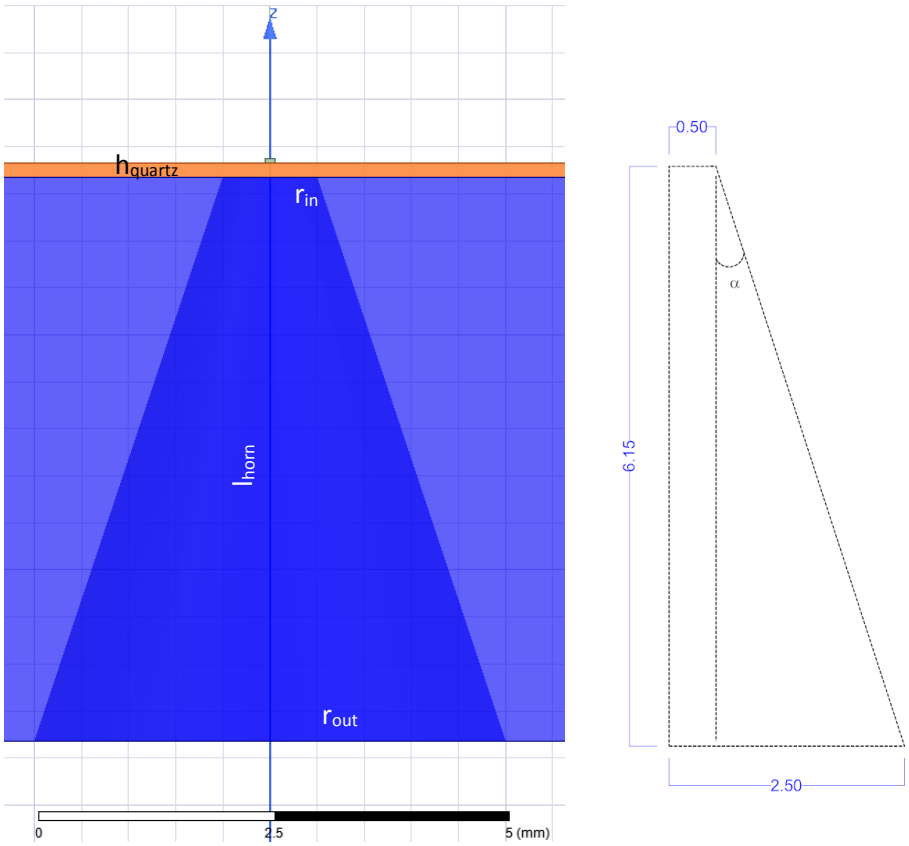

Fig. 53: Calculation of the angle of inclination

Once this angle was fixed, the position of the connectors was determined. First of all, due to the fundamental limitations of the working distance and the maximum angle of inclination, the connectors were placed right under the photomixer, so that the optical beam would travel quasi-parallel to the wall of the horn and also in order to minimize the distance to the photomixer. However, the design of the reflector, presented earlier in this section, incurred in some geometrical restrictions: The chosen eccentricity of the ellipsoid and the position of the bridge result in a minimum feasible distance greater than the optimal working distance. As an example, only the length of the bridge is 6mm and the optimal working distance would be 7.5mm from the lens of the collimator to the photomixer. In case of adopting this configuration, the connectors would intersect the surface of the reflector and the focalisation on the second focus would be lost. For these reasons, a distance of 20mm between each collimator and the photomixer was chosen. This allows to place the connectors slightly under the reflector so that the size of the hole made in the reflector is reduced, thus decreasing the aberration in the reflective process. The designed geometry results in a total working distance of 40mm, instead of the optimal 15mm. As can be extracted from Table 5, this value involves a 0.3dB extra insertion loss. This was assumed acceptable, since it

does not incur in a great loss of power. Moreover, the values shown in this table correspond to a scenario where the two collimators are placed in from of each other without any obstacle or body in between. Therefore, whereas they provide an approximate idea of the performance of the system, this values might not be directly applicable to the current scenario. It is believed that the performance of the collimators will be satisfactory and the actual performance shall be checked through an actual measuring process once the photomixer is available. The final geometry of the connectors is shown in Fig. 54. The blue layer represents the metallic bridge, in which the horn (dark blue) is etched. The thin, orange layer on top of if corresponds to the quartz substrate. Connectors are shown in grey. The yellow lines represent the optical beams, with a collimated diameter of 0.5mm. Finally, a lighter cylinder is observed starting at the end of the connectors. That corresponds to the hole that is made in the reflector. Its radius correspond to the radius of the lens (0.9mm) and it has been chosen in order to provide enough space for the optical beam to propagate without colliding with the walls while reducing the size of the holes to be machined in the reflective, elliptical surface, since this holes incur in an aberration of the focalisation.

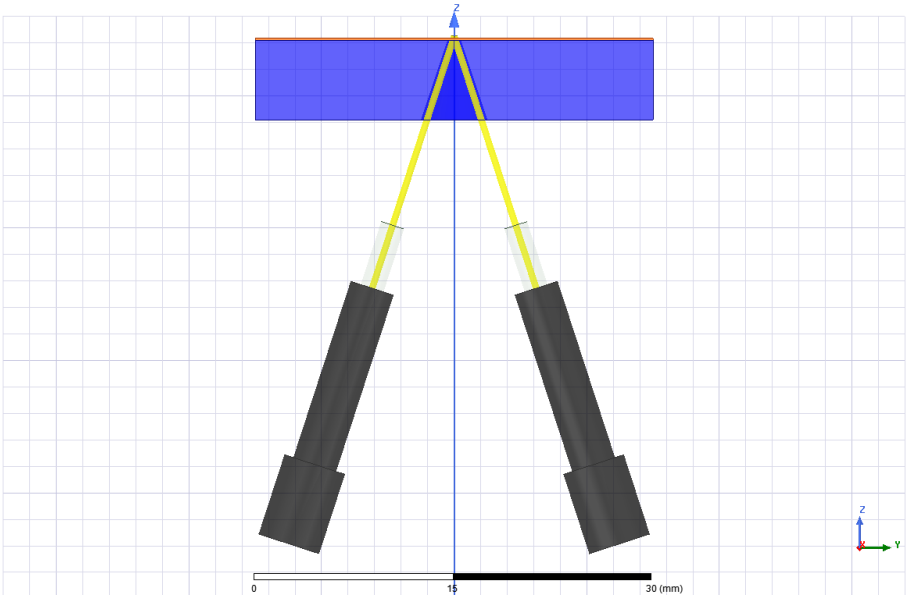


Fig. 54: Final geometry of the optical connectors

# 7. Proposed assembled model and simulation results

Once every fundamental piece of the component was designed, the challenging task of assembly and integration arose. Different approaches have been proposed and simulated. The fibre collimators were excluded from simulation at the beginning of this process and would be included later, in order to check the effect of introducing holes in the reflective surface.

## 7.1 Rotated ellipse

As a first approach, an ellipsoidal cavity rotated 45 degrees with respect to the XY plane was simulated. The piece can be observed in Fig. 55. The red dots correspond to the foci of the ellipse. At first, it was believed that locating the antenna at the position of the focus would be more accurate than placing the aperture, since the photodiode is the source of the radiation. However, the horn rearranges this radiation and therefore its phase centre could be considered as the actual source of the waves. However, it was decided to place the aperture at the focus instead of the diode because the bridge has a significant size in comparison to the cavity and placing it with respect to the diode would incur in a deterioration of the performance due to the proximity of the edges of the bridge to the reflective surface. In this scenario, the choke horn presented in the previous chapter has been included and placed at the second focus.

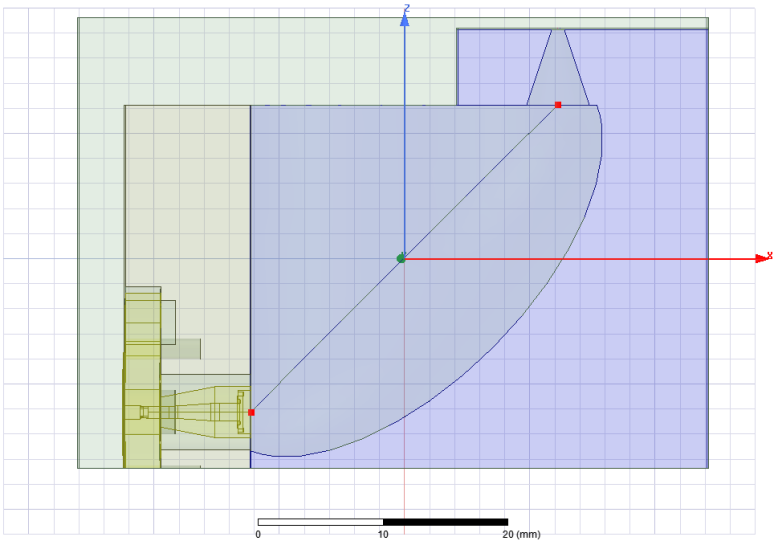


Fig. 55: Ellipsoidal cavity rotated 45 degrees with choke horn.

The horn antenna has been inserted into a metallic wall. This horn would be attached to the integration block through some alignment pins and screws in a real implementation. Two full wave simulations were performed with HFSS: first, with a radiation boundary after the choke horn, in order to

obtain a representation of the fields in the cavity, which can be observed in Fig. 56. Secondly, this radiation boundary was substituted by a wave port, in order to obtain the S21 parameter of the system. These two simulations were required because after adding at the second port, the plotted fields were the sum of two excitations. It was not possible to find a way of plotting the individual contribution of only one excitation.

Looking at Fig. 56 it can be observed how the maxima of the E-field follow a curved trajectory that could be approximated to the curvature of the ellipse. Moreover, it can be observed how the field enters the waveguide placed after the horn. As a consequence, the simulation yielded a very good matching, as shown in Fig. 57.

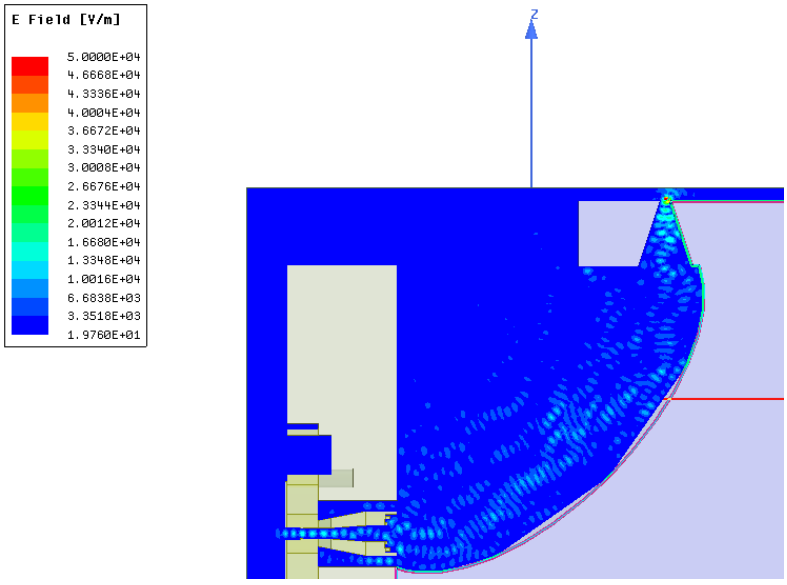


Fig. 56: E-Field in ellipsoidal cavity rotated 45 degrees with choke horn.

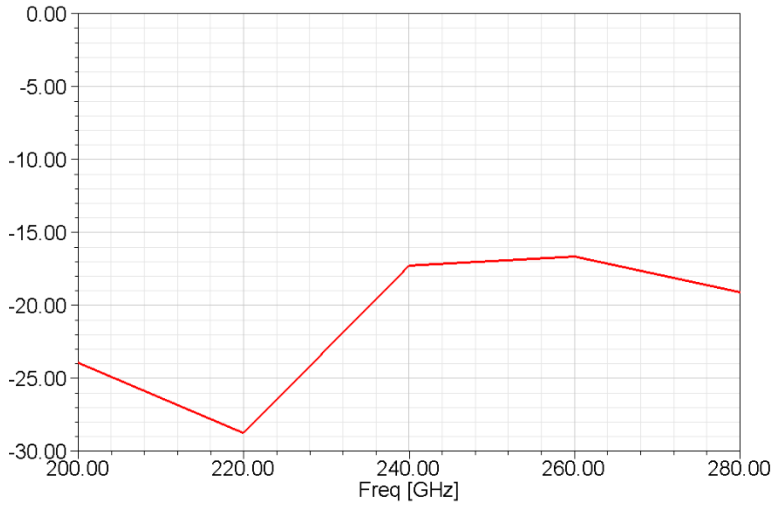


Fig. 57: S11 [dB] parameter in ellipsoidal cavity rotated 45 degrees with choke horn.

However, the simulation with two ports yielded a low transmission coefficient. Two perpendicular modes were defined in the output port, in order to check if the polarization was maintained. It this scenario[3], horizontal polarization was defined as the copolar polarization, since the diode and microstrip antenna were placed parallel to the XY plane. It was observed that the S22 for the crosspolar mode resulted below -90 dB and thus it was concluded that the polarization was not being modified. However, the S22 for the copolar mode was very low, as seen in Fig. 58. Therefore, it can be agreed that there is a significant loss of power. These loss could be due to the open boundary on the upper part of the cavity as well as due to the poor matching of the second port. In addition, the phase centre of both horns might not be properly positioned with respect to the foci and that would incur in spherical waves not being generated. Moreover, the proximity of the ellipsoidal surface and the sharp edges of the piece could be compromising the far-field operation.

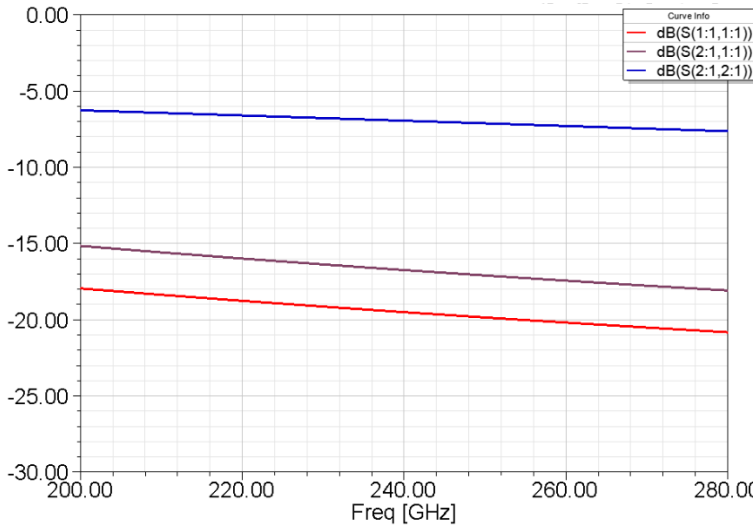


Fig. 58: Sij [dB] parameters in ellipsoidal cavity rotated 45 degrees with choke horn.

At this point, it is important to remark that in this scenario only a "face" of the ellipsoidal cavity is used. It was believed that closing the piece on the upper side by the symmetrical ellipsoidal face would increase the performance. Thus, it was decided to analyse the case with the complete ellipsoid. However, it was unexpectedly observed that the performance was deteriorated. As shown in Fig. 59, several incoherent reflections take place in the inside, and the energy is spread along the cavity, not being focalized at the second focus. This could be due to the existence of sharp edges due to

[3] In this scenario, the frequency sweep was performed via an interpolation method in order to ease the computational requirements. This method is not as accurate as the discrete method that had been used it all the previous simulations that have been presented, but it was the only cost-reasonable way to perform the simulation.

the bridge and the piece that supports the choke horn. Moreover a misalignment of the phase centre of the horn with respect to the focus shall be taking place.

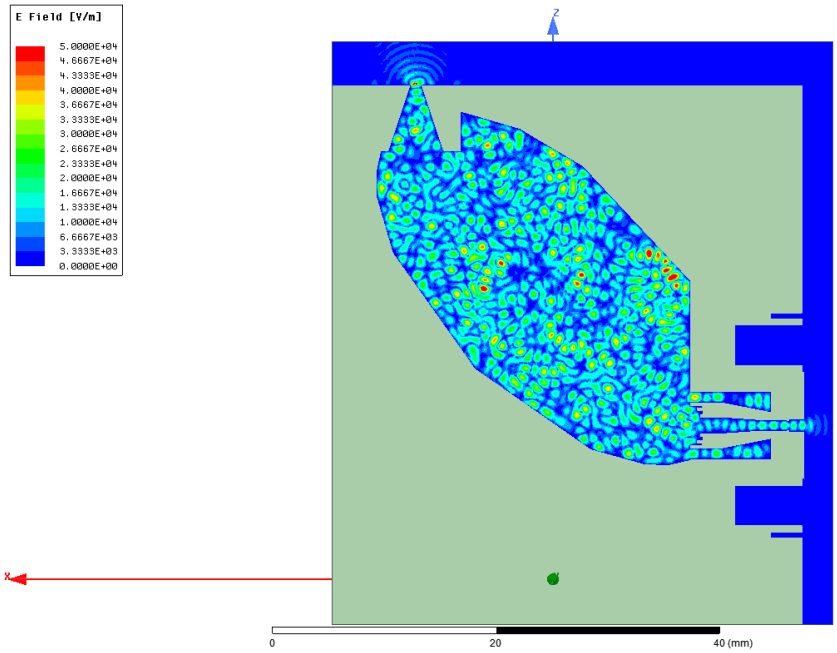


Fig. 59: E-Field in enclosed ellipsoidal cavity rotated 45 degrees with choke horn.

Since results were not as good as expected, a new structure was proposed consisting on a horizontal cavity.

## 7.2 Horizontal ellipse

In order to avoid some of these sharp edges presented in the rotated model, an ellipsoidal cavity was simulated in horizontal position. The bridge structure was placed at one of the foci, perpendicular to the major axis of the ellipse, with the microstrip dipole placed exactly at the focus. As well as in the previous case, there were doubts whether to match the position of the focus with the position of the diode or with the aperture of the horn in the bridge. It was believed that locating the antenna at the position of the focus would be more accurate than placing the aperture, since the photodiode is the source of the radiation. However, the horn rearranges this radiation and therefore its phase centre could be considered as the actual source of the waves. Both scenarios, shown in Fig. 60, were simulated in order to check their performance. The blue colour stands for PEC, while red represents vacuum. The thin, orange layer corresponds to the quartz substrate. A full ellipse was simulated with the corresponding E- and H- symmetry planes, in order to alleviate computational requirements. In fact, these planes allowed to effectively simulate the structure, since more than half million tetraedra

were meshed in only a quarter of the structure. The ellipsoidal surface was defined as a perfect E boundary. The cavity was truncated at the second focus in order to check whether the energy concentrates around this point and the intersected surface was defined as "radiation", in order to avoid infinite reflections of the fields. The part of the ellipse that was left behind the diode was also defined as radiation boundary in order to avoid the back radiation to affect the simulation.

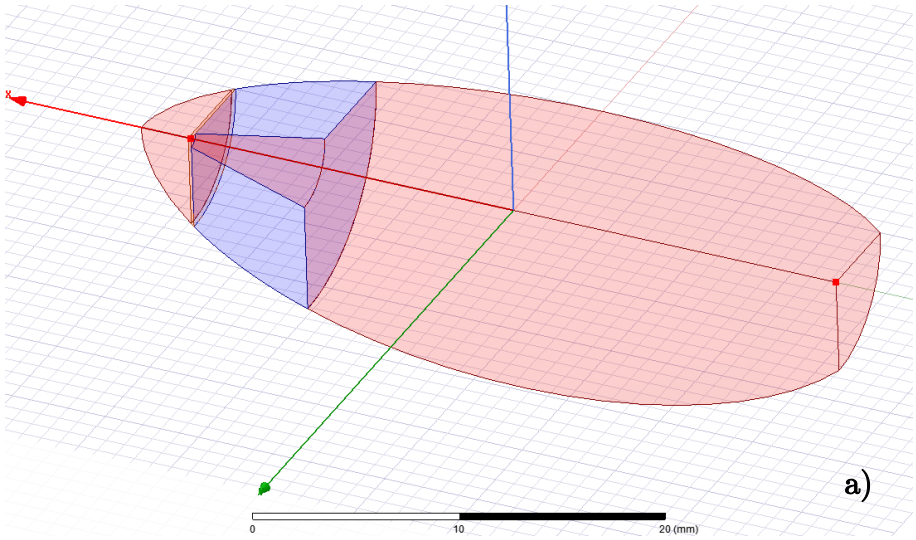


Fig. 60: Horizontal cavity with bridge at one focus. a) Diode placed at focus. b) Aperture placed at focus. Red dots represent the foci.

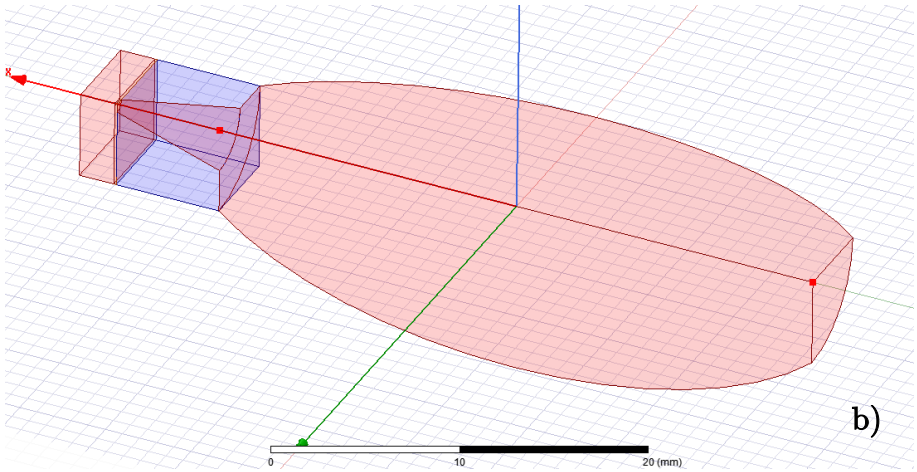


After simulating both scenarios, it was observed that a) provided much better matching than b), as can observed comparing Fig. 62 and Fig. 64. The frequency sweep in this case was limited to 5 discrete points between 200 and 280 GHz due to the computational requirements of the simulation and the desired of accuracy. Nevertheless, it can be seen that the S11 parameter remains below -10dB in scenario a). Of course, some peaks could be found in between these points, but all in all, in seems to reproduce similar results to

the matching of the bridge, shown in Fig. 44. In addition, it can be seen in Fig. 61 and Fig. 63 that the gathering effect is taking place in both, but the E-field is stronger in scenario a).

**Scenario a):** Diode placed at focus.

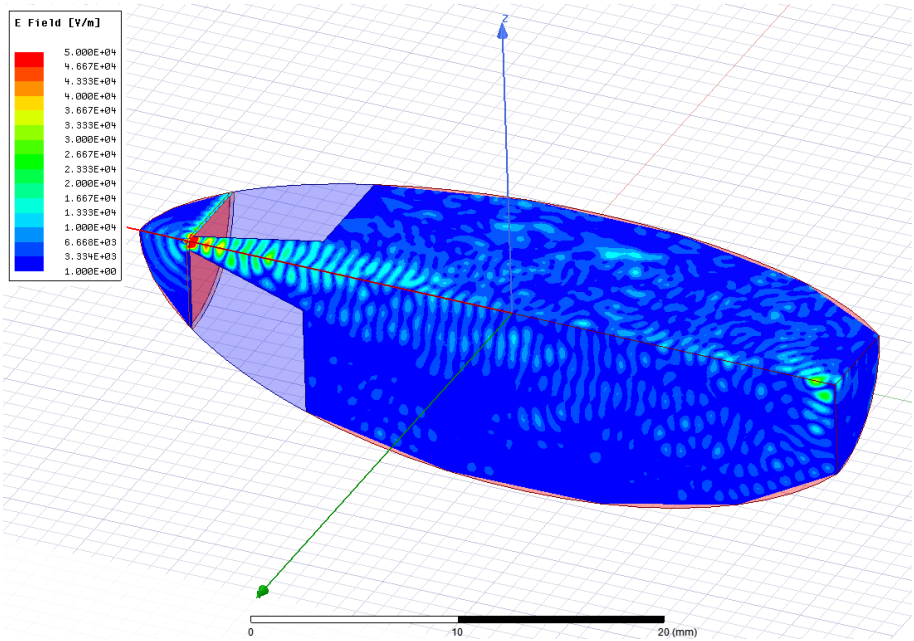


Fig. 61: Strength of the E field in scenario a) Diode placed at focus.

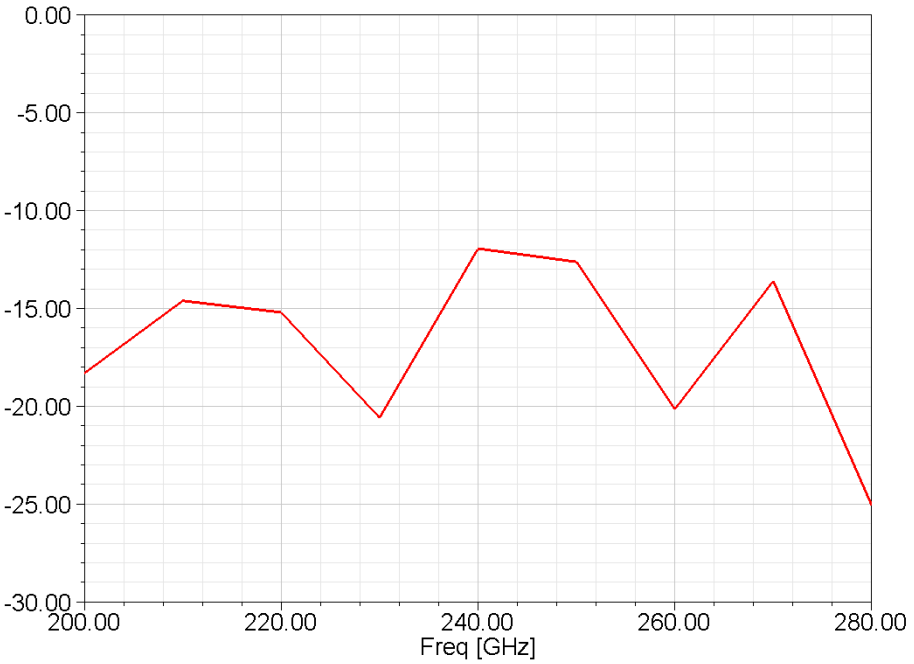


Fig. 62: S11 [dB] parameter in scenario a) Diode placed at focus.

**Scenario b):** Aperture placed at focus.

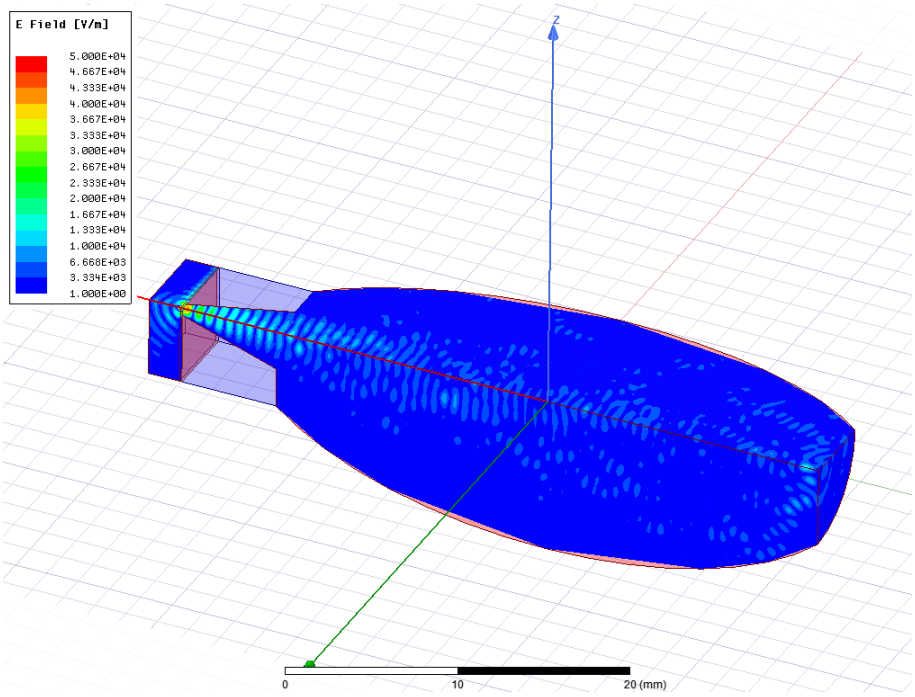


Fig. 63: Strength of the E field in scenario b) Aperture placed at focus.

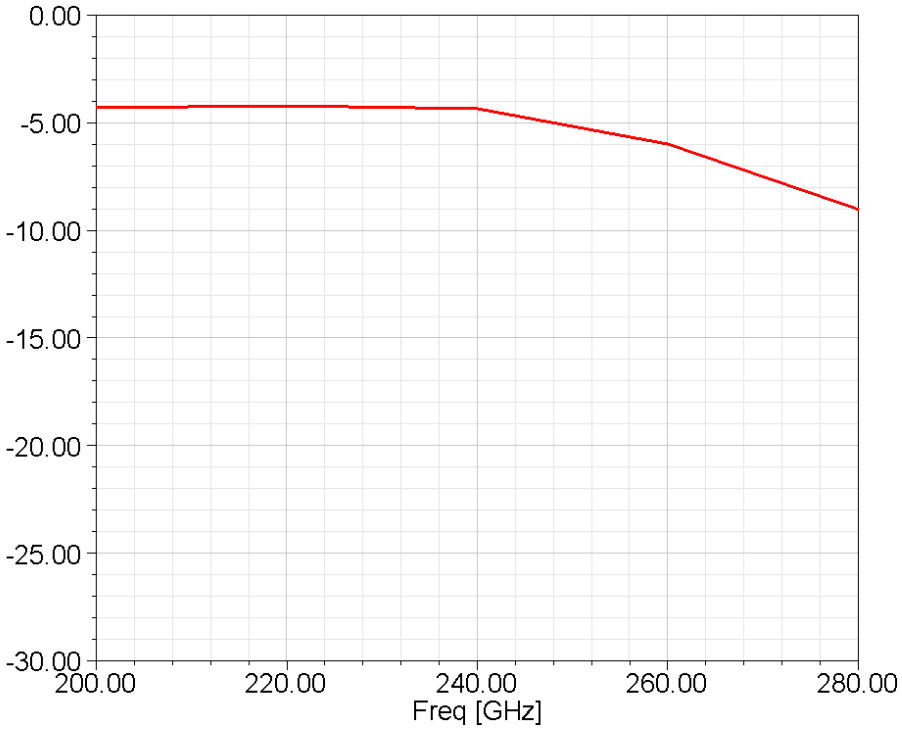


Fig. 64: S11 [dB] parameter in scenario b) Aperture placed at focus.

In this configuration, the bridge was placed perpendicular to the major axis and as a consequence there was a straight Line of Sight (LoS) between the input and output along the major axis. The idea behind this configuration was to take advantage of this LoS in order to maximize the output power, and use the elliptical surfaces to redirect any radiation that deviates of this direct path. The fact why scenario a) concentrates more energy at the second focus could be due to a more proper formation of spherical waves. After this first approach with the horizontal configuration, the choke horn was added. It was placed at the second focus, being the aperture slightly shifted from that position, into the cavity. With this shift, a better approximation to aligning the phase centre together with the focus was aimed.

An interpolation method was chosen for sweeping in frequency, in order to alleviate computational requirements. As in the rotated case, two simulations were set up: one with a radiation boundary and one with the wave port. As shown in Fig. 65, the energy is coupled into the choke horn and its input waveguide. When observing the S-parameters of the system, in Fig. 66, it can be observed how the S21 parameter is better in comparison to the rotated configuration.

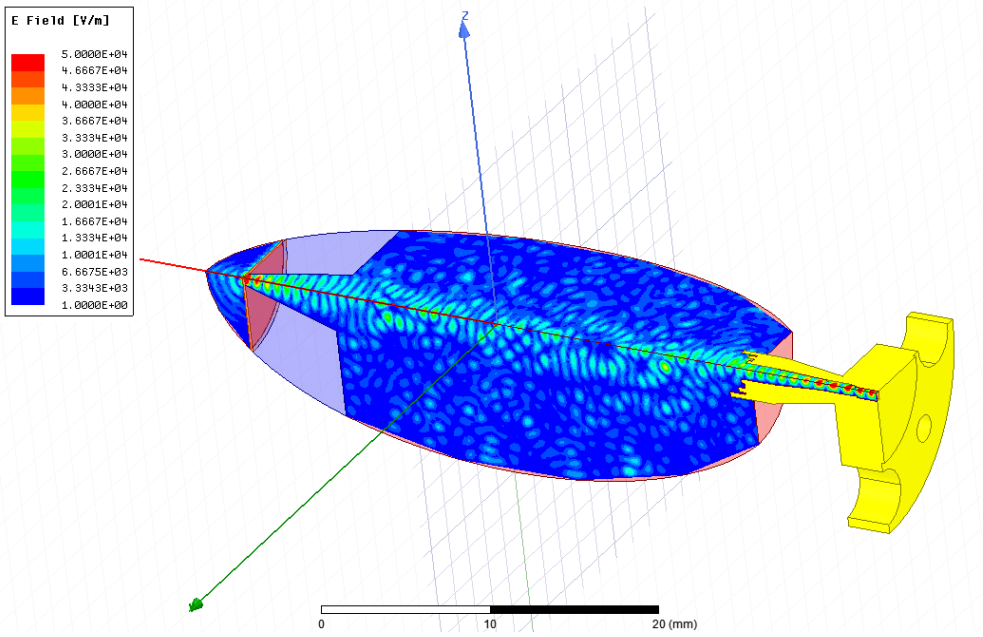

Fig. 65: Strength of the E field in the a) scenario including choke horn.

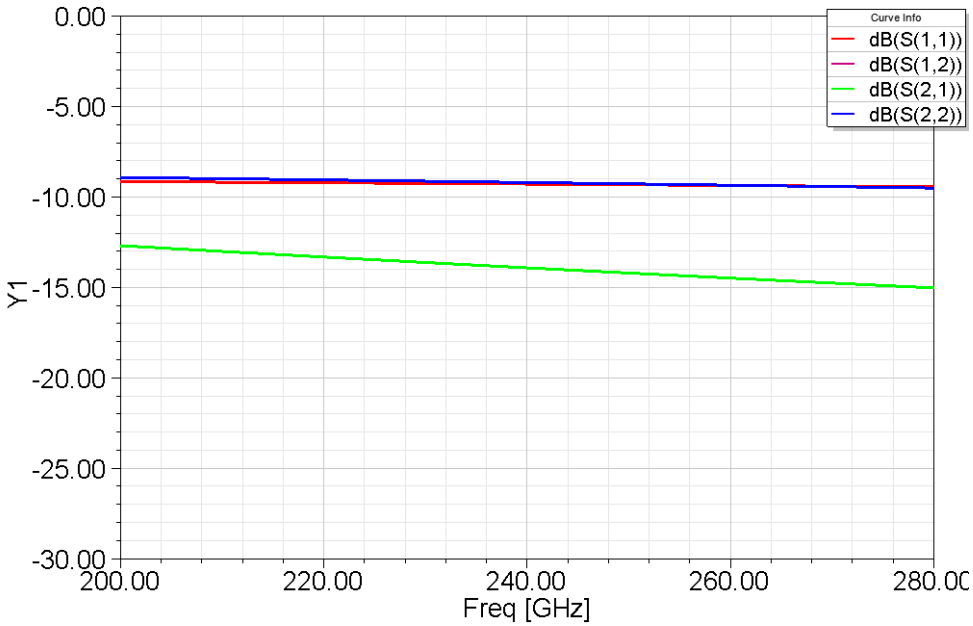


Fig. 66: Sij [dB] parameters in ellipsoidal cavity rotated 45 degrees with choke horn.

## 7.3 Conclusions

In this Chapter, a series of approaches to assemble the different parts presented in previous sections have been presented. It has been observed that the ellipsoidal cavity effectively reflects the waves and focalize them into the second focus. While good matching has been obtained, however, it has been observed that adding the different parts to the system affects the propagation of this waves and thus the performance is deteriorated. This could be due to several reasons. One of them is that the operation could be falling into the near-field region, where the waves have not adopted a spherical phase front. Moreover, it had been stated previously that the ellipsoidal reflector includes a phase error in the system. On the other hand, the horizontal configuration enhances the power transmission, although still remains low. One of the drawbacks of this configuration would be the need of rearrangement of the fibre collimators and the need of some waveguide bends in order to integrate the component with the rest of components in the generation system.

Nevertheless, it is believed that this approaches establish an interesting starting point for future studies and designs, at it can be agreed that some benchmarks have been validated. Future research on this topic is foreseen in the near future and it is expected to obtain better results. With these results, conclusions will be drawn on the configuration to be used: the horizontal or the rotated cavity.

# 8. Manufacturing

The final device could not be manufactured in metal due to time constrains. However, some prototyping had been done with 3D printing techniques. The model chosen for this fabrications was the rotated one. Although it seems to offer a worse performance, it was the first model to be designed and thus first attempts to manufacture the device were made with this model. At first, it was desired to fabricate a 3D model and metallize it to check its performance but the constant changes of the piece made it impossible to find time for it. Nevertheless, these techniques allowed us to have a visual impression of the piece itself. Moreover, it could be possible to detect the most critical parts for the manufacturing process, as well as design errors.

A first attempt was made trying to fabricate the packaging as a whole piece – excluding the substrate. This attempt was significantly illustrative, since several mistakes were found. In addition, after this attempt it was decided that the best solution would be manufacturing the piece in different parts and assemble them together. In order to assemble them together, alignment pins and in some cases, screws, were added to the model. This attempt consisted of 3 different approaches, orientating the piece in different directions. One of them was orientated horizontally. The second was built vertically and the third was rotated 45 degrees and supported with some pillars.

These pieces were fabricated with the 3D printer BQ Witbox 2 [80], which works under the FFF (Fused Filament Fabrication) process that uses a filament of thermoplastic material. This filament is melted and extruded in order to conform the final piece. The provider assures that an accuracy of up to 20 microns could be achieved. However, our approach reported errors in the order of millimetres.

Fig. 67 to Fig. 70 show the different pieces. It can be observed how different orientations reported better or worse accuracy in the different axis of the piece. For example, the horizontally-grown piece offered a significantly deteriorated elliptical surface, at the same time the alignment pins and the horn in the bridge were the most accurate out of the three versions (although they were not accurate enough). On the other hand, the vertically-grown piece reported the best flange. However, the hole in the bridge and the alignment pins were barely non-existent. The rotated piece reported the worst accuracy. This could be due to the addition of slim columns in the 3D model in order to support the piece and the later removal of these columns. However, the ellipsoidal cavity was too rough in order to be used as a reflector, and thus this printer has been proven to be unsuitable for our

purpose. Nevertheless, this first approach made us consider the fabrication of the bridge as a separated part from the rest of the piece.

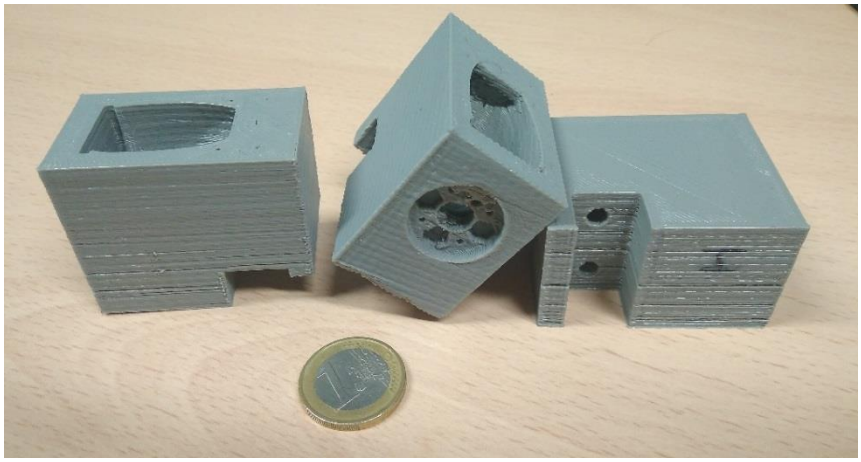

Fig. 67: Growth position of the pieces made with FFF (Vertical / Rotated / Horizontal).

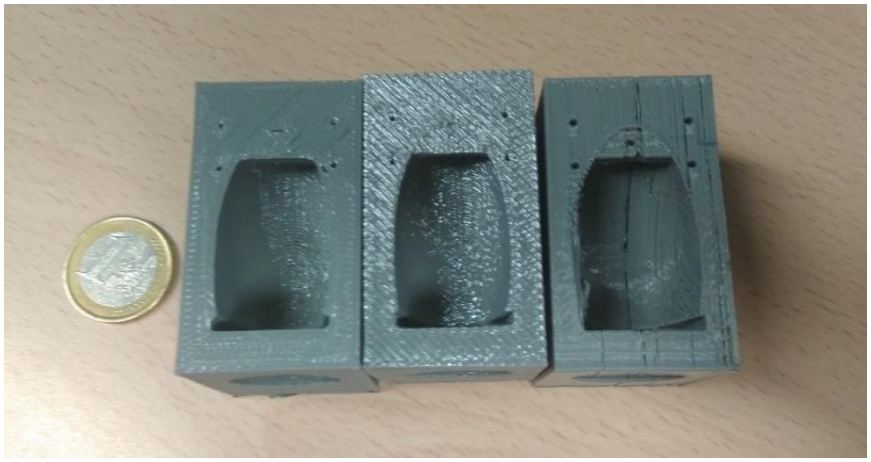

Fig. 68: Top view of the pieces made with FFF (Vertical / Rotated / Horizontal).

Fig. 69: Front view of the pieces made with FFF (Vertical / Rotated / Horizontal).


Fig. 70: Bottom view of the pieces made with FFF (Vertical / Rotated / Horizontal).

A second attempt in 3D printing fabrication was made, this time, applying SLA (Stereolithography) techniques. This process consists on selectively illuminating a photopolymerizing liquid resin that interacts with the light, creating bonds and linking its molecules and thus solidifying. The 3D printer employed is the DW 020X from DWS Systems [81]. This machine offers an accuracy higher than the one offered by BW with FFF process, up to 10 microns, as announced on their webpage. However, the printer was not properly calibrated and an accuracy of a few hundreds of microns was achieved. The material used, from the same provider, was THERMA DM220, a nano-filled ceramic material whose main features are presented in [82]. Two approaches were made with this printer, as can be seen in Fig. 71 and Fig. 72. Both pieces were grown upside down, from the lower part of the base up to the bridge. The first approach was fabricated as a whole piece. Some pillars were needed in order to support the bridge, as well as the flange. The shape of these columns was that of a truncated cone, with a diameter of 0.4mm at the base, becoming thinner as they were grown. The lattice of this columns was set to 2 mm, the minimum value admitted. A smooth surface was achieved for the ellipsoidal cavity. However, the pillars under the bridge could

not be removed successfully and, as a consequence, the part of the ellipsoidal reflector situated right under the bridge was seriously damaged. On the other hand, the second approach did not include the bridge. It was left to be printed separately and assembled together with two pairs of alignment pins. In this case, it was observed that the ellipsoidal surface was reproduced accurately.

Fig. 71: Front view of the pieces made with SLA.

Fig. 72: Back view of the pieces made with SLA.

However, some minor problems were found in the area of the flange, due to some pillars that could not be removed. This fact motivated the idea of separating this part in the manufacturing process. The piece would be then fabricated in 3 parts: the bridge, the flange to support the horn, and the ellipsoidal cavity. This division allows a much easier fabrication process, which is believed to decrease the manufacturing errors. Moreover, it increases the versatility of the design, since the bridge and the flange can be designed individually, in case some modifications were needed. However, due to time constraints, no attempts have been made to fabricate the three parts

individually and assemble them. It could also be considered, if the accuracy of the SLA 3D printer is improved and the resulting piece is accurate enough, to metallize the 3D-printed piece. This would stand as a cost-saving process that could replace more expensive techniques such as direct machining. Nevertheless, direct machining is the proposed method for fabricating the final piece. The fabrication shall be made as proposed in this section: dividing the piece into different parts: bridge, flange support and ellipsoidal cavity. Figure sketches the model to be fabricated, colouring the different parts and including screws and alignment pins in order to assemble them properly. This alignment would be critical, since a misalignment could incur in a loss of efficiency due to the optical power not irradiating the photodiode completely or the horn not being placed properly at the second focus.

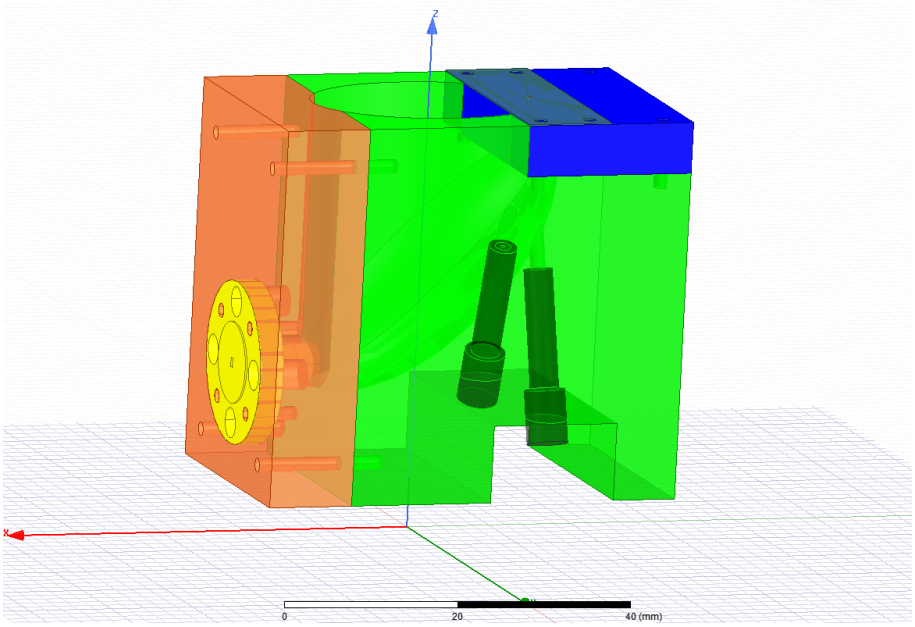


Fig. 73: Sketch of the machined model with coloured parts.

As for the substrate, no attempt has been made to fabricate it, since the photodiode was not available. Nevertheless, it is remarkable to note that it could be fabricated in the laboratory by means of photolithograpy and electron beam evaporation. This will be left as a future line of work.

# 9. Conclusions and future work

In this Master Thesis, a new integration and packaging technique for THz generation photomixers is presented.

This work has been developed in the framework of TERALINKS project, that has been presented and whose state of the art has been summarized. A review on the different techniques for generating THz radiation and the state of the art of the communication systems deployed at this frequency range have been presented in order to introduce the topic properly. Then, the basic theory concerning the ellipse has been explained, focusing on its fundamental property, which is that any beam coming out from one focus and intersecting the ellipse is redirected into the second focus.

This property has been corroborated using a full-wave simulation and, based on this concept, an ellipsoidal cavity has been designed, where the source of THz power, the photomixer, is placed in one of these foci and a horn antenna is placed at the second focus in order to collect this energy. For coupling the currents induced by the photomixer and thus generate THz radiation, different flat antennas have been designed.

A bridge structure has been designed to support the photomixer. This bridge contains a horn-shaped via that provides two main functionalities: allows direct irradiation of the photodiode and increases the amount of power that is directed to the ellipsoidal cavity.

In order to minimise the loss of power propagated across the substrate, some additional elements such as metallic rings and corrugations have been proposed, although they have not been studied.

In addition, an increase in this radiation has been observed by the inclusion of director elements and their performance have been evaluated.

As for the second focus, a choke horn antenna designed and measured at UPNA and manufactured by 3D printing techniques is proposed to collect the focalised energy. The results of the measurement campaign have been provided as well.

Front-side optical illumination of the photomixer is achieved by inserting the fibre collimators inside the cavity and incident directly through the horn-shaped via etched in the bridge. Commercial fibre collimators have been chosen for this purpose.

Some comments have been included regarding the manufacturing process. First attempts were made with 3D printing techniques, which illustrated how the piece could look like and allowed the detection of critical points, as well as to improve manufacturability of the design by separating the piece into different parts easier to fabricate individually. It was observed that SLA

printing provided significantly more accurate results than FFF 3D printing techniques.

When simulating the whole system, it was observed that the performance was not as good as expected. Nevertheless, it is believed that these approaches establish an interesting starting point for future studies and designs, and it can be agreed that some benchmarks have been validated. Future research on this topic is foreseen in the near future and is expected to obtain better results.

This work was strongly determined by the lack of information concerning the photomixer. For this reason, some adaptations of the model shall be made once this information is available. All in all, simulation results corroborate the feasibility of the proposed technique, demonstrate the proof of concept and establish some benchmarks for future designs. Once this information is known – such as the actual size of the photomixer, its impedance or the required spot size for optical illumination – and the model is redesigned, the manufacturing of the integration block will be feasible. This manufacturing could be realized by 3D printing and metallization techniques, if enough accuracy is provided by this first method. Otherwise, direct machining is proposed as the fabrication technique.

To the best knowledge of the author, this Master Thesis presents a novel concept for packaging and integration of THz-generating photomixers. Nevertheless, further work would be required in order to establish some benchmarks in the design of this kind of structures and several **future lines of work** could be drawn:

- The study of the dimensions of the ellipse and its eccentricity in order to obtain some benchmarks for an optimal design of the cavity.
- The study of different configurations including "shaping" on the surface of the reflector in order to compensate the phase distortion introduced. Other configurations could include two elliptical reflectors sharing a common focus in order to compensate the errors introduced.
- Further study of the position of the output antenna and the relation between the position of its phase centre and the focus. The same study shall be done to the position of the bridge and the phase centre of the horn etched in it.

Other minor lines of work to be investigated once the major limitations of the proposed structure are solved could involve:

- The study of the performance of different materials for the substrate, such as Topaz.
- Further study of the director elements, rings and corrugations.
- Manufacturing and measuring of the device.

# 10. Bibliography


[1] R. A. Lewis, "A review of terahertz sources," *J. Phys. D. Appl. Phys.*, vol. 47, no. 37, p. 374001, Sep. 2014.

[2] "TERALINKS — CHIST-ERA," 2015. [Online]. Available: http://www.chistera.eu/projects/teralinks. [Accessed: 23-Apr-2018].

[3] "ElectroDesign." [Online]. Available: http://www.electronicdesign.com/communications/millimeter-waves-will-expand-wireless-future. [Accessed: 10-Jun-2018].

[4] N. Bhushan *et al.*, "Network densification: the dominant theme for wireless evolution into 5G," *IEEE Commun. Mag.*, vol. 52, no. 2, pp. 82–89, Feb. 2014.

[5] X. Ge, H. Cheng, M. Guizani, and T. Han, "5G Wireless Backhaul Networks: Challenges and Research Advances," 2014.

[6] N. Sophia, G. Ducournau, and C. Luxey, "CHISTERA CALL - TMCS - TERAhertz high power LINKS using photonic devices , tube amplifiers and Smart antennas ( TERALINKS )," 2016.

[7] T. Nagatsuma and G. Carpintero, "Recent Progress and Future Prospect of Photonics-Enabled Terahertz Communications Research," no. 12, 2015.

[8] G. Ducournau *et al.*, "Ultrawide-Bandwidth Single-Channel 0.4-THz Wireless Link Combining Broadband Quasi-Optic Photomixer and Coherent Detection," *IEEE Trans. Terahertz Sci. Technol.*, vol. 4, no. 3, pp. 328–337, May 2014.

[9] X. Yu *et al.*, "160 Gbit/s photonics wireless transmission in the 300-500 GHz band," *Cit. APL Photonics*, vol. 1, no. 8, 2016.

[10] A. Hirata *et al.*, "120-GHz-Band Wireless Link Technologies for Outdoor 10-Gbit/s Data Transmission," *IEEE Trans. Microw. Theory Tech.*, vol. 60, no. 3, pp. 881–895, Mar. 2012.

[11] L. Daniel, D. Phippen, E. Hoare, A. Stove, M. Cherniakov, and M. Gashinova, "Low-THz Radar, Lidar and Optical Imaging through Artificially Generated Fog," in *International Conference on Radar Systems (Radar 2017)*, 2017.

[12] K. Humphreys *et al.*, "Medical applications of terahertz imaging: a review of current technology and potential applications in biomedical engineering," in *The 26th Annual International Conference of the IEEE Engineering in Medicine and Biology Society*, vol. 3, pp. 1302–1305.

[13] "Virginia Diodes, Inc - Detectors." [Online]. Available: https://www.vadiodes.com/en/products/detectors#zero-bias-detector.

[14] H. Jeffrey and C. Thomas W., "Responsivity and Noise Measurements of Zero-Bias Schottky Diode Detectors," *Semicond. Phys. Quantum Electron. Optoelectron.*, pp. 129–138, Jan. 2007.

[15] H. Motz, "Applications of the Radiation from Fast Electron Beams," *J. Appl. Phys.*, vol. 22, no. 5, pp. 527–535, May 1951.

[16] C. Pellegrini, "The history of X-ray free-electron lasers," *Eur. Phys. J. H*, vol. 37, no. 5, pp. 659–708, Oct. 2012.

[17] G. Ramian, "The new UCSB free-electron lasers," *Nucl. Instruments Methods Phys. Res. Sect. A Accel. Spectrometers, Detect. Assoc.*

*Equip.*, vol. 318, no. 1–3, pp. 225–229, Jul. 1992.

[18] "The UCSB Free Electron laser source — Materials Research Laboratory at UCSB: an NSF MRSEC." [Online]. Available: http://www.mrl.ucsb.edu/terahertz-facility/instruments/ucsb-free-electron-laser-source. [Accessed: 20-May-2018].

[19] G. Carpinero, E. Garcia-Munoz, H. Hartnagel, S. Preu, and A. Räisänen, *Semiconductor terahertz technology : devices and systems at room temperature operation*. 2015.

[20] H. Johnson, "Backward-Wave Oscillators," *Proc. IRE*, vol. 43, no. 6, pp. 684–697, 1955.

[21] E. B. Abubakirov, A. P. Konyushkov, and A. S. Sergeev, "Relativistic microvawe amplifier based on two backward-wave oscillators," in *2009 IEEE International Conference on Plasma Science - Abstracts*, 2009, pp. 1–1.

[22] L. Qing-Lun, W. Zi-Cheng, and L. Pu-Kun, "Simulation of the backward wave oscillator as a THz radiation source," in *2012 International Conference on Microwave and Millimeter Wave Technology (ICMMT)*, 2012, pp. 1–2.

[23] M. T. San, K. Ogura, K. Kubota, Y. Annaka, K. Yambe, and A. Sugawara, "Study on Operation of Oversized Backward Wave Oscillator for Broadband Terahertz Radiation," *IEEE Trans. Plasma Sci.*, vol. 46, no. 3, pp. 530–538, Mar. 2018.

[24] L. Gao, Y. Wang, Y. Hu, C. Paoloni, and B. Li, "Study of multiple beam backward wave oscillator based on corrugated waveguide TWT," in *2017 Eighteenth International Vacuum Electronics Conference (IVEC)*, 2017, pp. 1–2.

[25] S. Bhattacharjee *et al.*, "Folded Waveguide Traveling-Wave Tube Sources for Terahertz Radiation," *IEEE Trans. Plasma Sci.*, vol. 32, no. 3, pp. 1002–1014, Jun. 2004.

[26] C. Paoloni and M. Mineo, "0.22 THz TWT based on the double corrugated waveguide," in *IEEE International Vacuum Electronics Conference*, 2014, pp. 227–228.

[27] J.-S. Rieh, D. Yoon, and J. Yun, "An overview of solid-state electronic sources and detectors for Terahertz imaging," in *2014 12th IEEE International Conference on Solid-State and Integrated Circuit Technology (ICSICT)*, 2014, pp. 1–4.

[28] P. H. Siegel, "Terahertz technology," *IEEE Trans. Microw. Theory Tech.*, vol. 50, no. 3, pp. 910–928, Mar. 2002.

[29] E. Wasige, A. Al-Khalidi, K. Alharbi, and J. Wang, "High performance microstrip resonant tunneling diode oscillators as terahertz sources," in *2016 IEEE 9th UK-Europe-China Workshop on Millimetre Waves and Terahertz Technologies (UCMMT)*, 2016, pp. 25–28.

[30] K. Ishigaki, M. Shiraishi, S. Suzuki, M. Asada, N. Nishiyama, and S. Arai, "Direct intensity modulation and wireless data transmission characteristics of terahertz-oscillating resonant tunnelling diodes," *Electron. Lett.*, vol. 48, no. 10, p. 582, 2012.

[31] H. G. Yu, S. Jeon, S. H. Choi, and M. Kim, "300 GHz InP HBT amplifier with 10 mW output power," *Electron. Lett.*, vol. 50, no. 5, pp. 377–379, Feb. 2014.

[32] L. A. Samoska, "An Overview of Solid-State Integrated Circuit Amplifiers in the Submillimeter-Wave and THz Regime," *IEEE Trans. Terahertz Sci. Technol.*, vol. 1, no. 1, pp. 9–24, Sep. 2011.

[33] T. Bryllert, A. Malko, J. Vukusic, and J. Stake, "A 175 GHz HBV Frequency Quintupler With 60 mW Output Power," *IEEE Microw. Wirel. Components Lett.*, vol. 22, no. 2, pp. 76–78, Feb. 2012.

[34] J. Stake, A. Malko, T. Bryllert, and J. Vukusic, "Status and Prospects of High-Power Heterostructure Barrier Varactor Frequency Multipliers," *Proc. IEEE*, vol. 105, no. 6, pp. 1008–1019, Jun. 2017.

[35] I. Mehdi, J. V. Siles, C. Lee, and E. Schlecht, "THz Diode Technology: Status, Prospects, and Applications," *Proc. IEEE*, vol. 105, no. 6, pp. 990–1007, Jun. 2017.

[36] Qun Xiao, J. L. Hesler, Yiwei Duan, T. W. Crowe, and R. M. Weikle, "A 300-GHz Heterostructure Barrier Varactor (HBV) Frequency Septupler," in *2005 Joint 30th International Conference on Infrared and Millimeter Waves and 13th International Conference on Terahertz Electronics*, vol. 1, pp. 80–81.

[37] J. Stake, T. Bryllert, J. Vukusic, and A. Ø. Olsen, "Development of high power HBV multipliers for millimeter wave applications," 2007, vol. 6739, p. 67390U.

[38] B. T. Bulcha, J. L. Hesler, V. Drakinskiy, J. Stake, and N. S. Barker, "1.9-3.2 THz Schottky based harmonic mixer design and characterization," in *2015 European Microwave Conference (EuMC)*, 2015, pp. 837–840.

[39] T. Waliwander, M. Fehilly, and E. O'Brien, "An ultra-high efficiency high power Schottky varactor frequency doubler to 180–200 GHz," in *2016 Global Symposium on Millimeter Waves (GSMM) & ESA Workshop on Millimetre-Wave Technology and Applications*, 2016, pp. 1–4.

[40] N. Alijabbari, M. F. Bauwens, and R. M. Weikle, "160 GHz Balanced Frequency Quadruplers Based on Quasi-Vertical Schottky Varactors Integrated on Micromachined Silicon," *IEEE Trans. Terahertz Sci. Technol.*, vol. 4, no. 6, pp. 678–685, Nov. 2014.

[41] K. Fujita, M. Hitaka, A. Ito, M. Yamanishi, T. Dougakiuchi, and T. Edamura, "High-performance, ultra-broadband room-temperature terahertz quantum cascade laser sources," in *2016 41st International Conference on Infrared, Millimeter, and Terahertz waves (IRMMW-THz)*, 2016, pp. 1–2.

[42] H. Yasuda, "Choice of semiconductor material for high-temperature operation of terahertz quantum cascade laser," in *2012 37th International Conference on Infrared, Millimeter, and Terahertz Waves*, 2012, pp. 1–2.

[43] J. Zhu *et al.*, "Terahertz-frequency quantum cascade lasers with 1-Watt output power," 2014.

[44] A. Lyakh *et al.*, "3 W continuous-wave room temperature single-facet emission from quantum cascade lasers based on nonresonant extraction design approach," *Appl. Phys. Lett.*, vol. 95, no. 14, p. 141113, Oct. 2009.

[45] J. Niels Hovenier *et al.*, "The p-Ge terahertz laser-properties under

pulsed- and mode-locked operation," *IEEE Trans. Microw. Theory Tech.*, vol. 48, no. 4, pp. 670–676, Apr. 2000.

[46] A. Bergner *et al.*, "New p-Ge THz laser spectrometer for the study of solutions: THz absorption spectroscopy of water," *Rev. Sci. Instrum.*, vol. 76, no. 6, p. 063110, Jun. 2005.

[47] K. Sakai, *Terahertz optoelectronics*. Springer, 2005.

[48] C. Criollo and A. G. Avila, "Simulation of photoconductive antennas for terahertz radiation," *Ing. e Investig.*, vol. 35, no. 1, pp. 60–64, Mar. 2015.

[49] M. Weiß, M. Huchard, A. Stohr, B. Charbonnier, S. Fedderwitz, and D. S. Jager, "60-GHz Photonic Millimeter-Wave Link for Short- to Medium-Range Wireless Transmission Up to 12.5 Gb/s," *J. Light. Technol.*, vol. 26, no. 15, pp. 2424–2429, Aug. 2008.

[50] K. Balakier, M. J. Fice, L. Ponnampalam, A. J. Seeds, and C. C. Renaud, "Monolithically Integrated Optical Phase Lock Loop for Microwave Photonics," *J. Light. Technol.*, vol. 32, no. 20, pp. 3893–3900, Oct. 2014.

[51] I. Kostakis, D. Saeedkia, and M. Missous, "Terahertz Generation and Detection Using Low Temperature Grown InGaAs-InAlAs Photoconductive Antennas at 1.55 μm Pulse Excitation," *IEEE Trans. Terahertz Sci. Technol.*, vol. 2, no. 6, pp. 617–622, Nov. 2012.

[52] J. E. Bjarnason *et al.*, "ErAs:GaAs photomixer with two-decade tunability and 12μW peak output power," *Appl. Phys. Lett.*, vol. 85, no. 18, pp. 3983–3985, Nov. 2004.

[53] J. Mangeney, P. Crozat, A. Merigault, K. Blary, and J. F. Lampin, "CW generation up to 2 THz by ion-irradiated In0.53Ga0.47As photomixer driven at 1.55 μm wavelengths," in *2008 33rd International Conference on Infrared, Millimeter and Terahertz Waves*, 2008, pp. 1–2.

[54] E. Rouvalis, C. C. Renaud, D. G. Moodie, M. J. Robertson, and A. J. Seeds, "Continuous Wave Terahertz Generation From Ultra-Fast InP-Based Photodiodes," *IEEE Trans. Microw. Theory Tech.*, vol. 60, no. 3, pp. 509–517, Mar. 2012.

[55] H. Ito, F. Nakajima, T. Furuta, and T. Ishibashi, "Continuous THz-wave generation using antenna-integrated uni-travelling-carrier photodiodes," *Semicond. Sci. Technol.*, vol. 20, no. 7, pp. S191–S198, Jul. 2005.

[56] M. Natrella, E. Rouvalis, C.-P. Liu, H. Liu, C. C. Renaud, and A. J. Seeds, "InGaAsP-based uni-travelling carrier photodiode structure grown by solid source molecular beam epitaxy.," *Opt. Express*, vol. 20, no. 17, pp. 19279–88, Aug. 2012.

[57] G. Zhou *et al.*, "High-Power InP-Based Waveguide Integrated Modified Uni-Traveling-Carrier Photodiodes," *J. Light. Technol.*, vol. 35, no. 4, pp. 717–721, Feb. 2017.

[58] G. Ducournau *et al.*, "200 GHz coherent wireless link using photonics-based emission," in *2014 39th International Conference on Infrared, Millimeter, and Terahertz waves (IRMMW-THz)*, 2014, pp. 1–2.

[59] P. Latzel *et al.*, "Generation of mW Level in the 300-GHz Band Using Resonant-Cavity-Enhanced Unitraveling Carrier Photodiodes," *IEEE*

*Trans. Terahertz Sci. Technol.*, vol. 7, no. 6, pp. 800–807, Nov. 2017.

[60] A. Beck *et al.*, "High-efficiency uni-travelling-carrier photomixer at 1.55 μm and spectroscopy application up to 1.4 THz," *Electron. Lett.*, vol. 44, no. 22, p. 1320, 2008.

[61] V. K. Chinni *et al.*, "Single-channel 100 Gbit/s transmission using III–V UTC-PDs for future IEEE 802.15.3d wireless links in the 300 GHz band," *Electron. Lett.*, vol. 54, no. 10, pp. 638–640, May 2018.

[62] Q. Wu *et al.*, "A 21 km 5 Gbps real time wireless communication system at 0.14 THz," in *2017 42nd International Conference on Infrared, Millimeter, and Terahertz Waves (IRMMW-THz)*, 2017, pp. 1–2.

[63] T. Kosugi *et al.*, "A 120-GHz millimeter-wave MMIC chipset for future broadband wireless access applications," in *IEEE MTT-S International Microwave Symposium Digest, 2003*, vol. 1, pp. 129–132.

[64] G. Carpintero *et al.*, "Towards a common integration platform for photonics and electronics. Challenges for assembly and packaging," in *2016 IEEE CPMT Symposium Japan (ICSJ)*, 2016, pp. 115–117.

[65] F. Gaufillet, S. Marcellin, and E. Akmansoy, "Dielectric metamaterial-based gradient index lens in the terahertz frequency range," in *2017 11th International Congress on Engineered Materials Platforms for Novel Wave Phenomena (Metamaterials)*, 2017, pp. 7–9.

[66] J. Dai, J. Zhang, W. Zhang, and D. Grischkowsky, "Terahertz time-domain spectroscopy characterization of the far-infrared absorption and index of refraction of high-resistivity, float-zone silicon," *J. Opt. Soc. Am. B*, vol. 21, no. 7, p. 1379, Jul. 2004.

[67] A. Brahm, S. Doring, A. Wilms, G. Notni, S. Nolte, and A. Tunnermann, "Laser-generated broadband antireflection structures for freeform silicon lenses at terahertz frequencies," in *2014 39th International Conference on Infrared, Millimeter, and Terahertz waves (IRMMW-THz)*, 2014, pp. 1–2.

[68] M. Sun, Z. Chen, H. Tanoto, Q. Wu, J. Teng, and S. Yeap, "Design of continuous-wave photomixer driven terahertz dipole lens antennas," *APSIPA Annu. Summit Conf.*, pp. 14–17, 2010.

[69] I. Flammia, C. C. Leonhardt, J. Honecker, A. G. Steffan, and A. Stohr, "Novel E-Band (71–76 GHz) photodiode module featuring a hermetic grounded-coplanar-waveguide-to-rectangular-waveguide transition," in *2011 International Topical Meeting on Microwave Photonics jointly held with the 2011 Asia-Pacific Microwave Photonics Conference*, 2011, pp. 405–408.

[70] P. G. Huggard *et al.*, "Generation of millimetre and sub-millimetre waves by photomixing in 1.55 um wavelength photodiode," *Electron. Lett.*, vol. 38, no. 7, p. 327, 2002.

[71] X. Li, F. Ou, Z. Hou, Y. Huang, and S.-T. Ho, "Experimental Demonstration and Simulation of Lossless Metal-Free Integrated Elliptical Reflectors for Waveguide Turnings and Crossings," *CLEO2011 - Laser Appl. to Photonic Appl.*, p. JTuI26, 2011.

[72] J. A. Murphy and S. Withington, "Perturbation analysis of Gaussian-beam-mode scattering at off-axis ellipsoidal mirrors," *Infrared Phys. Technol.*, vol. 37, no. 2, pp. 205–219, Mar. 1996.

[73] M. Natrella *et al.*, "Modelling and measurement of the absolute level of power radiated by antenna integrated THz UTC photodiodes," *Opt. Express*, vol. 24, no. 11, p. 11793, May 2016.

[74] T. Wahyudi, C. Apriono, F. Y. Zulkifli, and E. T. Rahardjo, "Broadband planar bow-tie antenna on high resistivity silicon substrate for terahertz application," in *2017 15th International Conference on Quality in Research (QiR) : International Symposium on Electrical and Computer Engineering*, 2017, pp. 372–376.

[75] A. P. Aji, C. Apriono, F. Y. Zulkifli, and E. T. Rahardjo, "Radiation pattern validation of a THz planar bow-tie antenna at microwave domain by scaling up technique," in *2017 International Conference on Radar, Antenna, Microwave, Electronics, and Telecommunications (ICRAMET)*, 2017, pp. 108–111.

[76] Kiminami, Hirata, and Shiozawa, "Double-sided printed bow-tie antenna for UWB communications," *IEEE Antennas Wirel. Propag. Lett.*, vol. 3, pp. 152–153, 2004.

[77] H. G. Schantz and L. Fullerton, "The diamond dipole: a Gaussian impulse antenna," in *IEEE Antennas and Propagation Society International Symposium. 2001 Digest. Held in conjunction with: USNC/URSI National Radio Science Meeting (Cat. No.01CH37229)*, vol. 4, pp. 100–103.

[78] M. A. Sohaib, S. Bashir, S. ur Rehman, and F. Azam, "High gain microstrip yagi antenna for millimeter waves," in *2018 International Conference on Computing, Mathematics and Engineering Technologies (iCoMET)*, 2018, pp. 1–4.

[79] "GRIN Fiber Optic Collimators/Couplers, Single Mode Fiber." [Online]. Available: https://www.thorlabs.com/newgrouppage9.cfm?objectgroup˙id=1340. [Accessed: 16-May-2018].

[80] "BQ Witbox 2 Impresora 3D — BQ." [Online]. Available: https://www.bq.com/es/witbox-2. [Accessed: 12-Jun-2018].

[81] "DW 020X." [Online]. Available: https://www.dwssystems.com/3d-printers/industrial-design/DIGITALWAXff 020X. [Accessed: 12-Jun-2018].

[82] "DWS THERMA DM220." [Online]. Available: https://www.dwssystems.com/en/configurator/X/15/therma-dm220-ind-en. [Accessed: 12-Jun-2018].

[83] A. Yaghjian, "An overview of near-field antenna measurements," *IEEE Trans. Antennas Propag.*, vol. 34, no. 1, pp. 30–45, Jan. 1986.

[84] C. Taybi, M. A. Moutaouekkil, K. K. Rodrigues, B. Elmagroud, and A. Ziyyat, "Probes correction for planar near field antennas measurements," in *2015 IEEE 15th Mediterranean Microwave Symposium (MMS)*, 2015, pp. 1–4.

# Appendix 1 – Parametric analysis of the dimensions of the bridge

Three different parameters are swept in this analysis: the so-called internal or input radius of the horn-shaped via, its output radius and the length of the via (which is the thickness of the metallic bridge as well). Discrete values have been swept:

- Internal/Input radius was swept between 0.4mm and 1.5mm, with an interval of 0.1mm. Lower values were excluded because they were considered too small in comparison to the dipole. Analogously, higher values were excluded because they were considered too big.
- Output radius was swept between 1mm and 3mm, with an interval of 0.5mm.
- Thickness of the bridge was swept between 2mm and 6mm, with an interval of 1mm. It was believed that lower values would not offer remarkable directivities and higher values were considered too bulky.

Different colour maps are displayed next. For each value of the output radius, the relationship between the 2 other variables is shown in terms of

- Directivity in the direction of interest
- Backward directivity
- Difference of forward/backward directivities (front to back-lobe ratio).

Within each figure, the most remarkable combination of dimensions are highlighted by writing the values over their cells.

Output radius: 1mm

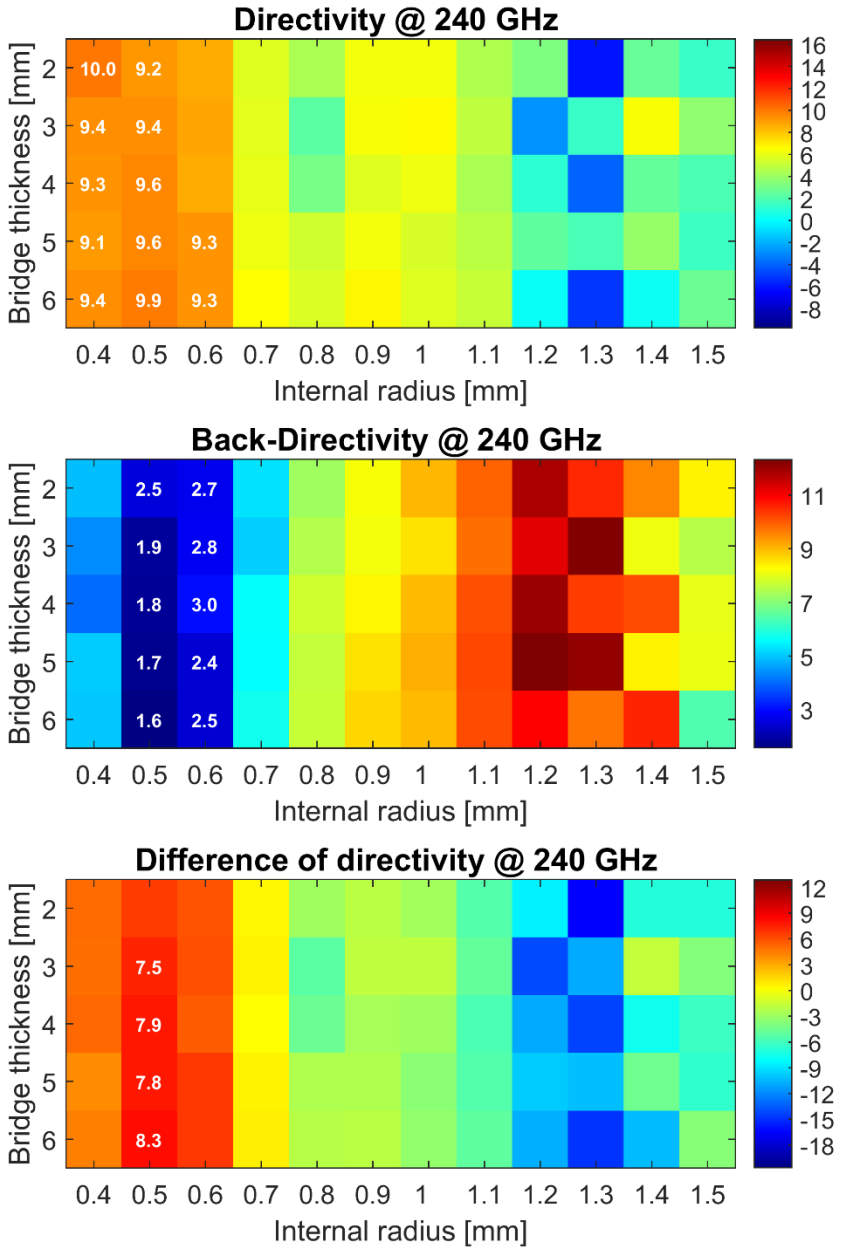


Fig. 74: Bridge with 1mm output radius

Output radius: 1.5mm

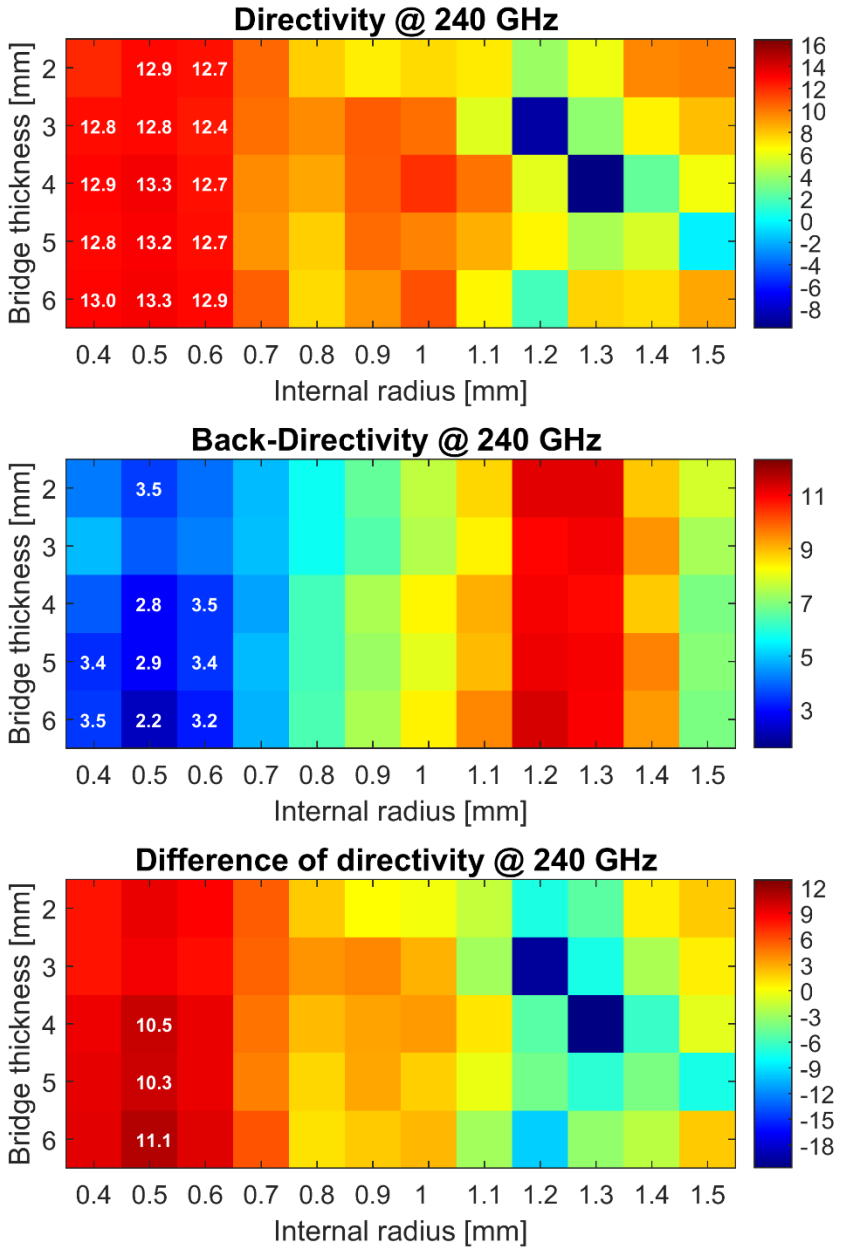


Fig. 75: Bridge with 1.5mm output radius

Output radius: 2mm

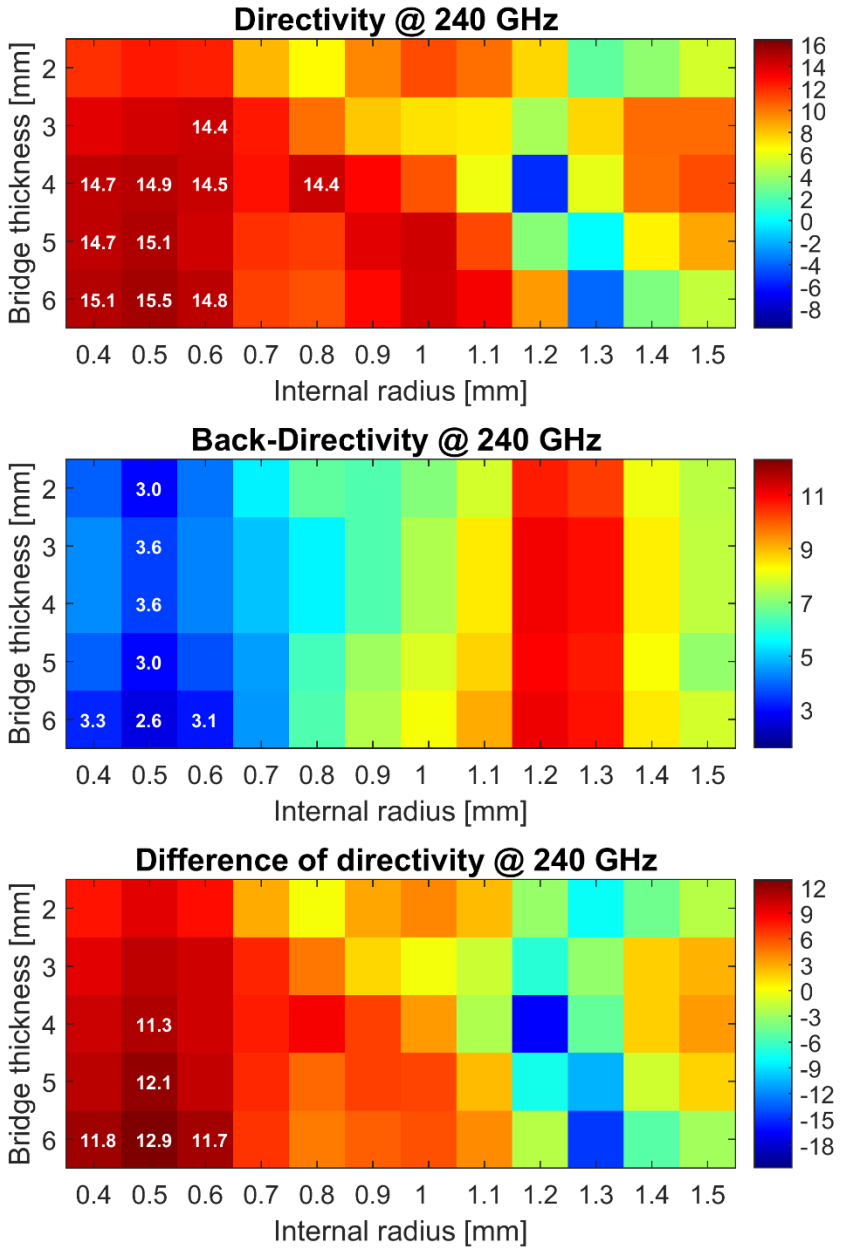


Fig. 76: Bridge with 2mm output radius

Output radius: 2.5mm

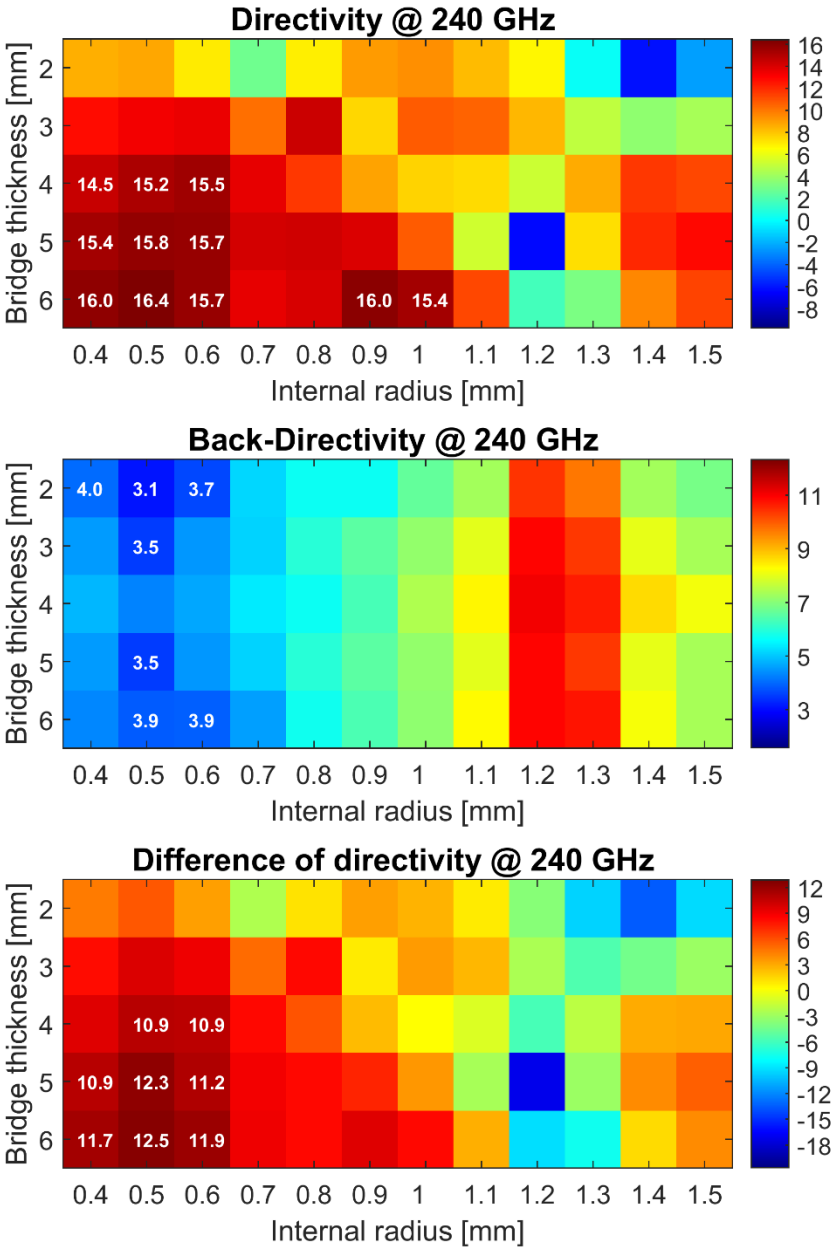


Fig. 77: Bridge with 2.5mm output radius

Output radius: 3mm

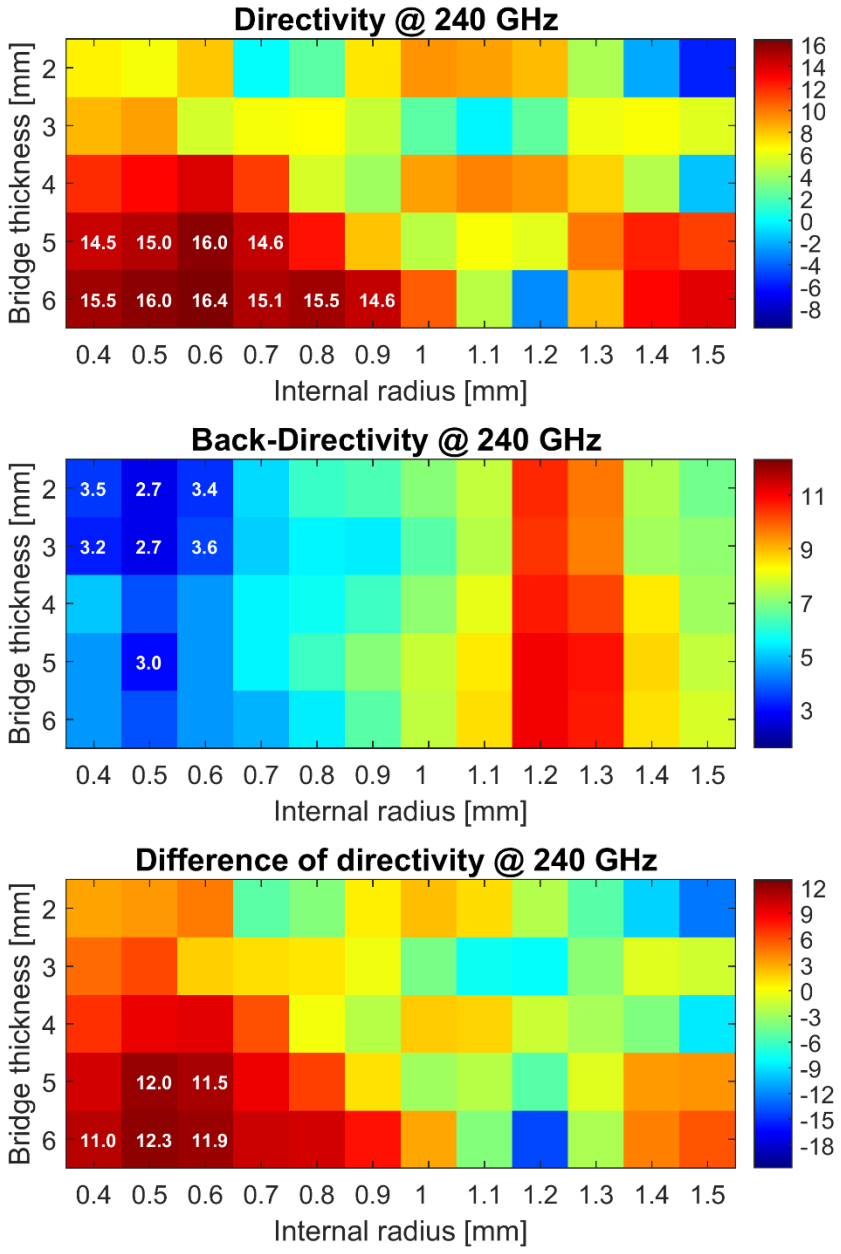


Fig. 78: Bridge with 3mm output radius

# Appendix 2 – Parametric analysis of the dimensions of the director elements

Three different parameters are swept in this analysis: the so-called director-offset, which refers to the distance, in the XY plane, from the inner edge of the director element to the vertical axis; frame width, which is the width of the metallic path that conforms the director element; and the width and length of the elements. Discrete values have been swept:

- Length and width of the directors: from 20% to 90% of the dipole size, 380μm x 270μm respectively.
- Directors' offset: from 25μm to 75μm, with an interval of 10 μm. The offset of 25μm corresponds to the offset of the elements of the dipole due to the input port.
- Directors' frame width, from 10μm to 30μm, with an interval of 10 μm. Lower frame widths have been excluded due to unavailability or high difficulty in a practical manufacturing process.

Different colour maps are displayed next. For each combination of the directors' offset and the frame width, the relationship between the 2 other variables is shown in terms of:

- Directivity in the direction of interest ($\theta = 180^\circ$)
- Backwards directivity (Since the maximum is not always located at $\theta$ =0, the maximum value of directivity in the range from 0 to $60^\circ$ has been considered)
- Difference of forward/backward directivities.

Within each figure, the most remarkable combination of dimensions are highlighted by writing the values over their cells. The values represented in these figures illustrate the difference of the obtained directivities with respect to the configuration without director elements (15.7 dB of directivity and 4.1 dB of back-directivity).

Frame width = 10 µm & Directors' offset = 25 µm

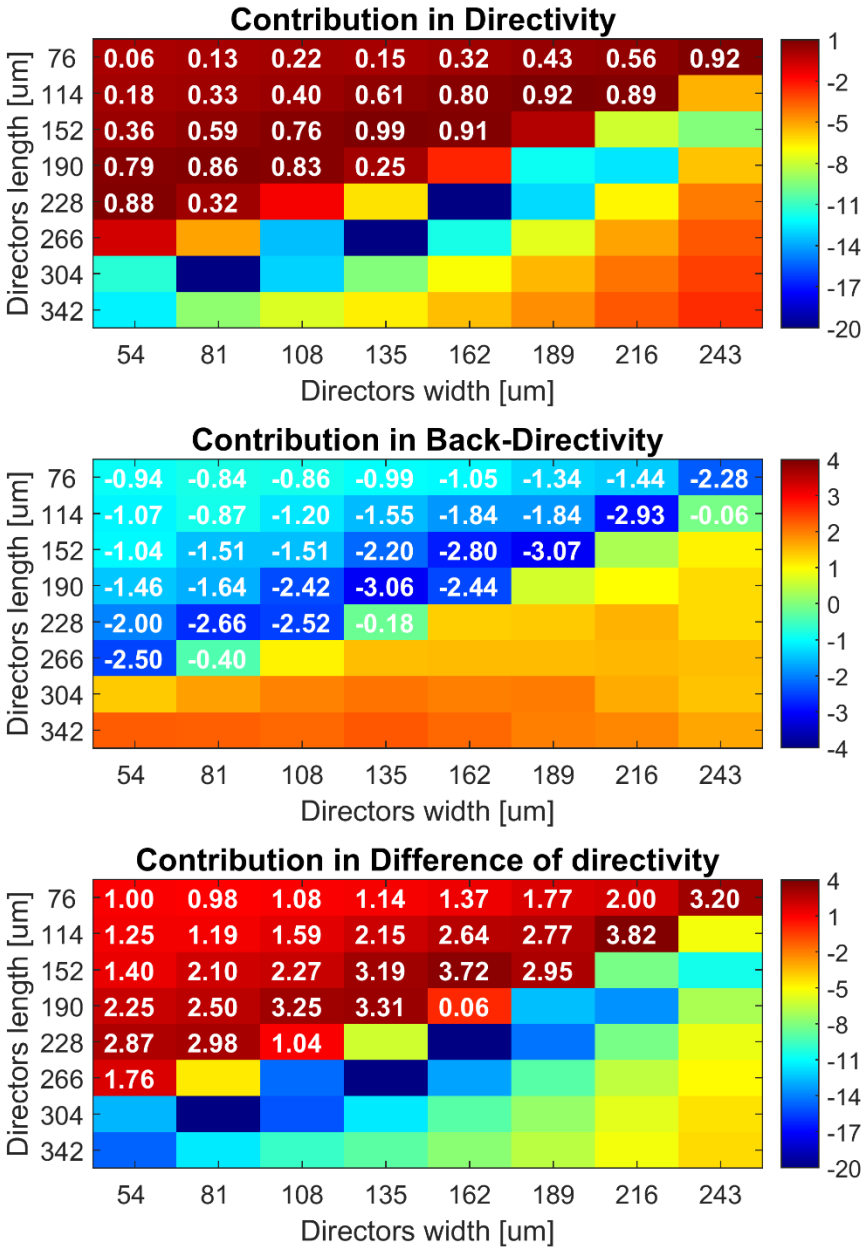


Fig. 79: Contribution to difference of directivities with 25 µm offset and 10 µm frame width

Frame width = 10 µm & Directors' offset = 35 µm

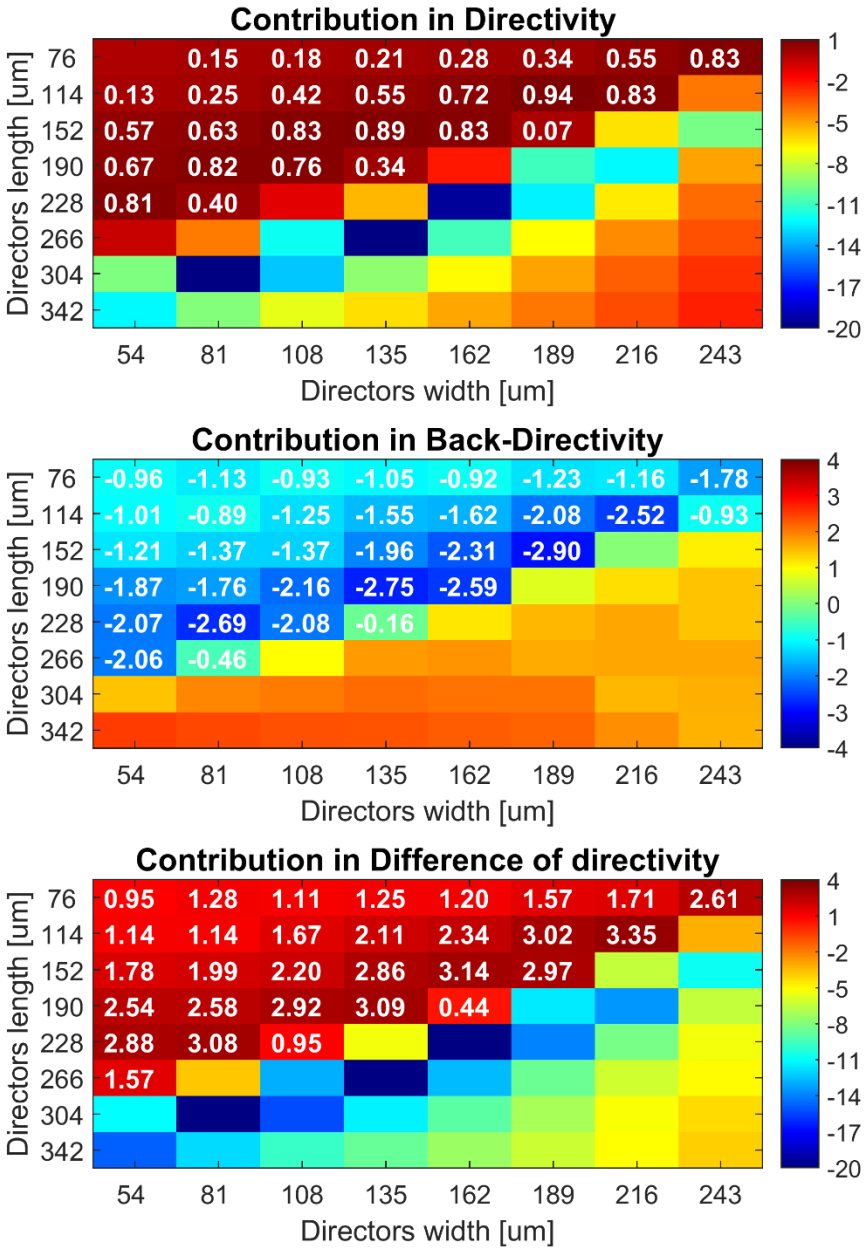


Fig. 80: Contribution to difference of directivities with 35 µm offset and 10 µm frame width

Frame width = 10 µm & Directors' offset = 45 µm

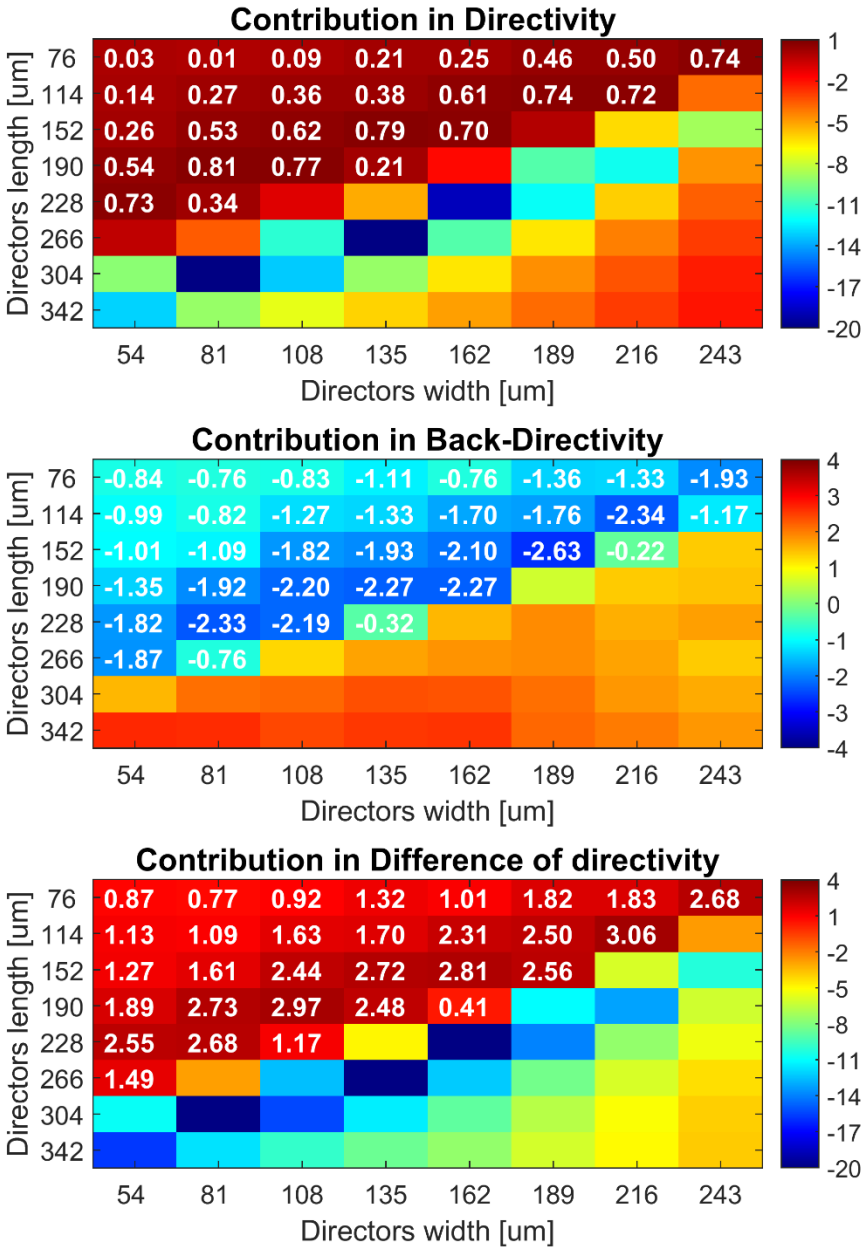


Fig. 81: Contribution of the director elements with 45 µm offset and 10 µm frame width

Frame width = 10 µm & Directors' offset = 55 µm

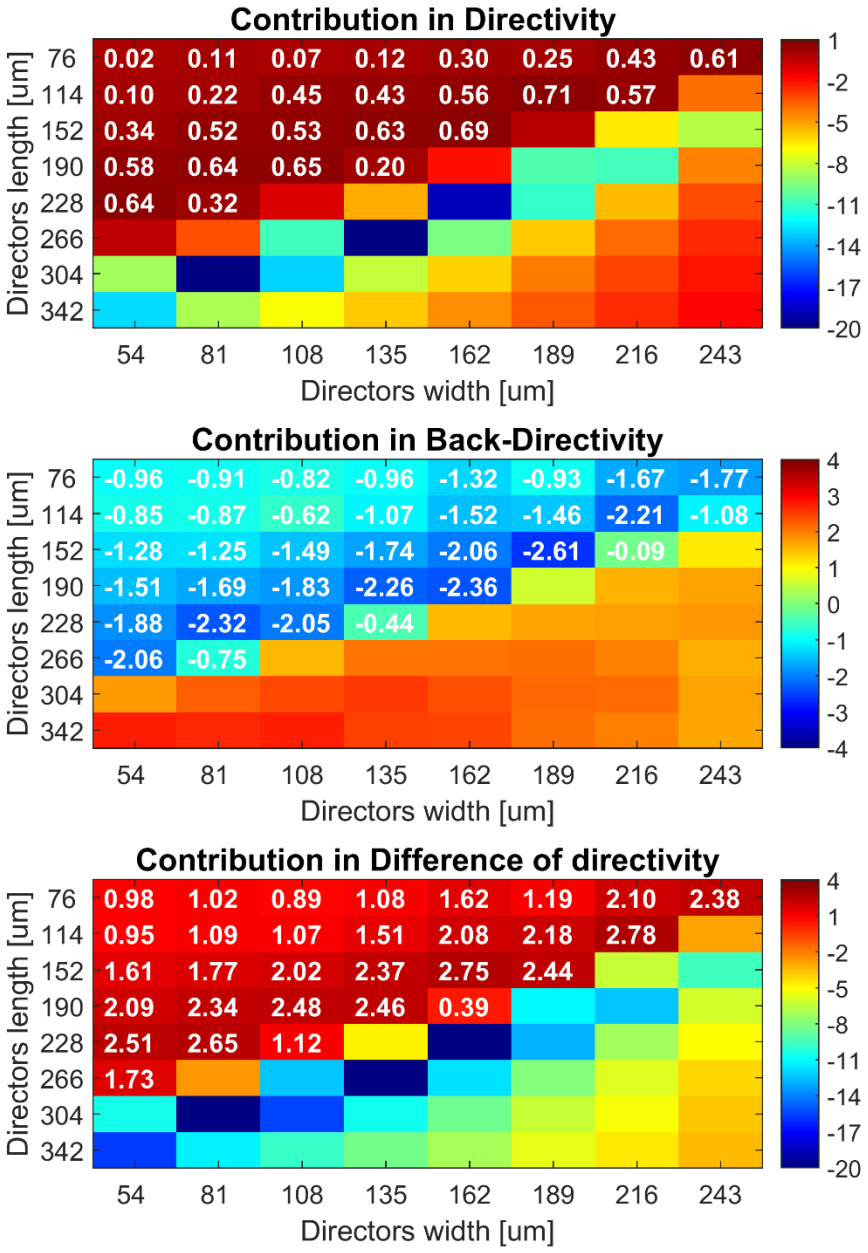


Fig. 82: Contribution of the director elements with 55 µm offset and 10 µm frame width

Frame width = 10 µm & Directors' offset = 65 µm

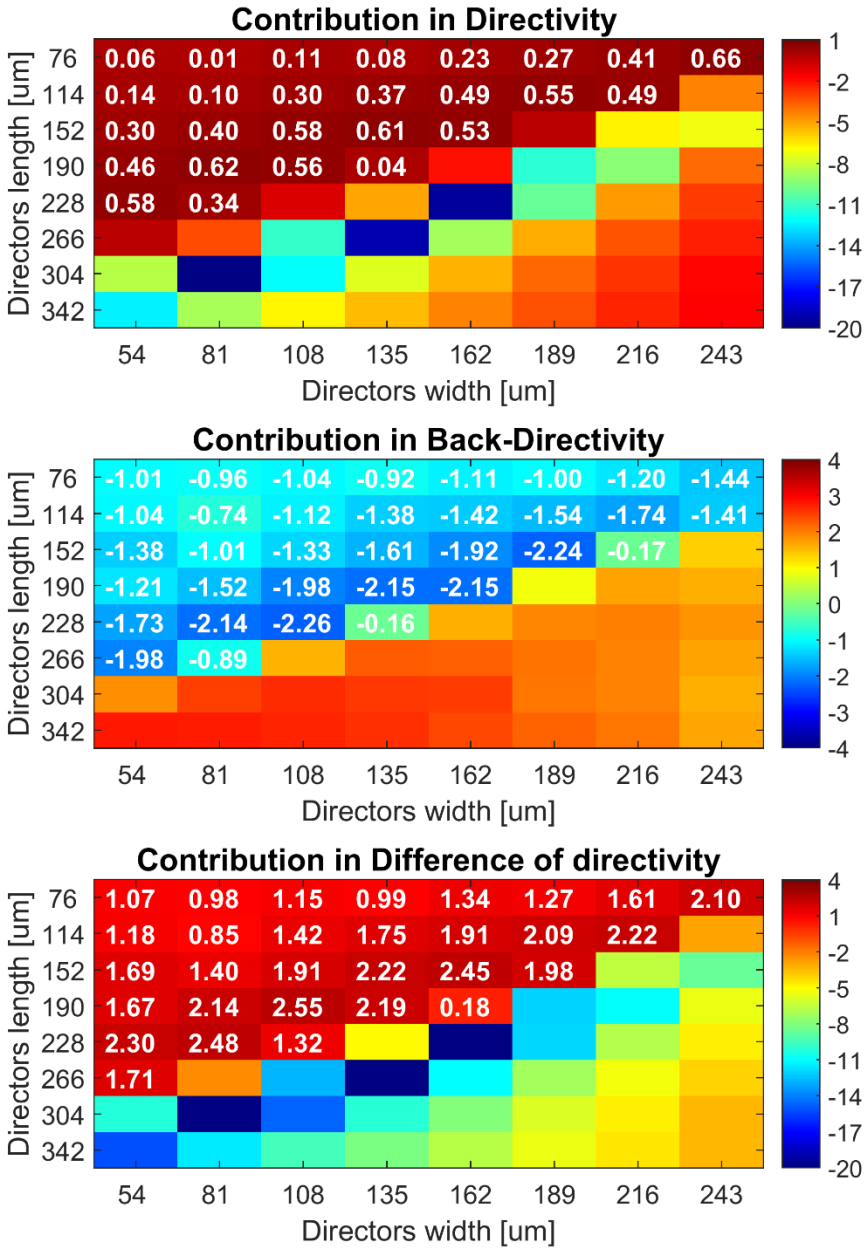


Fig. 83: Contribution of the director elements with 65 µm offset and 10 µm frame width

Frame width = 10 µm & Directors' offset = 75 µm

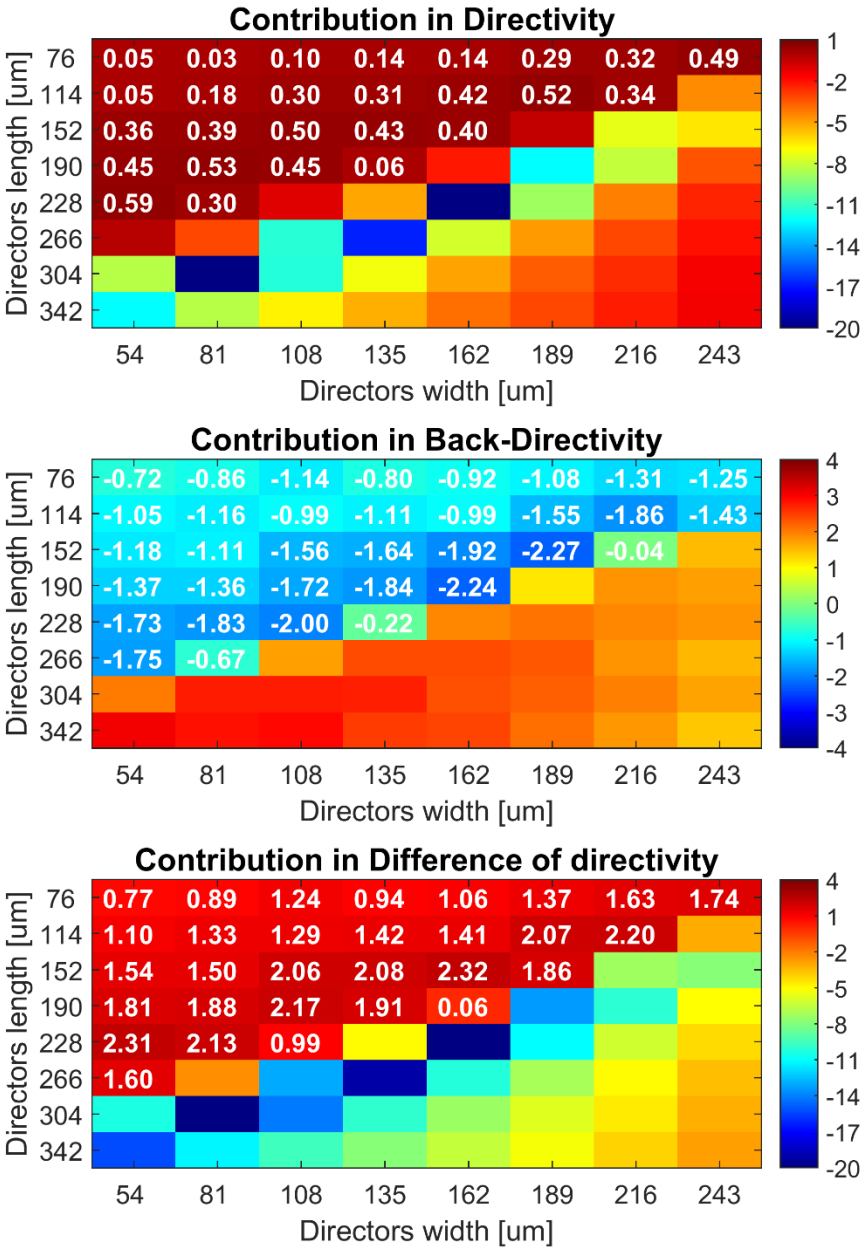


Fig. 84: Contribution of the director elements with 75 µm offset and 10 µm frame width

Frame width = 20 µm & Directors' offset = 25 µm

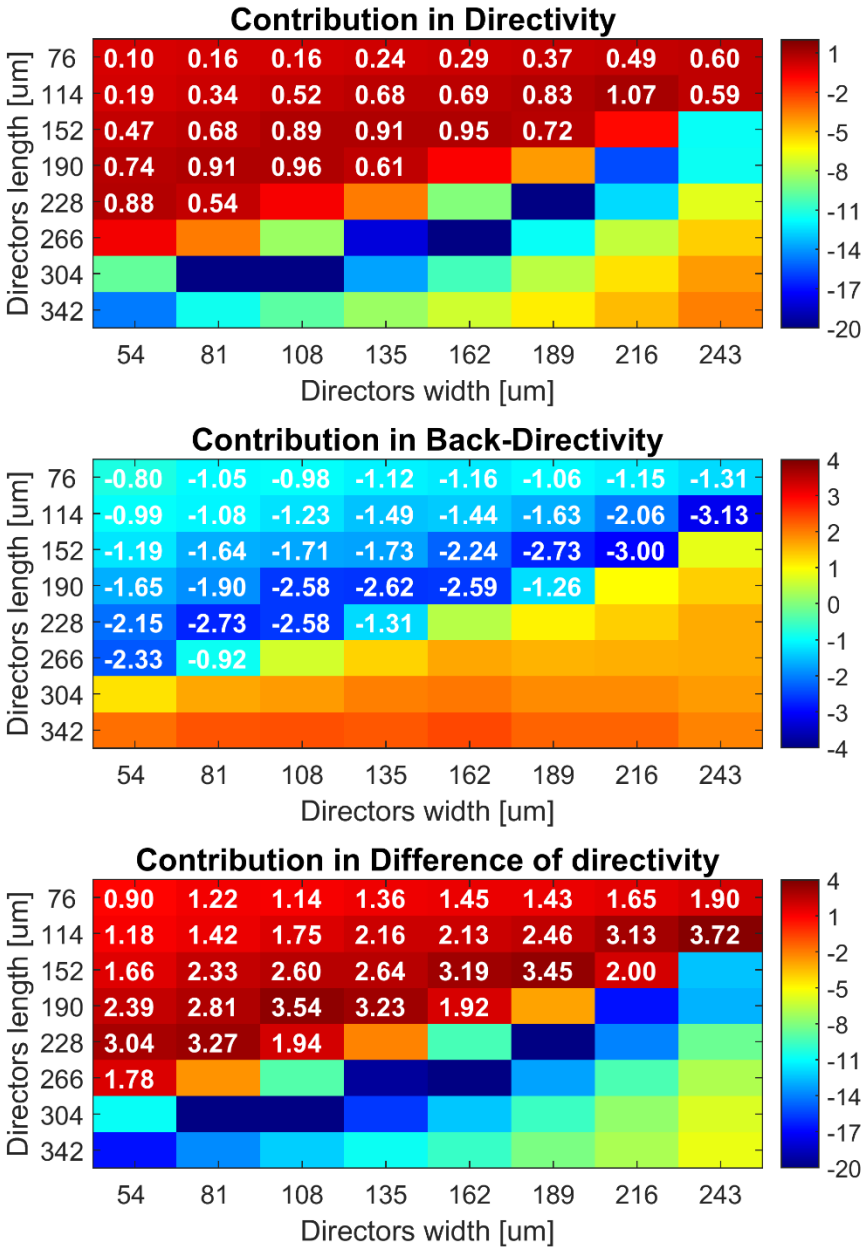


Fig. 85: Contribution of the director elements with 25 µm offset and 20 µm frame width

Frame width = 20 µm & Directors' offset = 35 µm

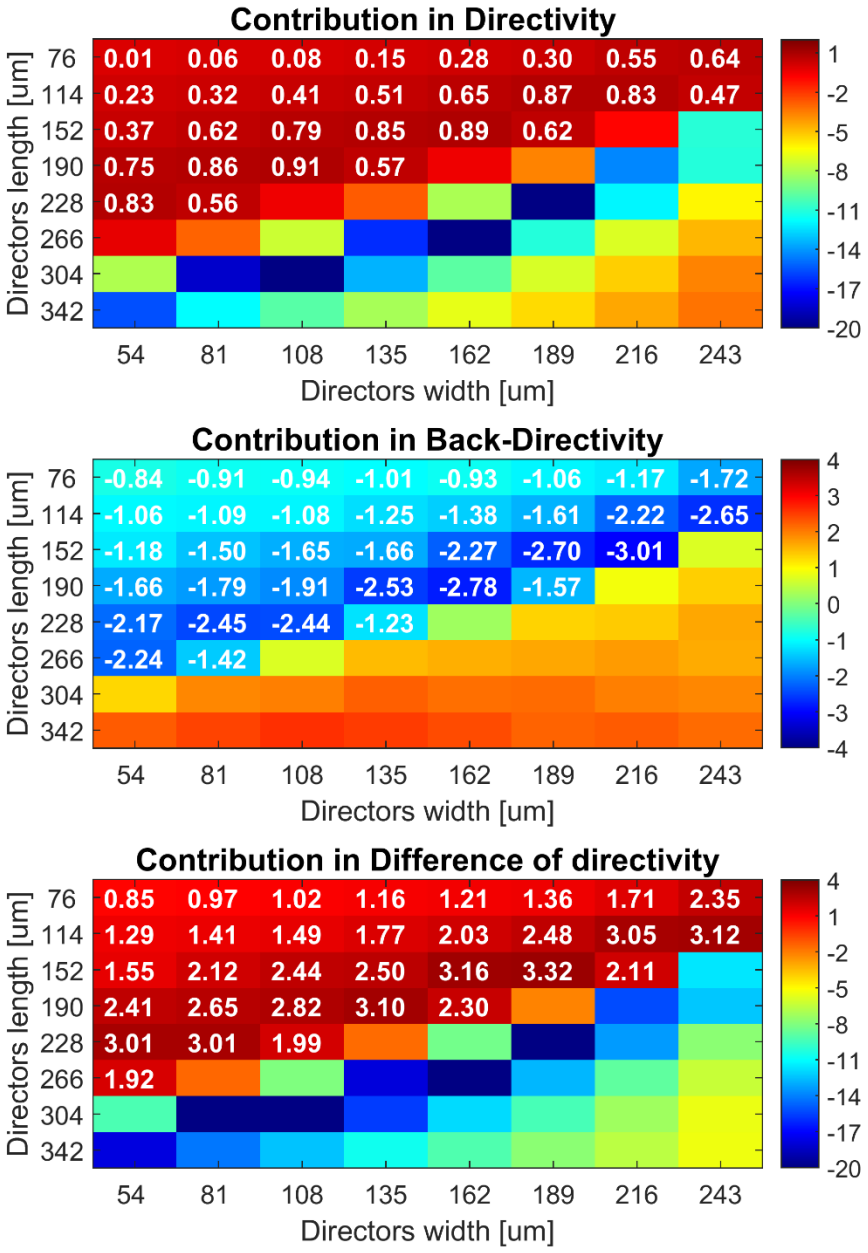


Fig. 86: Contribution of the director elements with 35 µm offset and 20 µm frame width

Frame width = 20 µm & Directors' offset = 45 µm

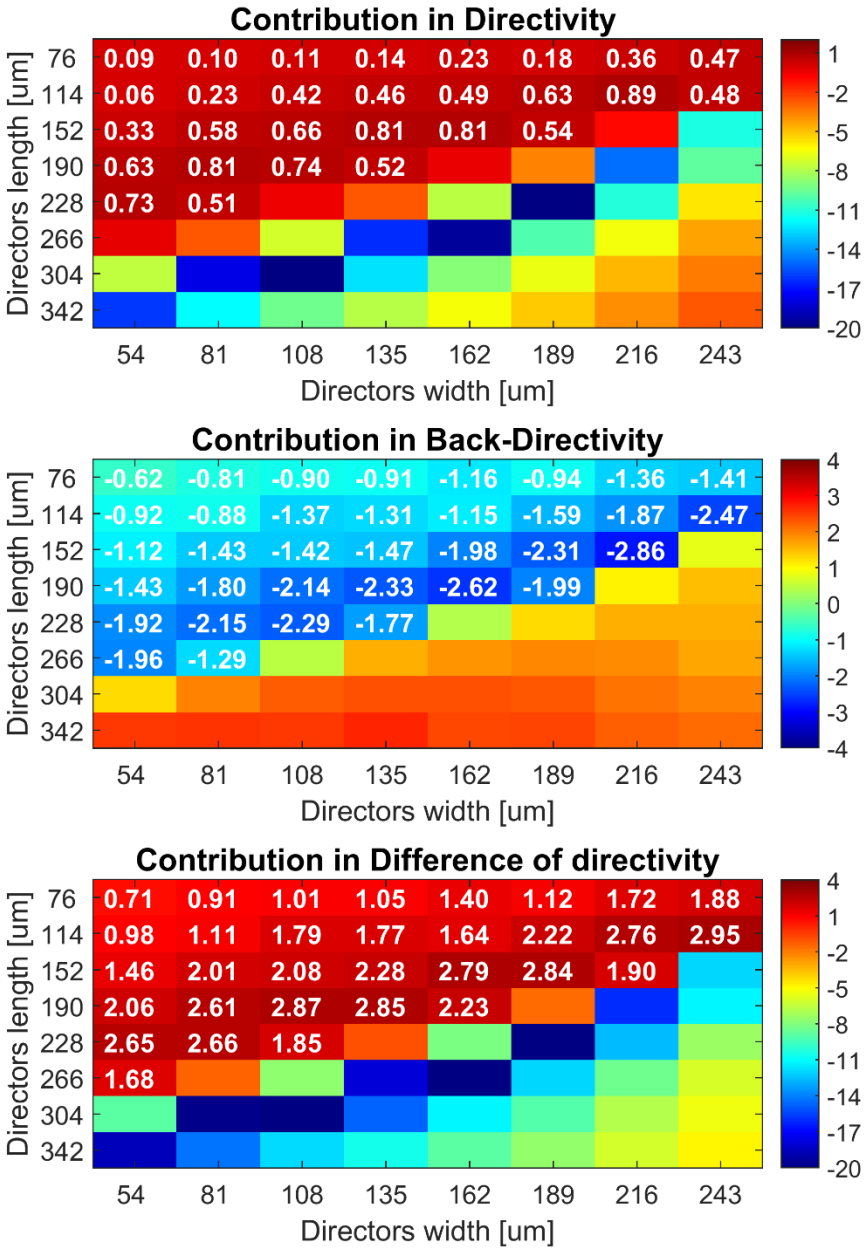


Fig. 87: Contribution of the director elements with 45 µm offset and 20 µm frame width

Frame width = 20 µm & Directors' offset = 55 µm

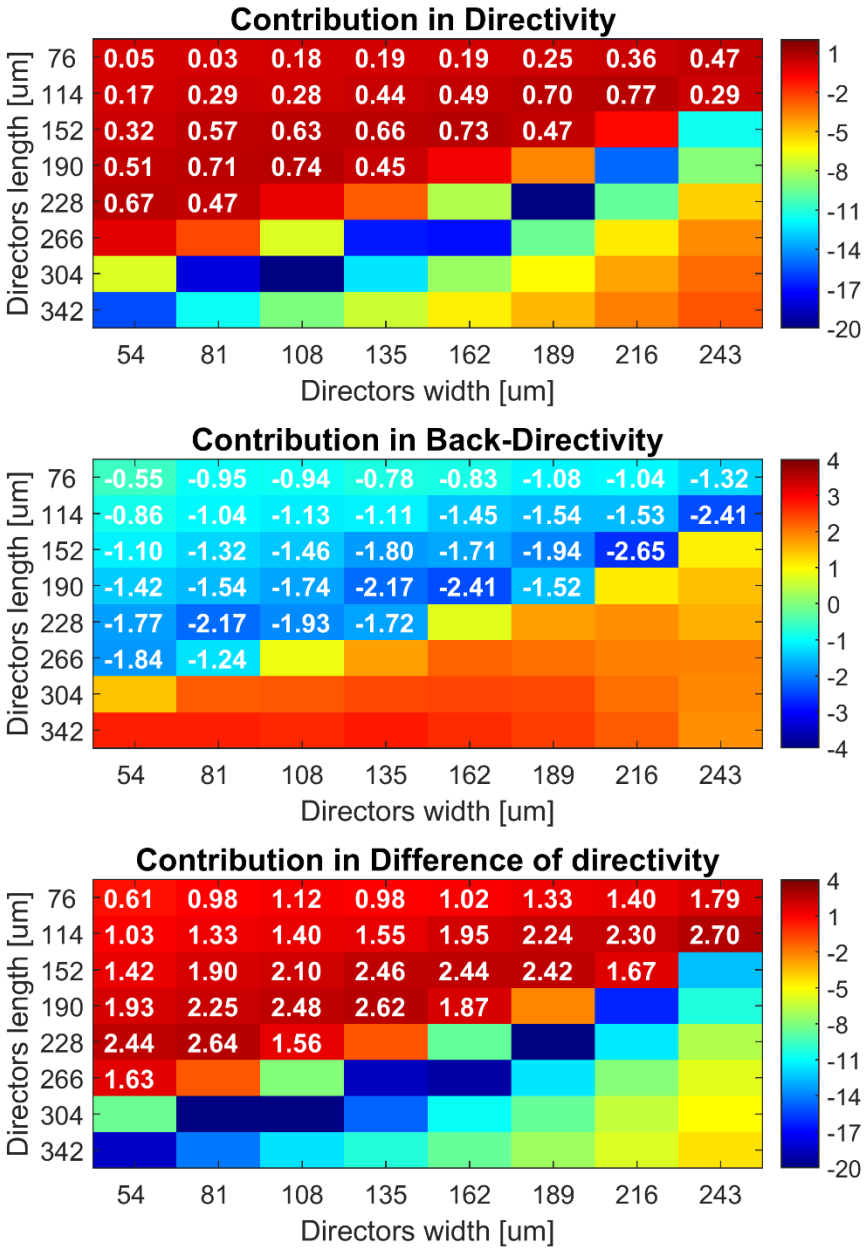


Fig. 88: Contribution of the director elements with 55 µm offset and 20 µm frame width

Frame width = 20 µm & Directors' offset = 65 µm

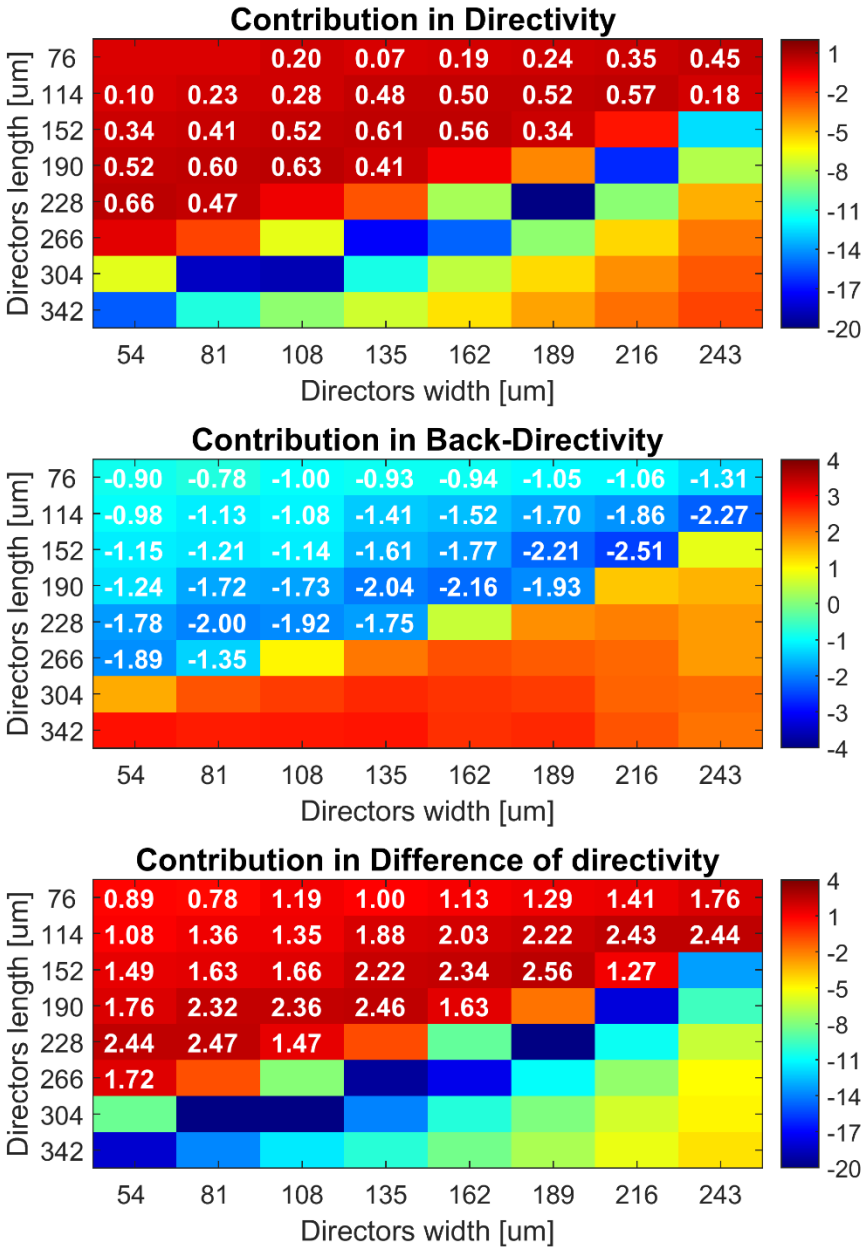


Fig. 89: Contribution of the director elements with 65 µm offset and 20 µm frame width

Frame width = 20 µm & Directors' offset = 75 µm

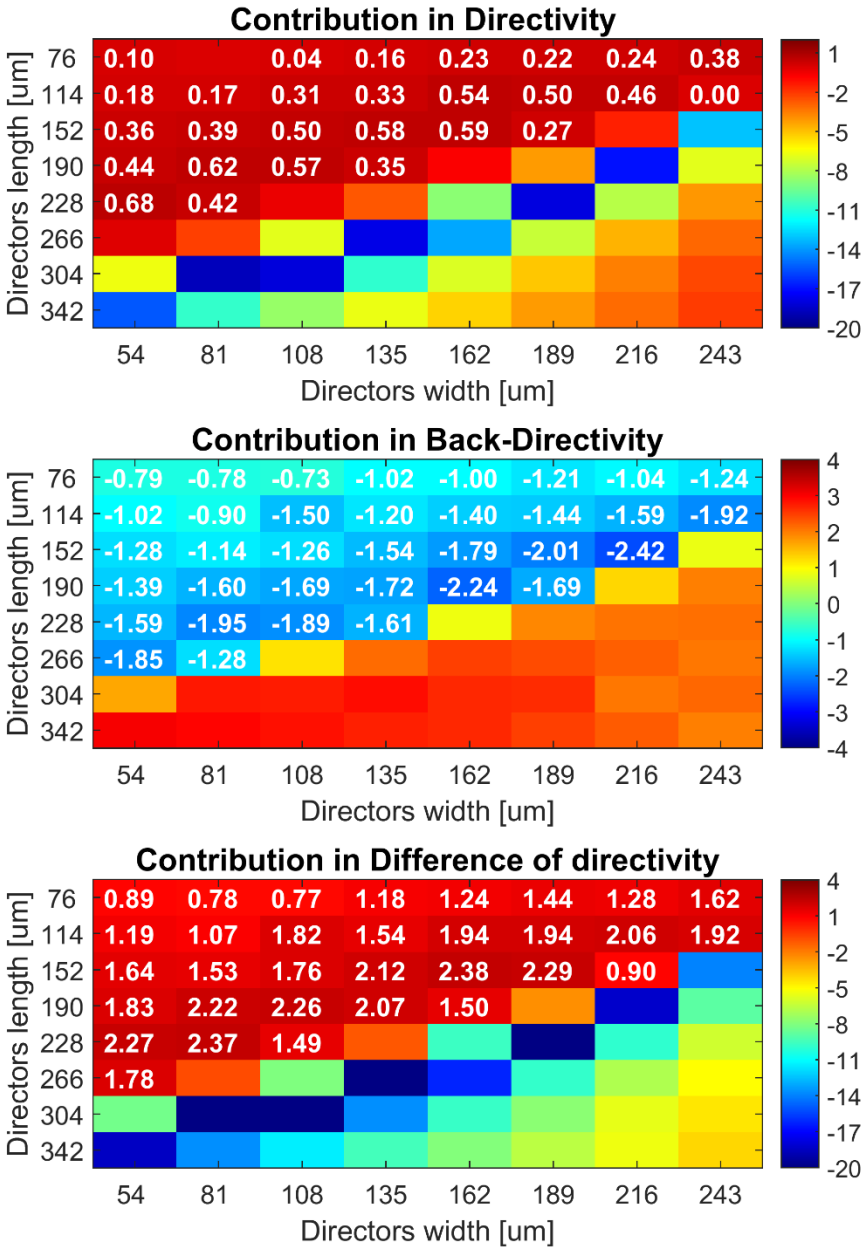


Fig. 90: Contribution of the director elements with 75 µm offset and 20 µm frame width

Frame width = 30 µm & Directors' offset = 25 µm

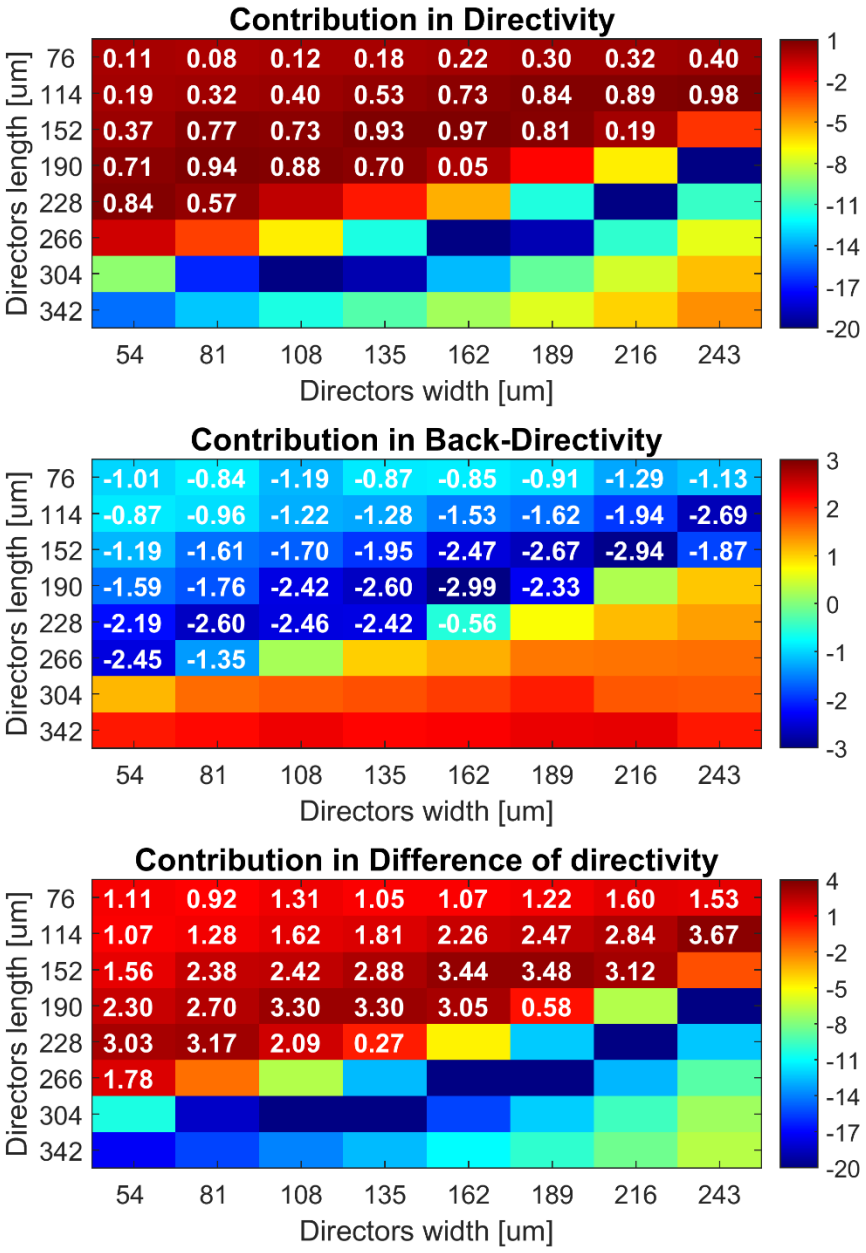


Fig. 91: Contribution of the director elements with 25 µm offset and 30 µm frame width

Frame width = 30 µm & Directors' offset = 35 µm

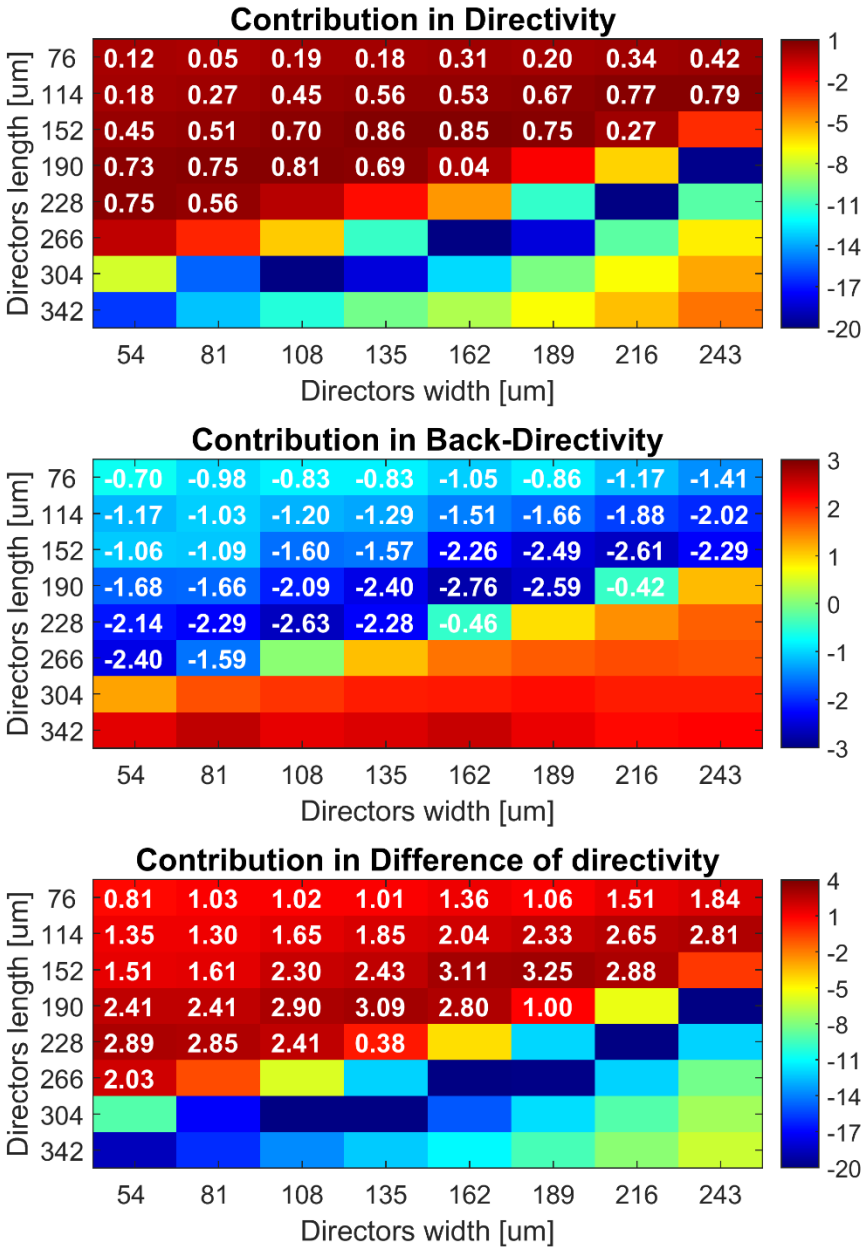


Fig. 92: Contribution of the director elements with 35 µm offset and 30 µm frame width

Frame width = 30 µm & Directors' offset = 45 µm

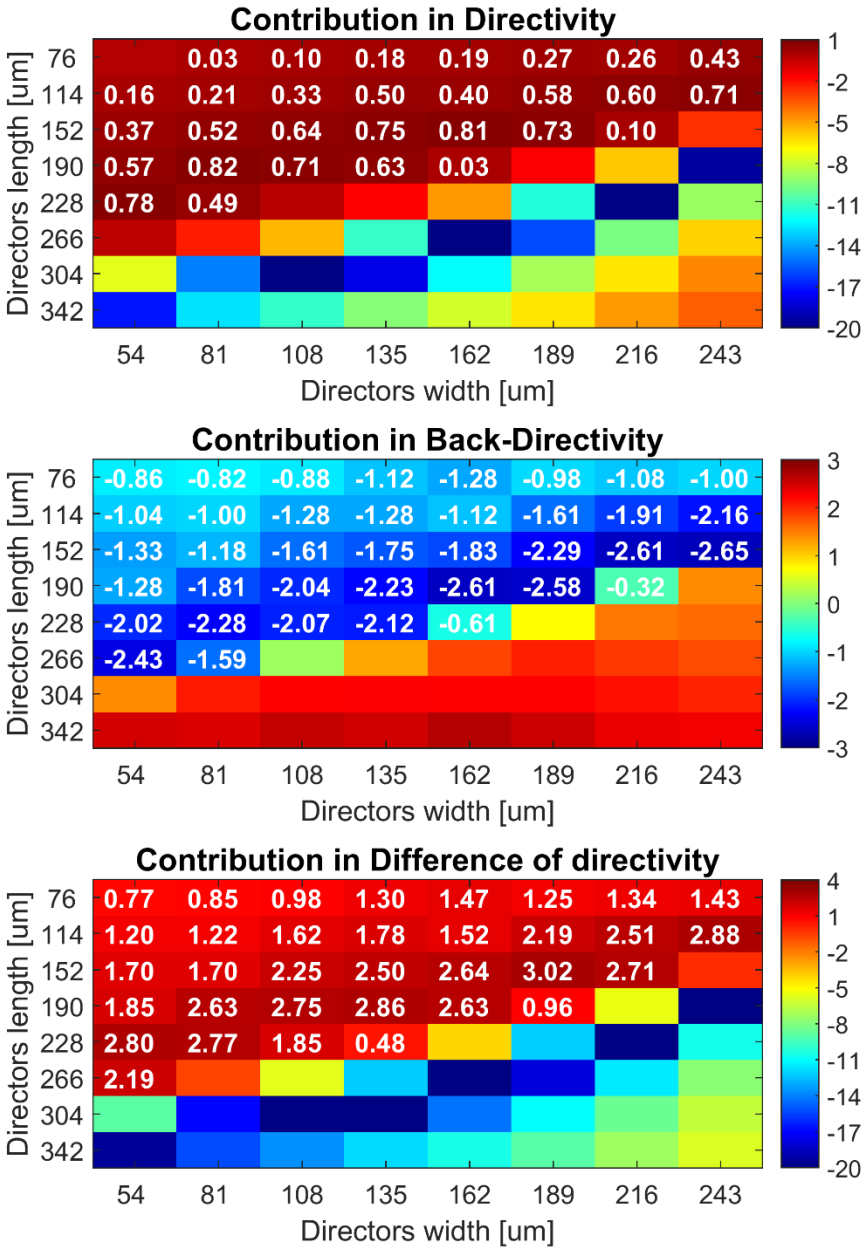


Fig. 93: Contribution of the director elements with 45 µm offset and 30 µm frame width

Frame width = 30 µm & Directors' offset = 55 µm

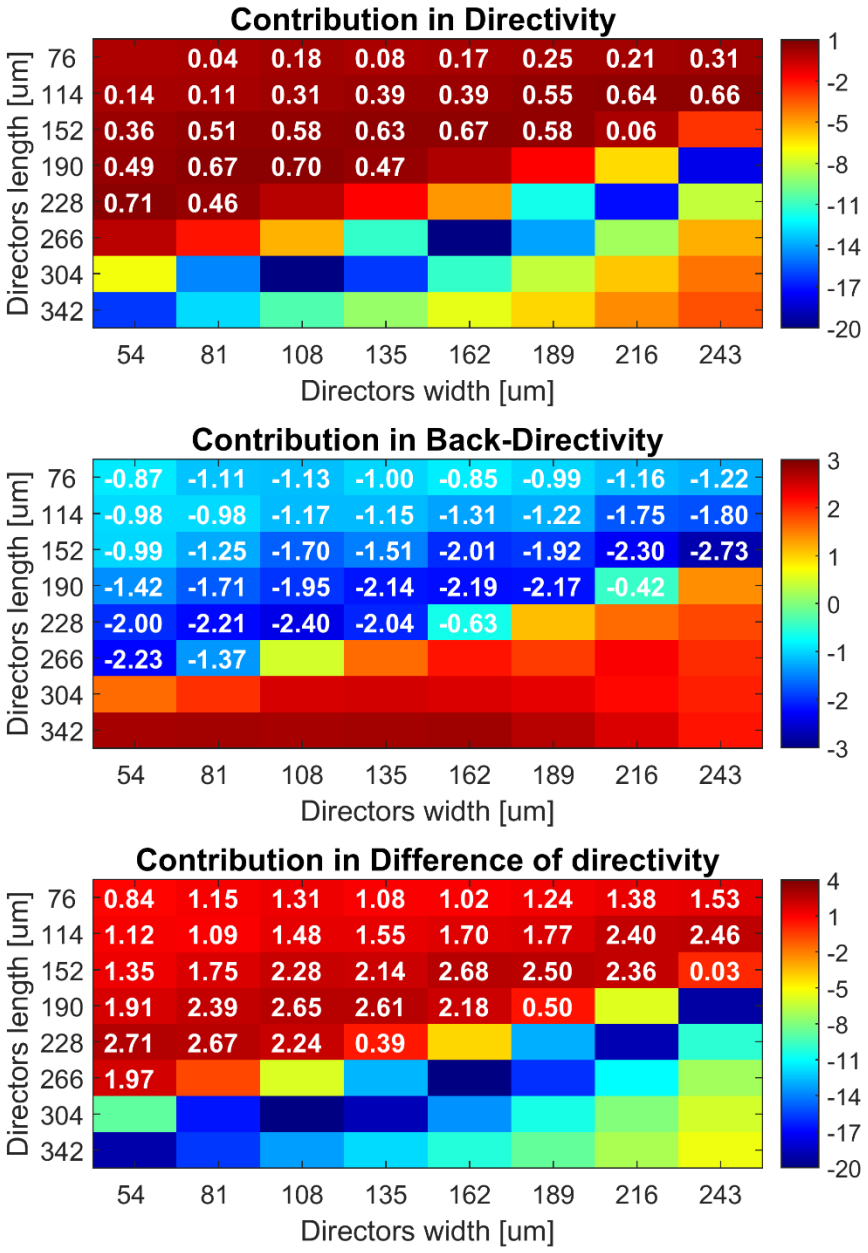


Fig. 94: Contribution of the director elements with 55 µm offset and 30 µm frame width

Frame width = 30 µm & Directors' offset = 65 µm

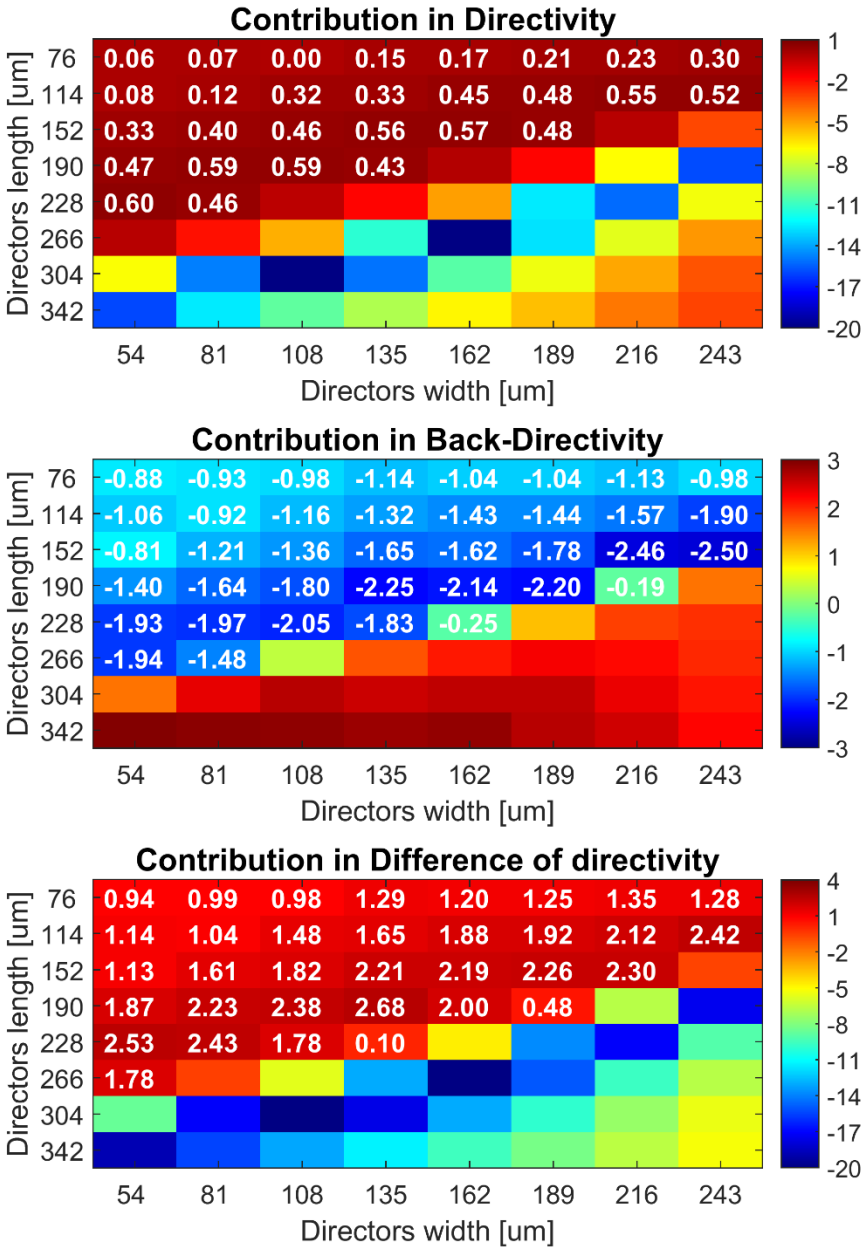


Fig. 95: Contribution of the director elements with 65 µm offset and 30 µm frame width

Frame width = 30 µm & Directors' offset = 75 µm

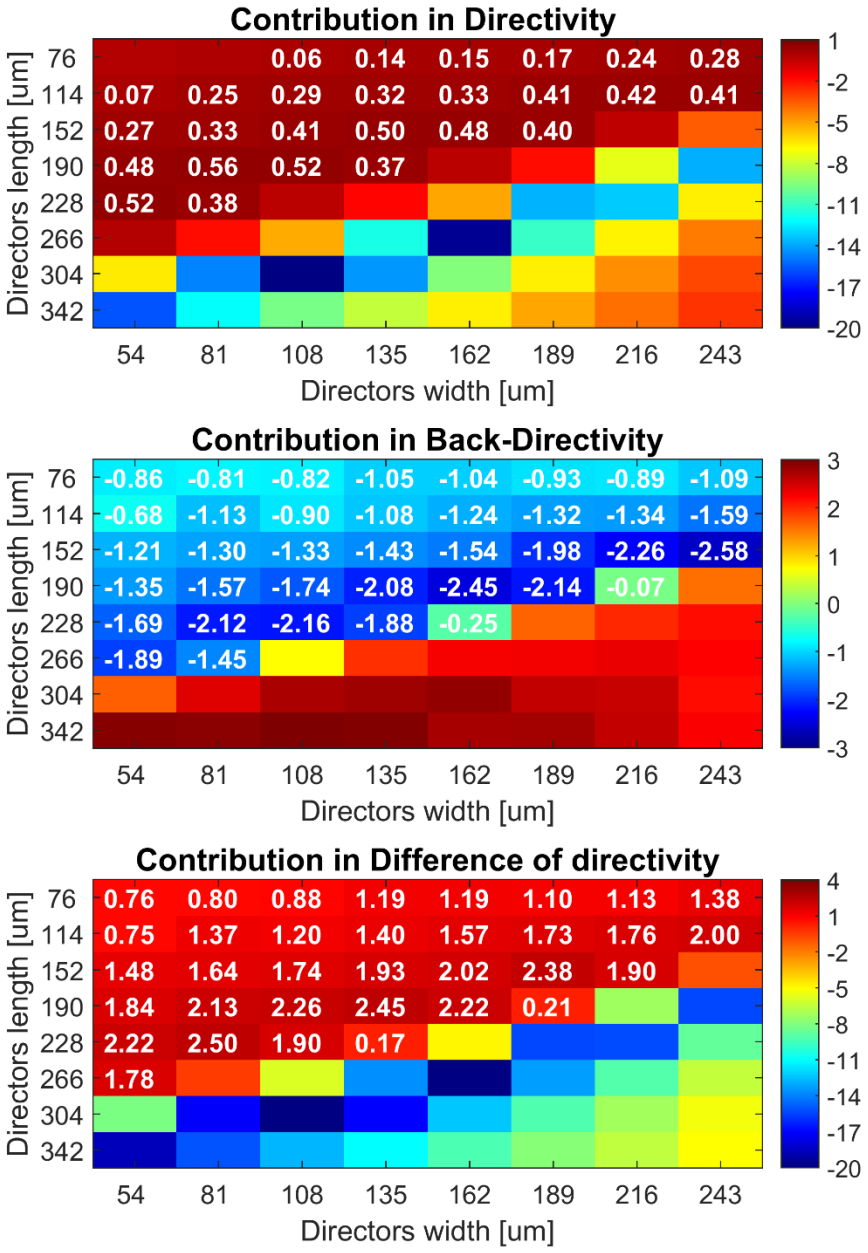


Fig. 96: Contribution of the director elements with 75 µm offset and 30 µm frame width

# Appendix 3 – Far-Field and Near-Field measuring campaign of the choke horn

The measurement of the choke horn antenna was performed at the Terahertz Laboratory, in Jeronimo de Ayanz Building, at UPNA. For the measurements an Agilent PNA-X N5242A Vector Analyser measuring system (26.5 GHz) and VDI external mixers, for the 220-330 GHz frequency band in WR3.4 standard waveguide, have been used.

Antenna measurements have been performed in both Far-Field and Planar Near-Field procedures. Both measurements were realised using the same set-up, shown in Fig. 97, consisting of a planar X-Y table, two polarization rotors, $\theta_1$ and $\theta_2$, and one azimuthal rotor, $\phi_1$. The far field pattern was obtained for a fixed X-Y position, measuring different cuts combining the three rotors. The planar near field measurement was performed by moving the measuring probe within the X-Y table, fixing the position of the rotors. All the measuring process is controlled with a LabVIEW script that was available at the laboratory.

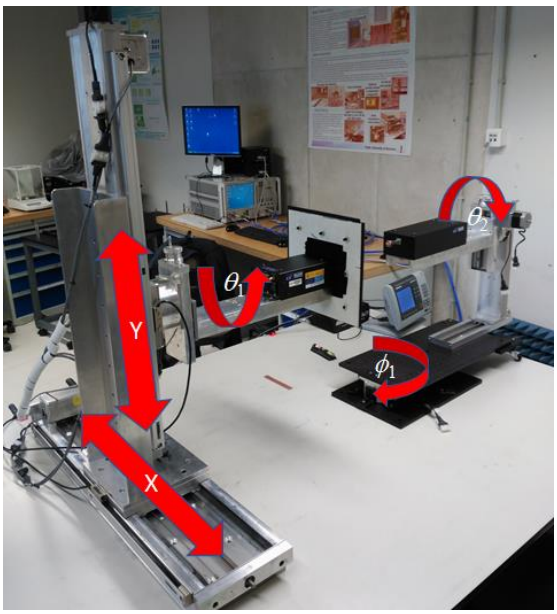


Fig. 97: Measuring set-up

For the planar Near-Field antenna measurement, an 8x8cm plane at a distance of 4 cm was chosen in order to guarantee at least -30 dB difference between the central point of the plane and its edges. The Near-Field to Far-Field transformation (NF2FF) [83] was performed offline. For this purpose, magnitude and phase of the electric field were previously measured and stored. The measuring probe effect [84] was also corrected through an offline processing. The measured points preserved a sampling span of $\lambda/2$ between

each other in order to prevent from creating aliasing after applying the transformation. As to reduce the effect of parasitic reflections in the measurement process, a **dynamic time-domain gating** has been included in the LabVIEW script, in order to modify TD gating in the Vector Analyser, fixing its width and adjusting its position for every measuring point contained in the plane, so that any feasible reflection would not affect the measuring process. This implemented feature resulted of great importance in the measuring process, since the swept plane was considerably big in terms of wavelengths (64λ x 64λ for the central frequency of interest) and therefore it allowed to exclude undesired reflections.

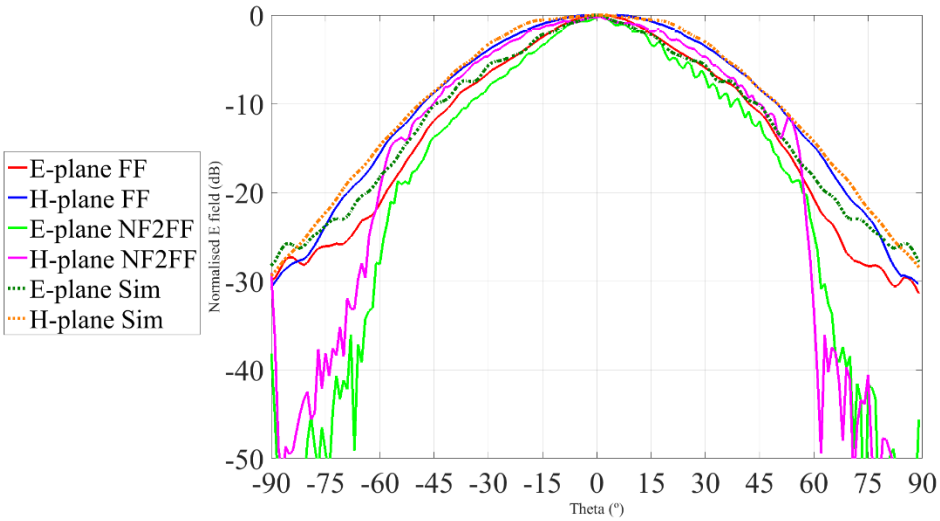


Fig. 98. Comparison of simulation and measurement results of the choke horn.

Fig. 98 shows the simulated and measured (in both far- and near-field techniques) radiation pattern of the antenna at 240 GHz for both E- and H-Plane. Doted lines correspond to the simulation results, while solid lines represent the measured ones. The measured results show reasonable agreement to the simulation results. Some ripples at the NF2FF radiation pattern can be observed. These are thought to be caused by two main reasons. First of all, the parasitic reflection from elements included in the time-domain gating, such as the screws that hold the antenna, whose size was comparable to the size of the antenna and whose position was not far enough to be excluded by the time-domain gating. Secondly, the measuring process itself, which limits the measuring area to a defined plane, creates a spatial window effect aliasing after applying the transformation and thus results not contained in the approximated interval $\theta \in [-55^\circ, 55^\circ]$ are not reliable.

All in all, this appendix aims to demonstrate a successful method for both Near and Far-Field measurements. In addition, 3D printing is validated as a suitable manufacturing method for horn antennas at sub-THz frequencies.